Charles University in Prague

Faculty of Science

Ph.D. study program: Biochemistry

Mgr. Jana Škerlová

Understanding the interaction of antibodies and transcription factors with their ligands through structural biology

Využití strukturní biologie ke studiu interakce protilátek a transkripčních faktorů s jejich ligandy

Dissertation thesis

Supervisor: RNDr. Pavlína Maloy Řezáčová, Ph.D.

Prague, 2015

This dissertation describes my original work except where acknowledgement is made in the text. It is not substantially the same as any work that has been, or is being submitted to any other university for any degree, diploma or any other qualification.

Prague, 29.4.2015

……..

Mgr. Jana Škerlová

I hereby declare that Mgr. Jana Škerlová contributed significantly to all scientific publications that are part of this dissertation. She performed most of the experiments by herself and also took part in their planning; she interpreted all results and wrote the publications. Her contribution to the individual publications is expressed in percentage below.

1. Crystallization of the effector-binding domain of repressor DeoR from *Bacillus subtilis*
Pisackova, J., Prochazkova, K., Fabry, M. & Rezacova, P. (2013), *Crystal Growth and Design.* 13, 844-848. **– 90%**

2. Structure of the effector-binding domain of deoxyribonucleoside regulator DeoR from *Bacillus subtilis*
Skerlova, J., Fabry, M., Hubalek, M., Otwinowski, Z. & Rezacova, P. (2014), *The FEBS Journal.* 281, 4280-4292. **– 80%**

3. Optimization of the crystallizability of a single-chain antibody fragment
Skerlova, J., Kral, V., Fabry, M., Sedlacek, J., Veverka, V. & Rezacova, P. (2014), *Acta Crystallographica Section F, Structural Biology and Crystallization Communications.* 70, 1701-1706. **– 90%**

4. Molecular mechanism for the action of the anti-CD44 monoclonal antibody MEM-85
Skerlova, J., Kral, V., Kachala, M., Fabry, M., Bumba, L., Svergun, D. I., Tosner, Z., Veverka V. & Rezacova, P. (2015), under consideration in *Journal of Structural Biology.* **– 75%**

Prague, 29.4.2015

……..……..

RNDr. Pavlína Maloy Řezáčová, Ph.D.

This work was elaborated in the Laboratory of Structural Biology at the Institute of Molecular Genetics and the Institute of Organic Chemistry and Biochemistry, AS CR, v.v.i.

I acknowledge the funding sources that made my work possible. I was funded by the Grant Agency of the Charles University in Prague, project GA UK No. 567012. This work was also supported in part by projects RVO 61388963 and 68378050 awarded by the Academy of Sciences of the Czech Republic, by the Ministry of Education of the Czech Republic, projects LK11205 (program "NAVRAT"), LO1304 (program "NPU I"), and ME08016, and also by project GA203/09/0820 awarded by The Grant Agency of the Czech Republic. I also thank the team of the BESSY II electron storage ring, Helmholtz-Zentrum Berlin, for the opportunity to collect X-ray diffraction data.

First and foremost I want to thank my supervisor Pavlína Řezáčová for her patient guidance, encouragement, and for being an inspiration. I am also grateful to Václav Veverka for introducing me to NMR and for sharing his expertise.

My special thanks belong to my colleagues Milan Fábry and Vlastimil Král, for being my "lab mentors" in all aspects of scientific work and life, and also to Irena Sieglová who has always been ready to help and give me support. I wish to thank Petr Pachl and Jiří Brynda, who helped me with all crystallography hardware and software, Jitka Kredbová and Věra Mrkvičková for technical assistance with protein preparation, and Petr Těšina for his help with NMR assignments.

I would also like to express my appreciation to everyone from the Laboratory of Structural Biology for being such a great team. I am grateful to all colleagues and collaborators who contributed to the publications included in this thesis.

Last but not least, I thank my family for the unceasing encouragement, support and attention, most of all to my husband Jan for his care and patience.

Table of contents

1 Abbreviations 6

2 Abstract 8

3 Abstrakt 10

4 Preface 12

5 Introduction 14

5.1 Regulation of metabolism in *Bacillus subtilis* 14
5.1.1 Carbohydrate catabolism 14
5.1.2 Carbon catabolite repression of catabolic operons 15
5.1.3 Induction of catabolic operons 16
5.1.4 Metabolic repressors in *B. subtilis* 18
5.1.5 Transcriptional regulator DeoR form *B. subtilis* 19

5.2 CD44 antigen 22
5.2.1 CD44 function 22
5.2.2 CD44 structure 23
5.2.3 Hyaluronate-binding domain of CD44 24
5.2.4 CD44 regulation 27
5.2.5 CD44 in pathology 28
5.2.6 CD44 as a target in cancer therapy 29
5.2.7 Anti-CD44 antibodies in cancer therapy 30
5.2.8 Monoclonal antibody MEM-85 against CD44 32

6 Aims of the study 33

7 Publications 34

7.1 Crystallization of the effector-binding domain of repressor DeoR from *Bacillus subtilis* 35

7.2 Structure of the effector-binding domain of deoxyribonucleoside regulator DeoR from *Bacillus subtilis* 42

7.3 Optimization of the crystallizability of a single-chain antibody fragment 57

7.4 Molecular mechanism for the action of the anti-CD44 monoclonal antibody MEM-85 66

8 Discussion 99

8.1 Structural studies of deoxyribonucleoside regulator form *Bacillus subtilis* 99

8.2 Epitope mapping for the anti-CD44 monoclonal antibody MEM-85 102

9 Conclusions 106

10 References 108

1 Abbreviations

AraR	Arabinose repressor
CBS	Cystathionine beta synthase domain
CcpA	Catabolite control protein A
CcpN	Catabolite control protein N
CD	Cluster of differentiation
CD44	Hyaluronate receptor
CD44s	Standard isoform of CD44
CD44v	Variant isoform of CD44
C-DeoR	C-terminal effector-binding domain of deoxyribonucleoside
CggR	Central glycolytic genes regulator
c-myc	Transcription factor, proto-oncogene
CP	Cytoplasmic region
cre	Catabolite-responsive element
CrH	Catabolite repression Hpr-like protein
DBD	DNA-binding bomain
DBTBS	Database of transcriptional regulation in *B. subtilis*
deo	Deoxyribonucleoside catabolism operon from *E. coli*
DeoR	Deoxyribonucleoside regulator
Dra	Deoxyriboaldolase
Drm	Phosphodeoxyribomutase
EBD	Effector-binding domain
EGF	Epidermal growth factor
ERM	Ezrin, radixin, moesin
FadR	Fatty acid metabolism regulator
FrlR	Fructosamine repressor
FruR	Fructose repressor
GamR	Glucosamine repressor
glp	Glycerolphosphate operon
GmuR	Glucomannan operon repressor
GntR	Gluconate operon repressor
HABD	Hyaluronate-binding domain
HER2	Human epidermal growth factor receptor 2
HPr	Phosphocarrier protein
HSQC	Heteronuclear single quantum coherence
HutC	Histidine utilization repressor
Ig	Immunoglobulin
IolR	Myo-inositol operon repressor

LacI	Lactose operon repressor
MALDI-TOF	Matrix-assisted laser desorption/ionization, time of flight
MEM-57	Murine monoclonal antibody against human CD3
MEM-85	Murine monoclonal antibody against human CD44
Mfd	Mutation frequency decline (transcription repair coupling factor)
NagC	N-acetylglucosamine repressor
NagR	N-acetylglucosamine repressor
NMR	Nuclear magnetic resonance
NupC	Nucleoside uptake protein C
O	Ordered conformation
PD	Partially disordered conformation
PDB	Protein Data Bank (http://www.rcsb.org)
Pdp	Pyrimidine nucleoside phosphorylase
pelB	Pectate lyase B leader sequence
PRD	Phosphotransferase regulator domain
PTS	Phosphoenolpyruvate: sugar phosphotransferase system
RAT	Ribonucleic antiterminator sequence
RbsR	Ribose operon repressor
SAXS	Small-angle X-ray scattering
scFv	Single-chain variable antibody fragment
siRNA	Small interfering RNA
SorC	Sorbitol operon regulator
SPR	Surface plasmon resonance
TCR	T-cell receptor
TM	Transmembrane region
T_m	Melting temperature
TreR	Trehalose repressor
V_H	Variable domain of the antibody heavy chain
V_L	Variable domain of the antibody light chain
XylR	Xylose operon repressor
YbgA	Alternative name for GamR
YdhQ	Alternative name for GmuR
YvoA	Alternative name for NagR
σ^A	RNA polymerase σ-43 factor
σ^L	RNA polymerase σ-54 factor

2 Abstract

Understanding protein function highly benefits from the knowledge of its three-dimensional structure, especially in the case of protein-ligand complexes. Structural biology methods such as X-ray crystallography, SAXS and NMR are therefore widely used for structural studies of protein-ligand interaction. In this work, these methods were used to understand two biological processes involving protein interactions: X-ray structural analysis was used to study binding of effector molecule to a prokaryotic transcription factor. NMR and SAXS techniques were used to study interaction of a monoclonal antibody with its protein antigen.

Transcriptional regulator DeoR negatively regulates the expression of catabolic genes for the utilization of deoxyribonucleosides and deoxyribose in *Bacillus subtilis*. DeoR comprises an N-terminal DNA-binding domain and a C-terminal effector-binding domain (C-DeoR), and its function is regulated by binding of a small-molecular effector deoxyribose-5-phosphate. We determined crystal structures of C-DeoR both in the free form and in complex with deoxyribose-5-phosphate. Structural analysis revealed unique covalent binding of effector molecule through a reversible Schiff-base double bond with an effector-binding-site lysine residue. The physiological nature of this binding mode was confirmed by mutational analysis and mass spectrometry of the Schiff-base adducts formed in solution. Comparison of the free and effector-bound structures of C-DeoR explained on a molecular level the mechanism of DeoR function as a molecular switch.

CD44, the cell receptor for hyaluronate, is involved in cell adhesion, migration, and tumor metastasis. CD44 binds hyaluronate through the hyaluronate-binding domain (HABD), which triggers an extensive conformational rearrangement in HABD that induces CD44 shedding. We constructed a single-chain variable fragment (scFv) of antibody MEM-85. MEM-85 is of therapeutic interest, recognizes a poorly characterized epitope in HABD, blocks hyaluronate binding, and induces CD44 shedding. Antibody scFv fragments exhibit poor homogeneity caused by scFv oligomerization. We developed a novel optimization approach, which we used for the preparation of a homogeneous scFv sample for NMR-based mapping of the epitope of MEM-85 in HABD. This mapping together with mutational analysis identified epitope residues in the C-terminal tail of the HABD. Additionally, we built a rigid-body model of the HABD – scFv MEM-85 complex based on the SAXS data. These biophysical methods provided a detailed insight into the

mechanism of MEM-85 action: MEM-85 binds to an epitope located outside the hyaluronate-binding site and induces a conformational change in the HABD tail, similar to that induced by hyaluronate. The mechanism of MEM-85 cross-blocking of hyaluronate binding is not a direct physical competition, but rather an allosteric, relay-like effect.

3 Abstrakt

K pochopení funkce proteinu významně přispívá znalost jeho trojrozměrné struktury, obzvláště v případě komplexů s ligandy. Metody strukturní biologie, jako je rentgenová krystalografie, SAXS nebo NMR, jsou proto ve strukturní analyse interakcí proteinů s ligandy široce využívány. V této práci byly tyto metody využity k objasnění molekulární podstaty dvou biologických dějů využívajících proteinové interakce: rentgenostrukturní analysa byla použita ke studiu vazby efektorové molekuly k prokaryotnímu transkripčnímu faktoru, metody NMR a SAXS byly využity ke studiu interakce monoklonální protilátky s proteinovým antigenem.

Transkripční regulátor DeoR negativně reguluje expresi katabolických genů pro utilizaci deoxyribonukleosidů a deoxyribosy v bakterii *Bacillus subtilis*. DeoR se skládá z N-koncové DNA-vazebné domény a z C-koncové efektor-vazebné domény (C-DeoR). Jeho funkce je regulována vazbou nízkomolekulárního efektoru deoxyribosa-5-fosfátu. Vyřešili jsme krystalové struktury C-DeoR ve volné formě a v komplexu s deoxyribosa-5-fosfátem. Strukturní analysa odhalila unikátní vazbu mezi molekulou efektoru a lysylovým zbytkem efektor-vazebného místa prostřednictvím reversibilní dvojné vazby typu Schiffovy base. Fysiologická relevance této vazby byla potvrzena mutačními experimenty a také analysou tvorby kovalentních aduktů v roztoku pomocí hmotnostní spektrometrie. Porovnání struktur volné C-DeoR a komplexu C-DeoR s efektorem vysvětlilo na molekulární úrovni funkci DeoR jako molekulárního spínače.

CD44, buněčný receptor pro hyaluronát, se účastní buněčné adhese, migrace a metastazování nádorů. CD44 váže hyaluronát prostřednictvím hyaluronát-vazebné domény (HABD), což indukuje v HABD rozsáhlou konformační změnu, vedoucí k proteolytickému uvolnění CD44 z povrchu buněk. Vytvořili jsme jednořetězcový variabilní fragment (scFv) protilátky MEM-85. MEM-85 má terapeutický potenciál, rozpoznává nedostatečně popsaný epitop v HABD, blokuje vazbu hyaluronátu a indukuje odštěpení CD44. Fragmenty scFv jsou kvůli své oligomeraci obvykle nehomogenní. Vyvinuli jsme nový optimalizační přístup, pomocí něhož jsme připravili homogenní vzorek scFv vhodný pro NMR mapování antigen-vazebného epitopu protilátky MEM-85 v CD44 HABD. Toto mapování společně s mutační analysou vedlo k identifikaci protilátkového epitopu v C-koncové části HABD. Na základě SAXS analysy jsme také vytvořili model komplexu HABD s scFv MEM-85. Tyto biofysikální metody přinesly

detailní vhled do mechanismu funkce MEM-85: MEM-85 váže epitop, který se nachází mimo hyaluronát-vazebné místo, a indukuje v C-konci HABD strukturní změny, jež jsou podobné změnám vyvolaným vazbou hyaluronátu. Blokace vazby hyaluronátu protilátkou MEM-85 proto nespočívá ve fysické kompetici o vazebné místo, ale jde spíše o allosterický přenosový efekt.

4 Preface

This work includes a combination of two research projects: structural studies of prokaryotic transcriptional regulators and structural studies of antibody-antigen interaction. The common basis of both projects is the understanding of protein-protein and proteinligand interactions and their effects on protein structure and function through structural biology. The first project is based on protein X-ray crystallography technique, whereas the second one utilizes NMR and SAXS techniques, illustrating thus the powerful synergy of these methods in structural biology.

X-ray crystallography is the principal method for determination of structures of biological macromolecules. It has made an immense impact in the field of biochemical and biological research; there have been 25 Nobel laureates connected to X-ray crystallography. Determination of protein three-dimensional structure is driven by the objective to gain the knowledge on the protein's biological activity, which is very often associated with the characterization of ligand binding. In an ideal case, X-ray crystallography enables structure determination for protein-protein and protein-ligand complexes at a resolution high enough to directly observe atomic details of covalent and non-covalent interactions in three dimensions. This allows for further analysis of the protein's mode of action on the molecular level, as well as for the design of small-molecular inhibitors of the protein's function. Moreover, the knowledge of high-resolution three-dimensional structures of the protein in the free and ligand-bound states constitutes the basis for understanding the ligand-induced changes in the protein conformation and thus unravels the effects of the ligand binding on the function of the protein.

The use of X-ray crystallography is irreplaceable for the detailed studies of the function of prokaryotic transcriptional regulators on the molecular level. These transcription factors function as molecular switches and their action usually includes extensive ligand-induced conformational changes associated with the modulation of oligomeric state. The first part of this thesis comprises X-ray structural study of deoxyribonucleoside regulator DeoR from *Bacillus subtilis* with the aim to undestand the regulation of its function by the small-molecular effector, deoxyribose-5-phosphate.

NMR methods play a prominent role in biochemistry and molecular biophysics for probing molecular structure and interactions. X-ray crystallography is still a simpler and more straightforward method of structure determination, especially in the case of larger molecules and complexes. However, solution NMR is the method of choice in structure determination of molecules that are resistive to forming well-ordered crystals. Moreover, the classical NMR applications, where the complete structure determination is not the goal, demonstrate the wide-range impact of NMR in biological and biophysical research. In particular, solution NMR has become the paramount method for studying molecular dynamics and for characterization of protein-ligand and protein-protein interactions. The method of choice for this application is the differential chemical shift perturbation method, which is based on the fact that the NMR-active nuclei that are located at the interaction interface undergo changes in their chemical shift, which are not observed for distant nuclei. Therefore, the location of the binding site on the protein can be mapped.

Recently, this widely applicable approach has been increasingly used to characterize antigen – antibody complexes, usually for the definition of the antigen-binding epitopes of therapeutic antibody fragments. The second part of this thesis is focused on the characterization of antibody binding to a cancer marker CD44. We have prepared a single-chain variable fragment of antibody MEM-85, which recognizes human CD44 antigen and which is of therapeutic potential and employed the NMR-based differential chemical shift perturbation method to map the antibody epitope.

5 Introduction

5.1 Regulation of metabolism in *Bacillus subtilis*

In order to be evolutionarily successful, bacteria need to be competitive both under limited and excessive supply of carbon and energy resources. They have to be able to efficiently select the preferred, most energetic carbon source out of a mixture of nutrients available in the environment at a given moment. The underlying regulatory mechanisms have been extensively studied in *Escherichia coli* as well as in *Bacillus subtilis*, the model Gram-positive bacterium [1, 2].

Bacillus subtilis is a soil bacterium, that can use at least 18 different mono- or disaccharides as sole sources of carbon and energy, as it produces extracellular hydrolases to digest polysaccharides of plant biomass [3]. The most preferred carbon and energy source is glucose and the expression of the genes involved in the catabolism of alternative nutrients is strictly controlled by two key mechanisms: carbon catabolite repression and induction. The carbon catabolite repression mechanism ensures that the genes encoding enzymes for the utilization of the non-preferred carbon sources are not expressed in the presence of the preferred nutrient. Additionally, the more specific induction mechanism ensures that genes for alternative catabolic pathways are not expressed, unless the respective alternative substrate is present in the environment. This regulation network includes a wide range of specific repressor proteins and functions at the level of transcription of metabolic operons [1, 4].

5.1.1 Carbohydrate catabolism

B. subtilis excretes various enzymes including glucanases, proteases and nucleases to decompose complex nutrients present in the soil. Amylases and glucanases are of major importance, as they degrade glucose polymers and produce maltodextrins, maltose, and glucose, the most preferred nutrient. The resulting mono-, di-, or oligosaccharides are imported into the cell by facilitated diffusion, secondary active transporters, ATP-binding cassette transporters, or the phosphoenolpyruvate: sugar phosphotransferase system (PTS), which phosphorylates the transported substrates. The PTS system not only transports nutrients into the cell, but also plays role in signal transduction. The system consists of two universal proteins: enzyme I and phosphocarrier protein (HPr), and of numerous

substrate-specific enzymes II. Enzymes II are protein complexes that perform the actual transport of the nutrients which are simultaneously phosphorylated by the cooperative action of enzyme I, HPr, and components of enzyme II complex [1, 3].

Once in the cell, the di- or oligosaccharides or their phosphorylated forms are cleaved by the respective glycosidases or phosphoglycosidases, respectively. The non-phosphorylated products are phosphorylated by kinases and enter the pentose phosphate pathway and glycolysis, yielding pyruvate which is converted by pyruvate dehydrogenase complex to acetyl-coenzyme A to be further metabolized in the tricarboxylic acid cycle. Apart from sugars, *B. subtilis* can also import and utilize various carbohydrate derivatives, such as aminosugars, hexitols, hexuronic acids, deoxyribose, and glycerol [3].

5.1.2 Carbon catabolite repression of catabolic operons

Carbon catabolite repression mechanisms ensure that catabolic genes and operons for alternative nutrients are not transcribed as long as preferred carbon and energy sources are present in the environment. This regulation can be achieved by three mechanisms: (1) control of the catabolic genes transcription by global sensor proteins registering the presence of preferred nutrients, (2) regulation of the intracellular availability of the catabolic genes inducers (inducer exclusion), or (3) induction prevention by operon-specific regulators controlled by preferred nutrients [2, 5, 6]. *B. subtilis* combines these mechanisms while using the PTS system and HPr kinase as the intracellular sensors of nutrient availability that trigger further carbon catabolite repression pathways [1, 7].

HPr can be phosphorylated by an ATP-dependent HPr kinase activated by specific metabolites, which leads to decreased PTS activity. HPr kinase functions both as kinase and phosphatase. The kinase activity is stimulated by glycolytic intermediates and inhibited by inorganic phosphate, which also stimulates the phosphatase activity of HPr kinase. Phosphorylated HPr protein can than act as a cofactor of the PTS system, or phosphorylate other regulatory proteins. Phosphorylated HPr binds to the C-terminal effector-binding domain of catabolite control protein A (CcpA), a transcriptional regulator that binds through its N-terminal DNA-binding domain to operator palindromic sequences *cre* (catabolite-responsive element) in various operons and genes. The interaction of CcpA with the phosphorylated HPr downregulates the expression of catabolic genes by binding the *cre* elements or by direct contact of the HPr-bound CcpA with RNA polymerase. CcpA

can also function as a transcriptional activator of glycolytic and overflow metabolism genes in the presence of preferred nutrients by interacting with the *cre* sites located upstream of the promoters of their operons, which enables very fast growth [1, 7].

The presence of preferred nutrients in the cell can prevent transport or formation of effector molecules inducing the expression of catabolic operons. An example of this inducer exclusion mechanism is *B. subtilis glp* operon, where the PTS is involved in formation of the inducer glycerol-3-phosphate. Monophosphorylated HPr can phosphorylate glycerol kinase and enhance its kinase activity [8]. The concentration of this monophosphorylated form of HPr is lower in the presence of preferred carbon sources, as it is depleted as a cofactor of the PTS by the nutrient-specific enzyme II or by phosphorylation of other HPr residues by HPr kinase. Therefore, glycerol kinase is less active and lower amount of the inducer glycerol-3-phosphate is formed under carbon catabolite repression conditions [1, 9].

Several catabolic operons for the non-preferred nutrients are positively regulated by activators or antiterminators in the presence of the inducer. Transcriptional factors of this type are inactivated in the absence of the inducer by the PTS-dependent phosphorylation at their phosphotransferase regulator domains (PRDs). Some of these proteins, which are subject to carbon catabolite repression, are only active (binding DNA) when phosphorylated at other sites in their PRDs by the monophosphorylated HPr protein. This additional HPr-dependent phosphorylation of the PRDs prevents induction of the catabolic operons for the non-preferred nutrients [1].

5.1.3 Induction of catabolic operons

The operons coding for the enzymes required for the catabolism of specific nutrients are not expressed, unless the respective carbon source is present in the environment. This process is controlled at the level of transcription by three different mechanisms: transcriptional repressors, activators, and antiterminators [3].

Transcriptional repressors in *B. subtilis* negatively control expression of operons for the catabolism of numerous nutrients including glucose, glucosamine, N-acetyl-glucosamine, trehalose, glucomannan, fructose, fructosamine, inositol, gluconate, arabinose, ribose, deoxyribose, xylose, and galactose. In the absence of the nutrient, the repressor binds through the N-terminal DNA-binding domain to the DNA operator site, usually upstream of the operon. In the presence of the effector (the nutrient or its catabolic intermediate), the

repressor binds the effector through the C-terminal effector-binding domain and the resulting conformational change results in lower affinity towards the DNA operator or even promotes dissociation of the repressor from the operator (see Figure 1) [1].

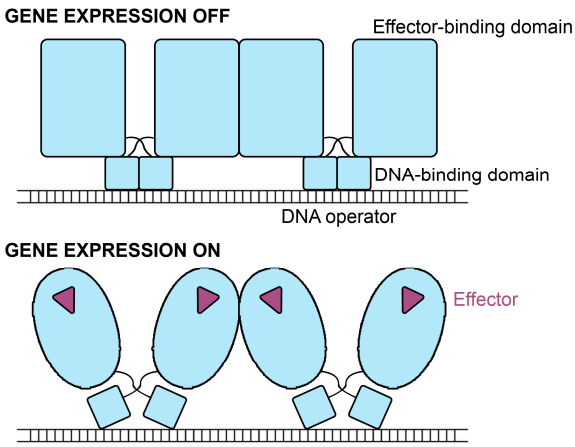

Figure 1: Regulation of catabolic genes expression by a transcriptional repressor
The molecular-switch function of a transcriptional repressor is schematically illustrated.

Transcriptional activators regulate the expression of catabolic genes for nutrients such as oligo-β-glucoside, fructose, mannitol, mannose, and glucitol and can be divided into two classes: (1) activators functional only in the complex with their specific inducer and (2) activators modulated by phosphorylation dependent on the presence of the substrate. Vast majority of *B. subtilis* activators are phosphorylation-regulated and can be further subclassified as activators of the σ^A- or σ^L-dependent promoters. The activator proteins typically contain an N-terminal DNA-binding domain and several other domains with additional functions and conserved phosphorylation sites, which are phosphorylated by PTS components (HPr or enzyme II) in the absence of the respective nutrient, which results in the inactivation of the activator protein [1, 10].

Transcriptional antiterminators regulate the expression of catabolic operons coding for utilization of nutrients including glucose, sucrose, β-glucosides, and glycerol. Most of the transcriptional antiterminators consist of an N-terminal RNA-binding domain and two PRD domains. The antiterminator-regulated operons are transcribed constitutively, but the transcription stops at transcriptional terminator sequences located upstream of the open reading frames. The 5'-parts of the terminators can be incorporated into stem-loop structures formed by ribonucleic antiterminator inverted repeat sequences (RATs). The antiterminator regulatory proteins bind the RAT sequences through their RNA-binding

domains, and their binding promotes transcription. In the absence of the specific nutrient, the PRDs are phosphorylated by PTS components (HPr or enzyme II), resulting in inactivation of the respective antiterminator protein [1, 10].

5.1.4 Metabolic repressors in *B. subtilis*

Majority of the transcriptional repressors regulating catabolic genes in *Bacillus subtilis* that have been characterized so far are members of following families of prokaryotic transcriptional factors: DeoR, GntR, SorC or LacI (see Table 1). The classification of the families is based on the sequence similarity of the N-terminal helix-turn-helix DNA-binding domains of the repressors. These conserved DNA-binding domains are combined with C-terminal effector-binding domains belonging to various structural families. The C-terminal domains are responsible for effector molecule recognition and for repressor oligomerization (see Figure 1, Table 1). This chimeric domain organization allows for great structural and functional variety of metabolic repressors. Several *B. subtillis* repressors have been studied on the structural level by X-ray crystallography (Table 1), usually as individual domains with the exception of the recently determined crystal structure of the full-length repressor NagR, also in the complex with its DNA operator [11, 12].

Table 1: Repressors in carbohydrate utilization in *Bacillus subtilis*[a]

Sugar	Operon	Repressor	DBD family (PDB code)	EBD family (PDB code)
Arabinose	*araABDLMNOPQ-abfA*	AraR	GntR (4EGY [13])	LacI (3TB6 [14])
Deoxyribose	*dra-nupC-pdp*	DeoR	SorC	SorC
Fructosamine	*yurPONML*	FrlR	GntR	HutC (2IKK)
Fructose	*fruRBA*	FruR	DeoR	DeoR
Galactose	*galKT*	AraR	GntR (4EGY [13])	LacI (3TB6 [14])
Glucomannan	*ydhMNOPQRST*	GmuR (YdhQ)	GntR	?[b]
Gluconate	*gntRKPZ*	GntR	GntR	FadR
Glucosamine	*gamAP*	GamR (YbgA)	GntR	?[b]
Glucose	*gapB-speD*	CcpN	DeoR	2 × CBS (3FV6)
Glucose	*cggR-gapA-pgk-tpiA-pgm-eno*	CggR	SorC	SorC (2OGK [15])
Inositol	*iolABCDEFGHIJ*	IolR	DeoR	DeoR
N-acetyl-glucosamine	*nagP-nagAB-yvoA*	NagR (YvoA)	GntR (2WV0 [11], 4WWC [12])	HutC (2WV0 [11], 4WWC [12])
Ribose	*rbsRKDACB*	RbsR	LacI	LacI
Trehalose	*trePAR*	TreR	GntR	HutC (2OGG [16])
Xylose	*xylAB*	XylR	?[b]	NagC/XylR

[a]compiled from [1], Pfam database [17], database of transcriptional regulation in *Bacillus subtilis* (DBTBS [18]), Protein data bank (PDB, http://www.rcsb.org), and UniProt (www.uniprot.org); [b]domains were not unambiguously classified; DBD, DNA-binding domain; EBD, effector-binding domain.

5.1.5 Transcriptional regulator DeoR form *B. subtilis*

Bacillus subtilis can utilize deoxyribonucleosides and deoxyribose as a source of carbon and energy. The deoxyribonucleosides are imported into the cell by nucleoside uptake protein C (NupC) and phosphorolytically cleaved by pyrimidine nucleoside phosphorylase (Pdp), yielding a base and deoxyribose-1-phosphate, which is converted to deoxyribose-5-phosphate and further processed by deoxyriboaldolase (Dra) to acetaldehyde and glyceraldehyde-3-phosphate. The genes encoding these three key enzymes of this catabolic pathway are grouped into the *dra-nupC-pdp* operon, which is under negative transcriptional control of the deoxyribonucleoside regulator, DeoR [19]. Another enzyme involved in this catabolic pathway is phosphodeoxyribomutase (Drm) which converts deoxyribose-1-phosphate to deoxyribose-5-phosphate. This enzyme is encoded by the *drm* gene located far from the *dra-nupC-pdp* operon in *B. subtilis* and its expression is therefore probably modulated by some other regulatory protein [19].

The *deoR* gene is located immediately upstream of the *dra-nupC-pdp* operon [19] and codes for the 313 amino acids long DeoR repressor protein that recognizes a palindromic operator sequence located between the positions -60 and -43 relative to the transcription start site for the *dra-nupC-pdp* operon. Also, a direct repeat sequence identical to the 3′-half of the palindrome, that might be another possible DeoR binding site, is located downstream to the palindrome (see Figure 2, Table 2) [20].

The *dra-nupC-pdp* operon is subject to another negative regulation mechanism, carbon catabolite repression by glucose [20, 21]. The operon carries one *cre* element, located downstream of the *dra* transcription start site (Figure 2). The catabolite repression by HPr can be in this case substituted by the homologous CrH protein [21], which is also phosphorylated by HPr kinase and then induces CcpA binding to *cre*, similarly to phospho-HPr [22, 23]. Mfd protein is also involved [21], which is a strand-specific DNA repair protein that is able to displace RNA polymerase form downstream-located *cre* sites [24].

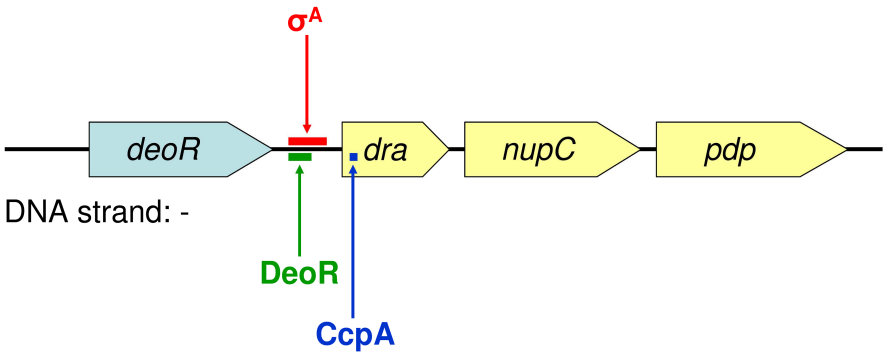

Figure 2: Schematic overview of the *deoR-dra-nupC-pdp* operon
Genome positions of the individual genes in the minus DNA strand are schematically illustrated: *deoR* is the deoxyribonucleoside regulator gene, *dra* is the deoxyriboaldolase gene, *nupC* is the nucleoside uptake protein C gene, and *pdp* is the pyrimidine nucleoside phosphorylase gene. Promoter and operator sites for RNA polymerase σ-43 factor (σ^A), deoxyribonucleoside regulator (DeoR), and catabolite control protein A (CcpA) are also indicated in colors. Compiled from [18, 19].

Table 2: Promoter and operator sites of the *dra-nupC-pdp* operon in *Bacillus subtilis*

Factor	Location	Binding sequence (cis-element)[a]	Ref.
CcpA	+60 – +82	GCTTTGAAACCGCATACACAAAA	[19]
DeoR	-60 – -22	ATTGAACAAAATTTCAATTACCAATTTACAT ATGTTCAA	[19, 20, 25]
σ^A	-60 – +10	ATTGAACAAAATTTCAATTACCAATTTACAT ATGTTCAAAAGTCGGTTATGCTAAAAAATAT CTTAACAA	[19]

[a]The minimal operator binding sites for catabolite control protein A (CcpA) and deoxyribonucleoside regulator (DeoR) are highlighted in red. Compiled from [18].

Both deoxyribose-1-phosphate and deoxyribose-5-phosphate are suggested to function as inducers of the catabolic operon, but only deoxyribose-5-phosphate appears to be the true effector [20]. Despite the participation of Pdp and Drm in the catabolism of pyrimidine ribonucleosides, no induction of expression of the *dra*, *pdp*, or *drm* genes has been observed in *B. subtilis* in the presence of ribonucleosides [19]. The carbon catabolite repression of the *dra-nupC-pdp* operon only occurs when the operon is not repressed by DeoR [21]. Also, neither CcpA, nor DeoR binds strong enough to totally prevent expression of the *dra-nupC-pdp*. This might be a protective mechanism against the toxic effects of deoxyribose-5-phosphate [19], or it may also be a result of the action of phosphodeoxyribomutase, which constitutively produces very low amounts of deoxyribose-5-phosphate from deoxyribose-1-phosphate [26].

The DeoR regulator from *Bacillus subtilis* is not related to the DeoR from *Escherichia coli* [18, 25], which belongs to the DeoR family and regulates the *deo* operon and has been studied in great detail [27]. Although both DeoR regulators from *B. subtilis* and *E. coli* contain a similar helix-turn-helix motif typical for DNA-binding proteins [28, 29] there is very little sequence similarity between them, and there is no similarity between their DNA operator sites [20, 25, 30]. The N-terminal DNA-binding domain of the *B. subtilis* DeoR is homologous to the SorC family of regulator proteins from various bacteria species that play role in transcriptional regulation of sugar alcohol catabolism genes [25]. The C-terminal effector-binding domain of *B. subtilis* DeoR is homologous to the SorC-type regulators of glucose metabolism genes that probably recognize glyceraldehyde-3-phosphate as the effector molecule [25]. The domain organization of DeoR is shown in Figure 3.

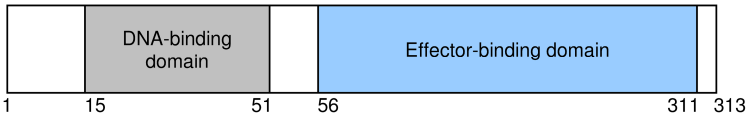

Figure 3: Domain organization of DeoR
The modular domain organization of deoxyribonucleoside regulator (DeoR) is schematically illustrated with residue numbers indicating domain boundaries according to [17].

The only one SorC-type transcriptional regulator characterized so far in *B. subtilis* is the central glycolytic genes regulator, CggR [18]. The sequence identity of DeoR and CggR is 20% (according to the UniProt Align tool at www.uniprot.org/align). Crystal structure of the CggR effector-binding domain, which is also classified as the SorC-type effector-binding domain, has been determined and revealed a double-Rossmann fold core with three accessory peripheral subdomains involved in repressor oligomerization and effector binding. CggR binds four different ligands: fructose-1,6-bisphosphate, dihydroxyaceton phosphate, glucose-6-phosphate, and fructose-6-phosphate. Each of these ligands induces individual specific conformational changes that influence the dimer interface in the effector-binding domain and affect the distribution of the repressor oligomers [15].

5.2 CD44 antigen

The CD44 antigen, a type I transmembrane glycoprotein also known as lymphocyte homing/adhesion receptor, epican, or Hermes antigen, was first described in 1983 [31-33]. CD44 is the principal cell receptor for hyaluronate [34], which is a major component of extracellular matrix. CD44 can also mediate binding to other components of extracellular matrix, including fibronectin, collagen, laminin, and fibrin and to several cell-surface ligands, such as E-, P-, and L-selectin [35-39]. Intracellular portion of CD44 is involved in signaling pathways [39, 40]. It interacts through ankyrin adaptor protein with spectrin and is involved in hyaluronate-dependent cell adhesion and motility [41]. Other binding partners of the intracellular CD44 domain are ezrin, radixin and moesin (ERM proteins) involved in the regulation of cell migration, shape, and protein resorting in the plasma membrane [42]. The ERM proteins mediate the interaction of CD44 intracellular domain with filamentous actin [43] which results in CD44 clustering [39, 40].

CD44 is expressed in most mammalian tissues, mainly in the gastrointestinal tract, skin, spleen, and leukocytes. Lower expression level can be observed in erythrocytes, neurons, and brain. CD44 is not expressed in kidney, hepatocytes, and mature thymocytes [32, 44]. The expression of CD44 on blood cell progenitors is strictly regulated during differentiation and it can be induced in many cell types only after cell activation [45, 46].

5.2.1 CD44 function

The CD44 receptor is involved not only in cell adhesion, but also in cell survival and proliferation, growth factor presentation, apoptosis, and cell motility and migration [47]. CD44 is a key player in lymphocyte trafficking and recirculation, including lymphocyte extravasation and homing to the peripheral lymphoid organs or the site of inflammation. These processes are initiated by a CD44-mediated rolling adhesion of lymphocytes to endothelial cells presenting hyaluronate (see Figure 4) [48]. CD44 also mediates and regulates the mobilization and distribution of blood cell progenitors during hematopoiesis in bone marrow [39, 49]. CD44 is also important for hyaluronate metabolism as it executes hyaluronate internalization which allows subsequent hyaluronate degradation by acid hydrolases within low-pH cellular compartments such as lysosomes [50]. This process is regulated by a palmitoylation-dependent association of CD44 with lipid rafts [51].

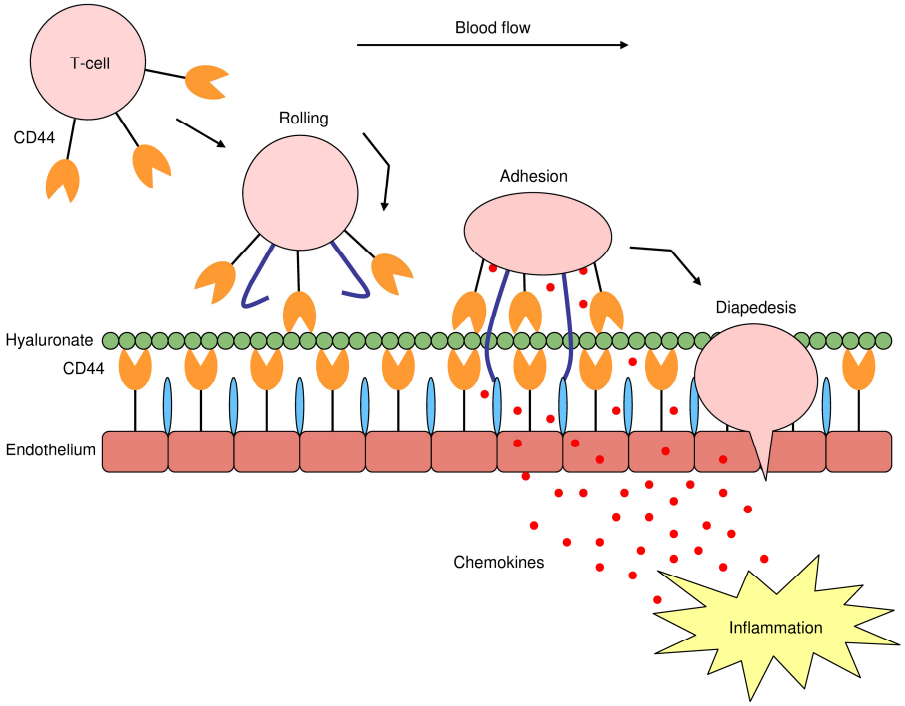

Figure 4: CD44 in lymphocyte homing
Schematic representation of CD44-mediated rolling of lymphocytes on endothelium is shown. T-cell capture and rolling are mediated by CD44 (orange) recognition of hyaluronate (green) presented on the endothelial cells. Firm adhesion is induced by the binding of integrins (dark blue) activated by inflammatory chemokines (red) to their counter-receptors (light blue) on the endothelium, which results in T-cell diapedesis, extravasation, and migration to the site of inflammation. Amended from http://www.glycoforum.gr.jp/.

5.2.2 CD44 structure

The 363 amino acids long CD44 glycoprotein (residues 21-383; see Figure 5) belongs to the cartilage Link protein superfamily [52, 53]. The extracellular portion of CD44 comprises the N-terminal 158 amino acids long extended Link domain coded by exons S1-S4 followed by the 112 amino acids long stem region coded by exons S5, S6, and S7 [54]. The stalk-like structure can be enlarged by the insertion of variable exon products V1-V10 between residues 222 and 223 due to alternative splicing [45, 55]. The extracellular portion of CD44 is followed by the 21 amino acids long hydrophobic transmembrane region coded by exon S8. Exons S9 and S10 code for the 72 amino acids long intracellular C-terminal domain [56, 57].

CD44 is subject to posttranslational modification. The N-terminal part is heavily N-glycosylated (Asn25, 57, 100, 110, and 120 [58]), the membrane-proximal serine- and threonine-rich extracellular region is O-glycosylated, an intracellular serine residue can be phosphorylated, and two conserved cysteine residues in the transmembrane domain and in the membrane-proximal cytoplasmic region can be palmitoylated [45, 51, 57]. The stem

region contains putative proteolytic cleavage site that allows for CD44 shedding [59]. After the ectodomain shedding, the intracellular domain can be released by an intramembrane presenilin-dependent γ-secretase cleavage [60] and the released cytoplasmic CD44 domain can then function as a transcription factor in the nucleus, promoting expression of numerous genes [61].

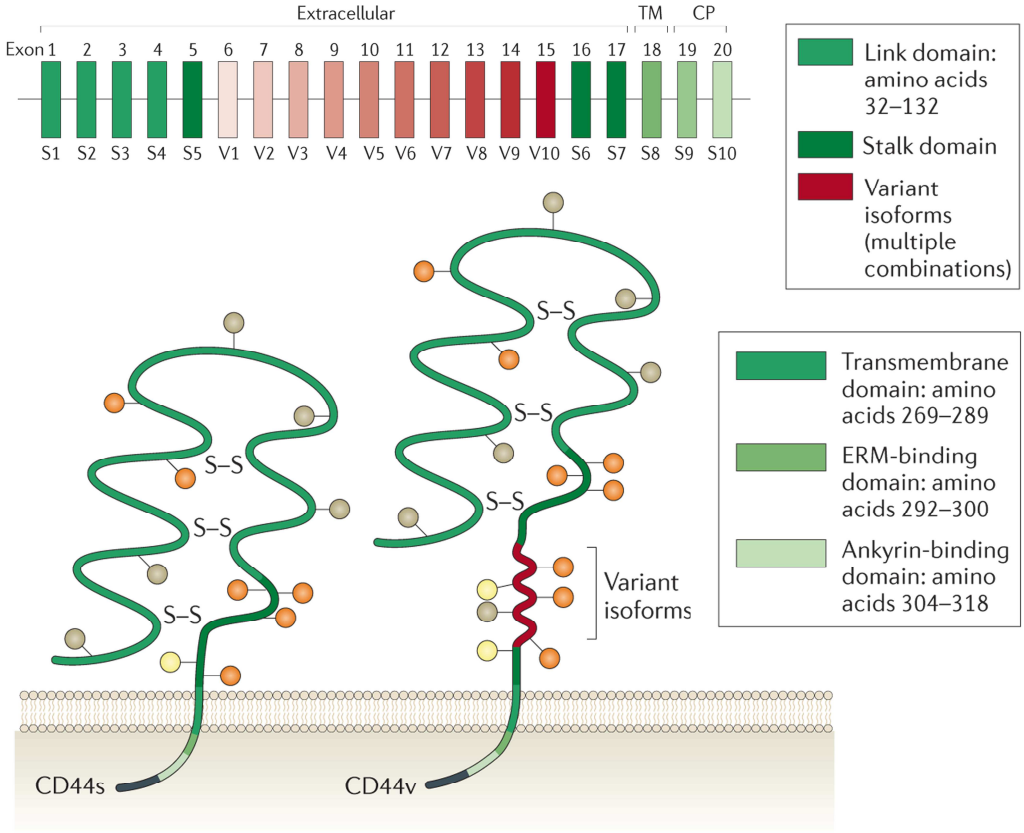

Figure 5: CD44 gene and protein structure
CD44 gene composition is shown comprising 10 constant exons (S1-S10) and 10 alternatively spliced variable exons (V1-V10), coding for the extracellular, transmembrane (TM), and cytoplasmic (CP) portions of CD44. The CD44 protein products, the standard (CD44s) and variant (CD44v) isoforms are schematically illustrated with the color coding indicating the extracellular, transmembrane, Link, and stalk domains, the variable exons, and also the interaction sites for ankyrin and for the ezrin, radixin, and moesin (ERM) proteins. N-glycosylation sites are represented by grey circles, O-glycosylation sites by orange circles, and glycosaminoglycan-binding sites by yellow circles. S-S indicates disulfide bonds. Adapted from [57].

5.2.3 Hyaluronate-binding domain of CD44

The N-terminal extended Link domain is responsible for hyaluronate binding and therefore, it is often referred to as the CD44 hyaluronate-binding domain (CD44 HABD). CD44 HABD binds hyaluronate molecules in a wide range of molecular weights. The minimum length of hyaluronate chain to be recognized by HABD is a hexamer and optimal

binding was achieved for hyaluronate octamer [62, 63]. Three-dimensional structures of mouse and human HABD have been determined by X-ray crystallography and NMR, respectively [62-64]. These structures revealed that HABD has a novel type of C-lectin fold, which can be designated as: β0 - β0' - **β1** - **α1** - **α2** - **β3** - **β4** - **β5** - **β6** - β7 - β8 - β9 - α3 (see Figure 6). The 100 amino acids long hyaluronate-binding Link module (residues 32-132, in bold) contains two highly conserved disulfide bridges and its sequence is generally conserved within the family of hyaluronate-binding proteins (80 – 90% sequence similarity) [33, 40, 45, 65]. Link module is the most evolutionarily conserved part of the whole CD44 antigen [66, 67]. In contrast to other Link superfamily members, the Link module in CD44 HABD is equipped with an extension lobe formed by β0 and β0' at the N-terminus and by β7, β8, β9, and α3 at the C-terminus of HABD [62]. This extension is crucial for structural integrity as it contains an additional disulfide bridge important for the correct folding of the Link module [68] and it also plays an important role in hyaluronate binding [65, 69]. The key interactions for the hyaluronate binding to human CD44 are hydrogen bonds with residues Arg41, Tyr42, Arg78 a Tyr79 from the Link module, but residues Arg29, Arg150, Arg154, Lys158 a Arg162 from the extension lobe also take part in hyaluronate binding, suggesting a more complex hyaluronate-binding mode than in the case of other hyaluronate-binding proteins of the Link family [62, 63, 65].

The solution structure of HABD in complex with hyaluronate determined by NMR [64] unraveled a major allosteric conformational change in HABD induced by the ligand binding (Figure 6): β9 strand and α3 helix become an unstructured random coil, and β8 and β0 strands are repositioned relative to each other, which results in an enhanced flexibility of the C-terminus of the HABD [64]. The ligand-free state of HABD is referred to as "ordered" (O) and the ligand-bound state as "partially disordered" (PD). The O-state structure of the ligand-bound murine CD44 HABD has been also captured by X-ray crystallography, probably because the rigid ordered conformation is more likely to form crystal contacts [63]. There is a two-state equilibrium between the O- and PD-conformational states of CD44 HABD and both conformations are capable of hyaluronate binding [70]. However, the PD-conformation exhibits higher affinity towards hyaluronate and it is also more resistant to cell detachment from a hyaluronate-coated surface in comparison to the O-conformation [70]. This conformational equilibrium has been proposed to be a mechanism essential for the proper CD44-mediated cell rolling, specifically for the formation of new contacts of the CD44 receptor with hyaluronate at the cell rolling front and for their disruption at the rear edge [70]. The ligand-induced shift in

the equilibrium in the favor of the PD-conformation also results in the elongation of the stalk-like membrane-proximal region of CD44. This makes the stem region more easily accessible to matrix metalloproteases and thus enhances the proteolytic susceptibility of the cleavage sites [64], which results in hyaluronate-induced HABD shedding and regulates thus cell motility and migration [59, 71, 72] (Figure 7).

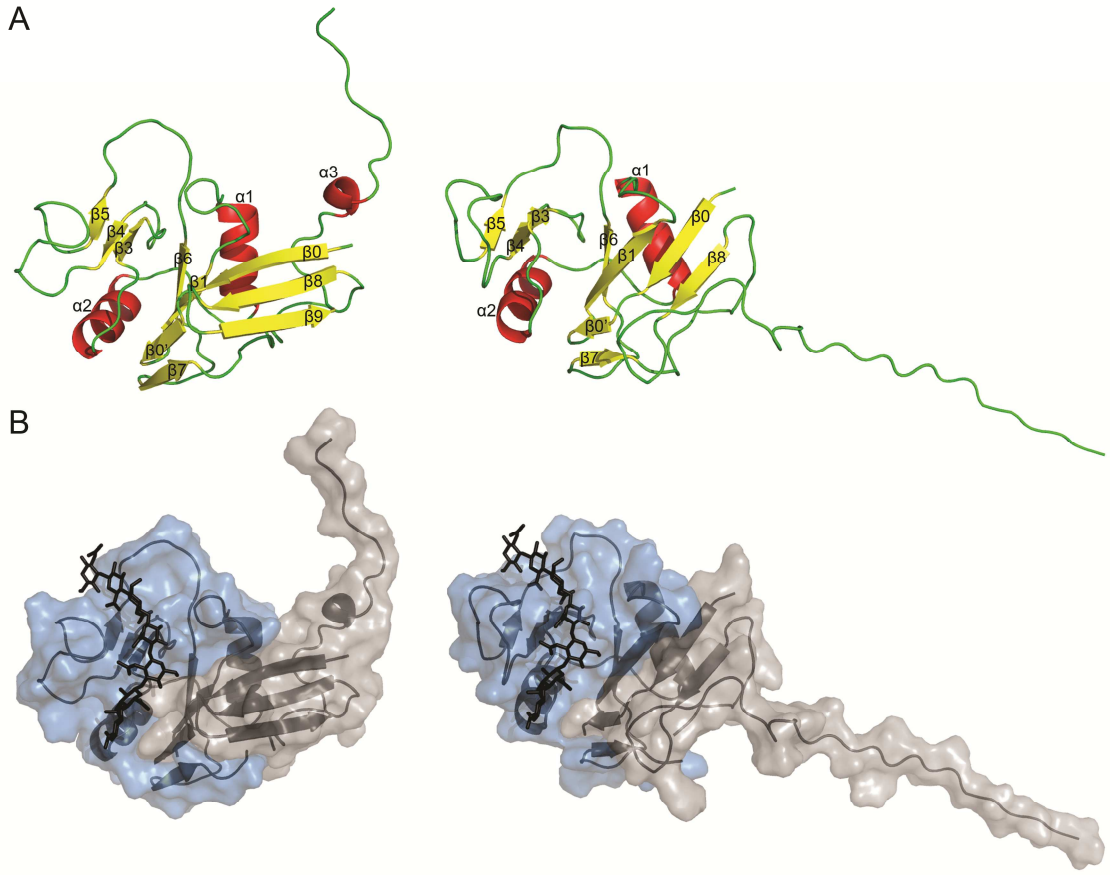

Figure 6: Structures of the CD44 hyaluronate-binding domain
A: CD44 hyaluronate-binding domain (HABD) topology is depicted in a cartoon diagram of the ligand-free CD44 HABD (left, PDB code 1POZ [62]) and hyaluronate-bound CD44 HABD (right, PDB code 2I83 [64]). Secondary structure elements are labeled; α-helices are in red, β-strands are in yellow, and random coil is in green. B: Hyaluronate-induced structural changes are depicted in a cartoon-surface diagram of the ligand-free CD44 HABD (left, PDB code 1POZ [62]) and hyaluronate-bound CD44 HABD (right, PDB code 2I83 [64]). The Link module is shown in blue and the extension lobe in gray. The hyaluronate octamer from the crystal structure of the hyaluronate-bound murine CD44 HABD (PDB code 2JCQ [63]) is superposed onto the structures to mark the hyaluronate-binding site.

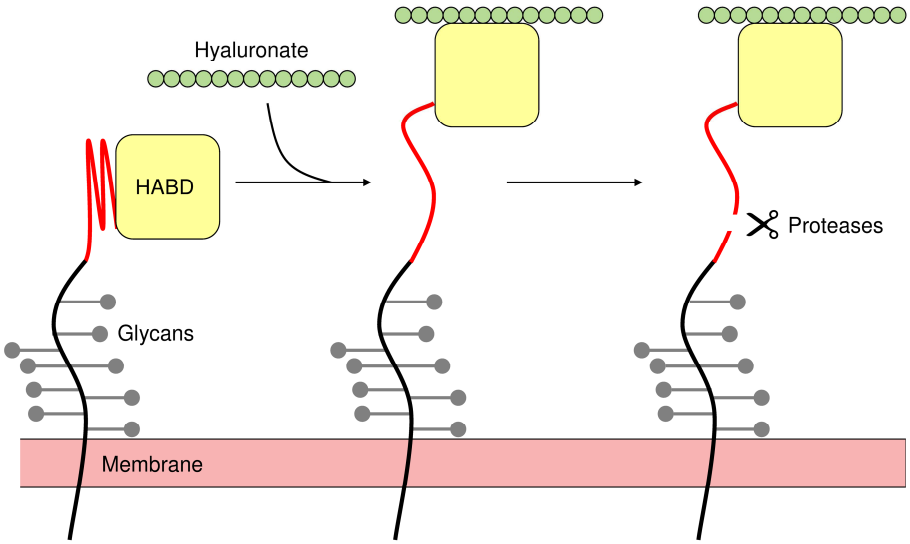

Figure 7: Hyaluronate-induced CD44 shedding
Schematic representation of the hyaluronate-induced structural changes (see also Figure 6) in CD44 hyaluronate-binding domain (HABD) is shown, which promotes proteolytic cleavage in the stem region resulting in CD44 ectodomain shedding. Illustrated according to [64, 70].

5.2.4 CD44 regulation

Hyaluronate binding to CD44 is regulated by a number of factors including cell activation state, receptor clustering, glycosylation pattern, phosphorylation of intracellular Ser291 and receptor dimerization through intramembrane cysteine residues [39, 73-76]. Especially the O-glycosylation pattern together with the cytoplasmic tail of CD44 can affect membrane subdomain localization which can modulate the interaction of CD44 with hyaluronate [77]. CD44 glycosylation also directly controls its binding capacity to fibrin and immobilized fibrinogen [38, 78]. Moreover, CD44 has an inducible character. It is in an inactive (low-affinity) state on the surface of resting T-cells and monocytes and it only binds hyaluronate after the transition to a high-affinity state due to cytokine activation or T-cell activation through the TCR-CD3 [46]. The transition to the high-affinity state is induced by enzymatic removal of terminal sialic acids from the N-linked glycosylation chains on Asn25 and Asn120 [75, 79]. This mechanism targets selected populations of peripheral blood cells to the inflammation site, where they recognize hyaluronate presented on the surface of cytokine-activated endothelial cells and leave the blood stream [62, 63].

Some of the CD44 functions are determined by alternative splicing of the CD44 precursor mRNA [57, 80]. The CD44 gene, located on chromosome 11, spans 50 thousand base pairs of genomic DNA [40] and comprises 20 exons, out of which 10 exons are variable (V1-V10; see Figure 5) [57, 80]. Omitting all these exons gives rise to the

standard or hematopoietic form CD44s (80-85 kDa, 270 extracellular amino acids [45, 56]), which is expressed in most cell types [81], typically on activated leukocytes, where it plays role in their adhesion and trafficking to the inflammation site [82]. The variable exons code for CD44 membrane-proximal region and give rise to at least 20 variant mRNA molecules and at least six out of them were observed also in the form of variant isoform protein product CD44v [82]. Some of the variant isoforms exhibit constitutive hyaluronate-binding activity [73, 83]. Inclusion of exon V3 creates a site for chondroitin sulfate and heparan sulfate modification. This modification enables binding of several growth factors and chemokines, which amplify the immune response [84, 85]. Inclusion of exon V6 creates a binding site for hepatocyte growth factor and vascular endothelial growth factor [85, 86].

5.2.5 CD44 in pathology

CD44 also plays a role in various types of pathological processes, such as extensive inflammatory diseases [87] and cancer, especially in tumor-cell migration and metastasis [47, 72, 81, 88]. Autoimmune inflammatory disorders are characterized by elevated counts of lymphocytes bearing the activated high-affinity-state CD44 [89]. This phenomenon has been observed in patients suffering form lupus erythematosus and chronic arthropathies [90] and in rheumatoid arthritis patients [91]. CD44 has therefore been suggested to play a crucial role in the maintenance and propagation of autoimmune inflammatory diseases [45].

Expression of CD44 variant isoforms can induce metastatic phenotype in locally growing tumor cells [88, 92] and usually correlates with bad prognosis [88]. Inclusion of variant exon V6 has been shown to induce tumor metastasis [92] which is probably caused by a loss of contact with the neighboring cells due to altered adhesion properties of the cells. Proteolysis of the extracellular matrix induced by CD44 variant isoforms [71, 93] facilitates the detachment of tumor cells from the tumor site and their spread outside the original tumor.

Another explanation for the metastatic behavior might be an increased mobility of the cells along the hyaluronate-rich extracellular matrix due to the overexpression of CD44 standard variant CD44s [94]. A significant number of acute lymphoblastic leukemia cases exhibit very high or low CD44 expression on leukemic B-cells when compared to normal B-cell progenitors. This can be used for the detection of minimal residual disease [39, 95,

96]. Low expression of CD44s has been correlated with the aggressive phenotype of some solid tumor types [97-99]. CD44 in cancer cells promotes angiogenesis and the tumor growth, as CD44 has proliferative and anti-apoptotic effects in general [67, 80]. Expression of CD44 is important in the progression of many tumor types [81], is often observed on cancer stem cells [100], and can be a marker of poor prognosis [101]. The cytostatic and pro-apoptotic function of p53 tumor suppressor protein [102] is connected with the inhibition of CD44 expression. The p53 factor binds to the promoter region of the CD44 gene and thus prevents excess mitotic activity in the cell which prevents tumor growth [103]. CD44 interacts with the HER2 tyrosine kinase from the EGF receptor family. Overexpression of HER2 by breast and ovarian cancer cells is an indicator of poor prognosis. CD44s isoform can form interchain disulfide bonds with HER2 and hyaluronate binding to CD44 then stimulates the tyrosine kinase activity of HER2 which triggers signaling pathways that promote cell growth and proliferation [49, 104]. Moreover, CD44 receptor clusters are capable of recruiting matrix metalloprotease 9 to the cell membrane and thus localizing its proteolytic collagenase activity to the tumor cells. This leads to extracellular matrix degradation which by itself facilitates tumor growth but it also releases growth factors and angiogenic factors sequestered in the extracellular matrix, which further stimulates tumor progression [105].

5.2.6 CD44 as a target in cancer therapy

Many approaches in cancer therapy are focused on CD44. CD44 has been identified as a marker of cancer stem cells which represent only a minor population of tumor cells, but are essential for tumor progression and tumor survival during treatment. Cancer stem cells often resist the treatment and this causes cancer relapse or recurrence at distal sites [106]. Cancer initiating cells might thus be targeted through CD44 [57].

One of promising therapeutic approaches is CD44 blocking, the abruption of CD44 interaction with hyaluronate [107]. Hyaluronate induces anti-apoptotic signaling pathways through interaction with the activated CD44 during inflammation and tissue healing or with the constitutively active CD44 on cancer cells [73, 107]. The CD44 inactive state structure on normal cells is different as it is not activated by the specific conditions of the environment [88]. The constitutive hyaluronate-binding by CD44 can be exploited in cancer therapy by four different approaches [107]: (1) small hyaluronate oligomers can be used to compete with the endogenous hyaluronate, (2) soluble CD44 or other

hyaluronate-binding proteins can be used to outcompete the endogenous cell-surface CD44 for hyaluronate binding, (3) the post-transcriptional expression of CD44 variant isoforms can be inhibited using CD44 siRNAs, and (4) hyaluronate binding can be blocked by an anti-CD44 antibody recognizing the hyaluronate-binding site [108-112]. Recently, another approach emerged: (5) first small-molecular inhibitors of the hyaluronate binding to CD44 have been identified by a combinantion of fragment screening and structure-based optimization of the lead compounds. These compounds are based on 1,2,3,4-tetrahydroisoquinoline and they might be potential therapeutic agents in cancer, but also in chronic inflammatory diseases [113].

Small hyaluronate oligomers or antibodies can be further equipped with cytostatic drugs, possibly encapsulated in liposomes, internalized through CD44 [50] and activated inside the tumor cell [114-116]. This approach also increases the drug solubility [116]. The next part is focused on the use of antibodies in CD44-targeted cancer therapy.

5.2.7 Anti-CD44 antibodies in cancer therapy

Known anti-CD44 antibodies recognize a wide variety of antigenic determinants in the CD44 molecule [117]. The standard variant CD44s contains three distinct groups of antigen epitopes. Antibodies recognizing epitope group 1 inhibit T-cell clustering, antibodies recognizing epitope group 2 block hyaluronate binding to CD44, and antibodies recognizing epitope group 3 block lymphocyte adhesion to the epithelium of blood vessels [39, 44]. Antibodies recognizing CD44 can be used to block hyaluronate binding to CD44 and disrupt its interactions with the extracellular matrix [117, 118] or even induce CD44 ectodomain shedding [119]. Activating antibodies can be used to induce CD44 pro-apoptotic signaling [120-122], and anti-CD44 antibodies in general can be used for targeting anti-cancer active substances to the tumor site [123-125].

Several anti-CD44 antibodies targeting cancer stem cells show a promising potential in the preclinical stage [126, 127]. Murine monoclonal antibody H90 activates CD44 signaling that triggers pro-apoptotic and proliferation-inhibitory pathways in human acute myeloid leukemia [121, 122, 128, 129]. Murine monoclonal antibody P245 reduces tumor growth in the mouse model of human basal-like breast cancer and was able to eliminate cancer stem cells and thus prevent breast cancer relapse [130]. Murine monoclonal antibody H4C4 inhibits human pancreatic tumor growth, metastasis, and recurrence in mouse xenografts by inhibiting specific CD44 signaling pathways [127]. Recombinant

human monoclonal antibody GV5 against CD44v8-v10 isoform completely inhibited tumorigenesis of human cervix and larynx carcinomas in mouse models, by inducing antibody-dependent cell cytotoxicity mechanisms [131]. Recombinant humanized antibody RO5429083/RG7356 recognizes a glycosylated part of CD44 present in all CD44 isoforms. The antibody interferes with hyaluronate binding, but does not induce CD44 shedding. It inhibits the growth of head and neck squamous cell carcinoma tumor cells, breast cancer cells, and chronic lymphocytic leukemia cells *in vitro* and in mouse xenografts [118, 132, 133]. The RO5429083/RG7356 antibody has recently reached phase I clinical trials in patients with CD44-positive malignant solid tumors and a study with the antibody alone or an immunotoxin conjugate of the antibody with cytarabine in patients suffering from acute myeloid leukemia [127].

The use of antibodies targeting the CD44v6 variant isoform appears to be the most successful approach in CD44-based cancer immunotherapy [134, 135]. For example, monoclonal antibody 1.1ASML against CD44v6 has been shown to block metastases formation in animal models of cancer [119]. These antibodies are especially potent in the form of radioimmunoconjugates or immunotoxin conjugates. Several clinical phase I trials were performed with murine (U36, BIWA 1), chimeric (chU36), and humanized (BIWA 4) monoclonal antibodies recognizing CD44v6 isoform [135]. Murine antibody U36 conjugated with technetium ^{99m}Tc was successfully tested as a diagnostic tool for the detection of lymph node metastases [136], however, it induced human anti-mouse immune response in later radioimmunotherapy studies with the rhenium ^{186}Re-conjugate [137] and had to be chimerized for further therapeutic applications [138]. The phase I study with the chimerized chU36 antibody has shown reduced adverse immune response while maintaining the effective antibody responses [139-142]. Murine monoclonal antibody BIWA 1 conjugated with ^{99m}Tc has been proven an effective and relatively safe diagnostic tool in a radioimmunoscintigraphy study [143]. Due to the human anti-mouse adverse immune response in the patients [143], a humanized version, BIWA 4 was constructed for further therapeutic applications, also known as Bivatuzumab. Bivatuzumab reached the phase I clinical trials in the form of a radioimmunoconjugate with ^{186}Re [123, 144]. Bivatuzumab was also tested in phase I clinical trials in the form of an immunotoxin conjugate with the cytotoxic drug mertansine. Although these trials seemed very promising, they were abruptly ended after the death of one patient. [124, 145-148].

5.2.8 Monoclonal antibody MEM-85 against CD44

Murine monoclonal antibody MEM-85 of IgG2 class recognizes the CD44 antigen [149]. It was raised against peripheral blood monocytes of a patient suffering form large granular lymphocyte leukemia [149]. The antibody reacts with all peripheral blood monocytes, with granulocytes, and with cell lines including CEM, MOLT-4, ARH-77, HEL, HL-60. MEM-85 reacts very weekly or it does not react at all with cell lines such as Jurkat, Nalm-6, Daudi, and KM3 [32].

MEM-85 has been shown to block hyaluronate binding to CD44 [149, 150] and the antibody binding also induces CD44 shedding, similar to that induced by hyaluronate binding [151]. The HABD epitope recognized by MEM-85 has not yet been unambiguously identified. The epitope is supposed to be localized in the N-terminal part of the HABD [32, 33, 44] and mutational analysis results suggest that residues Lys38, Arg41, and Tyr42 are important for MEM-85 binding [33]. This represents an epitope from the epitope group 2 [32, 44, 150] discussed above. Some consider the MEM-85 epitope to be structural [33], but others have observed MEM-85 binding to SDS-denatured CD44 under non-reducing conditions, which suggests a sequential epitope, stabilized by a disulfide bridge [32].

Antibody MEM-85 might play an important role in diagnostics of some types of malignancies, especially for the detection of minimal residual disease. It might also be of therapeutic interest, as it has been shown to inhibit lung cancer cells growth in murine models (Godar, S., personal communication). This antibody can also be used as a tool for better understanding hyaluronate binding to CD44 and of the subsequent cellular processes, which would be useful for structure-based design of inhibitors of the hyaluronate binding.

6 Aims of the study

This work is a part of two long-term projects: (1) X-ray crystallographic studies of bacterial transcription factors and (2) recombinant antibody fragments targeted against therapeutically relevant human antigens.

Structural studies of selected metabolic repressors from the model bacterium *Bacillus subtilis* aim to elucidate the mechanisms of metabolite repression on the molecular level. Recombinant fragments of monoclonal antibodies targeting selected human antigens are constructed to be used as potential diagnostic or immunotherapeutic agents, and as molecular tools for better structural and functional characterization of their antigens.

Specific research aims:

- Structural characterization of deoxyribonucleoside regulator from *Bacillus subtilis*, the binding of the ligand deoxyribose-5-phosphate, and the effect of the ligand-induced structural changes on the function of the regulator.

- Definition of the binding epitope of monoclonal antibody MEM-85 in the hyaluronate-binding domain of human CD44 receptor and structural characterization of the antibody-induced conformational changes in the antigen and their impact on CD44 function.

7 Publications

1. Crystallization of the effector-binding domain of repressor DeoR from *Bacillus subtilis*

Pisackova, J., Prochazkova, K., Fabry, M. & Rezacova, P. (2013), *Crystal Growth and Design.* 13, 844-848.

$IF_{2013} = 4.558$

2. Structure of the effector-binding domain of deoxyribonucleoside regulator DeoR from *Bacillus subtilis*

Skerlova, J., Fabry, M., Hubalek, M., Otwinowski, Z. & Rezacova, P. (2014), *The FEBS Journal.* 281, 4280-4292.

$IF_{2013/2014} = 3.986$

3. Optimization of the crystallizability of a single-chain antibody fragment*

Skerlova, J., Kral, V., Fabry, M., Sedlacek, J., Veverka, V. & Rezacova, P. (2014), *Acta Crystallographica Section F, Structural Biology and Crystallization Communications.* 70, 1701-1706.

$IF_{2013/2014} = 0.568$

4. Molecular mechanism for the action of the anti-CD44 monoclonal antibody MEM-85

Skerlova, J., Kral, V., Kachala, M., Fabry, M., Bumba, L., Svergun, D. I., Tosner, Z., Veverka V. & Rezacova, P. (2015), under consideration in *Journal of Structural Biology.*

($IF_{2013/2014} = 3.369$)

*Part of the results published in this article was included in the master's thesis of Jana Škerlová (nee Písačková).

7.1 Crystallization of the effector-binding domain of repressor DeoR from *Bacillus subtilis*

Background

Carbon catabolite repression in *Bacillus subtilis*, the model Gram-positive bacterium, has been intensively studied on cellular and molecular level. However, little investigation has been done on structural characterization of the proteins involved in the regulation of the expression of metabolic genes. Structural studies of these repressors would provide the needed insight into the carbon catabolite repression in Gram-positive bacteria as well as the general mechanisms of gene regulation. In this work, we focused on the preparation of crystals of the C-terminal effector-binding domain of the deoxyribonucleoside regulator, DeoR, suitable for X-ray diffraction analysis in order to gain structural information on the effector binding and the effector-induced conformational changes.

Summary

We prepared a recombinant C-terminal effector-binding domain of DeoR (C-DeoR) from *Bacillus subtilis*. Initial crystallization trials yielded thin needle-shaped crystals which could only be optimized to poorly-diffracting rod-shaped crystal clusters. In order to obtain high quality monocrystals suitable for X-ray diffraction experiments, we employed Thermofluor assay to screen for a buffer composition optimal for protein stability, homogeneity, and therefore, crystallizability. In this assay, C-DeoR exhibited the highest melting temperature in citrate buffer, which was identified as the optimal protein storage buffer. The subsequent crystallization screening experiments gave rise to new crystal forms for both the free and effector-bound C-DeoR, that were further optimized to large three-dimensional monocrystals. We collected three complete diffraction data sets for the free and effector-bound C-DeoR. The processed data can be used to solve the structures by molecular replacement using some of the available three-dimensional structures of homologous bacterial repressor proteins. Some of the key results of the publication are summarized in Figure 8.

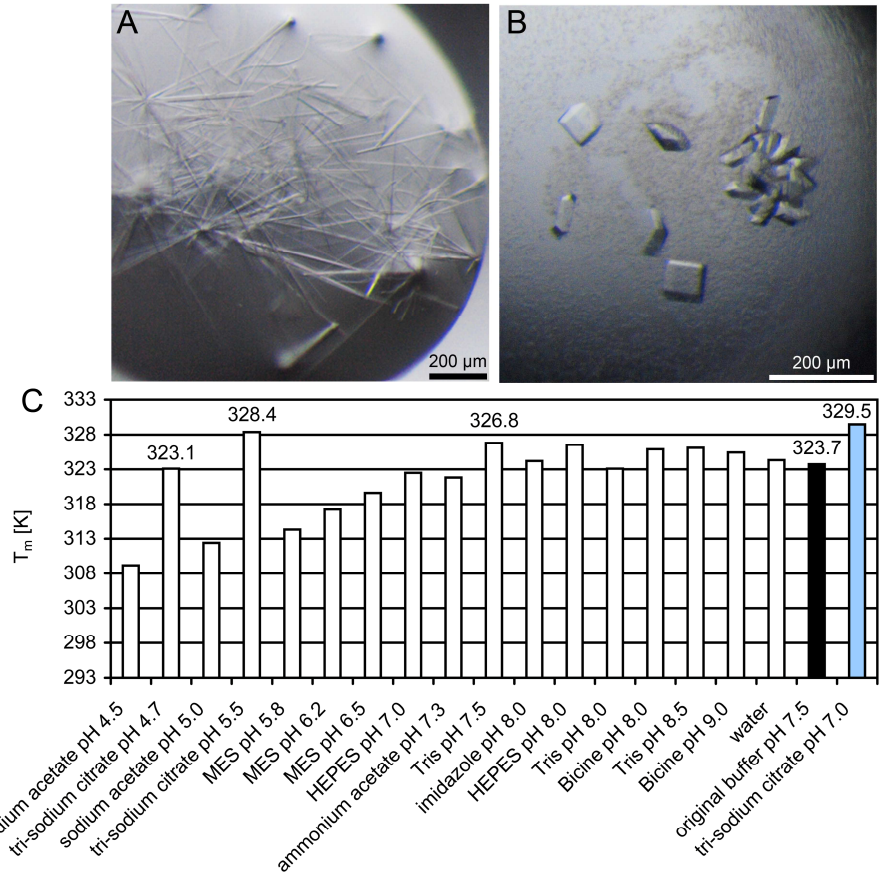

Figure 8: Optimization of the C-DeoR crystals using Thermofluor assay
A: Needle-shaped C-DeoR crystals from the initial crystallization screening in the original protein storage buffer are shown. B: Three-dimensional C-DeoR crystals obtained from the crystallization optimization experiments in the optimized protein storage buffer are shown. C: Screening for the optimal protein storage buffer composition by Thermofluor assay is illustrated by a plot of the C-DeoR melting temperatures (T_m) in various buffers. The original Tris-based protein storage buffer is shown in black and the optimized protein storage buffer in blue.

My contribution

I prepared recombinant C-DeoR protein, performed protein storage buffer optimization by the Thermofluor assay, conducted both the screening and optimization crystallization experiments, participated in X-ray diffraction data collection and processing, and wrote the manuscript.

Crystallization of the effector-binding domain of repressor DeoR from *Bacillus subtilis*. Pisackova, J., Prochazkova, K., Fabry, M. & Rezacova, P. (2013), *Crystal Growth and Design.* 13, 844-848.

CRYSTAL GROWTH & DESIGN

Article

pubs.acs.org/crystal

Crystallization of the Effector-Binding Domain of Repressor DeoR from *Bacillus subtilis*

Published as part of the Crystal Growth & Design virtual special issue on the 14th International Conference on the Crystallization of Biological Macromolecules (ICCBM14)

Jana Písačková,[†,‡] Kateřina Procházková,[†] Milan Fábry,[‡] and Pavlína Řezáčová*[,†,‡]

[†]Institute of Organic Chemistry and Biochemistry, Academy of Sciences of the Czech Republic, Flemingovo nam. 2, Prague 6, Czech Republic

[‡]Institute of Molecular Genetics, Academy of Sciences of the Czech Republic, Videnska 1083, Prague 4, Czech Republic

ABSTRACT: The DeoR repressor of *Bacillus subtilis* negatively regulates the expression of the enzymes needed for the metabolism of deoxyribonucleosides and deoxyribose. To gain structural information on the regulation of DeoR function by a small molecular ligand, we prepared crystals of the C-terminal domain of DeoR in its free form and in complex with the effector molecule deoxyribose-5-phosphate. To develop the optimal procedure for crystallization, we have employed the thermofluor assay as a tool for the optimization of protein crystallizability. The monocrystals of three crystal forms were used to collect complete sets of diffraction data at a synchrotron radiation source and will be used to determine the DeoR crystal structure.

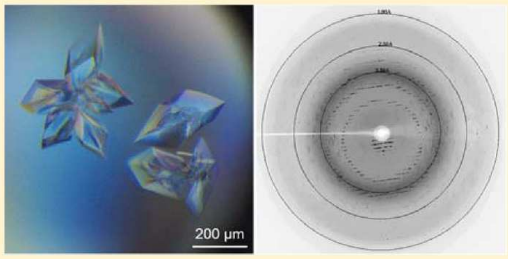

INTRODUCTION

The Gram-positive soil bacterium *Bacillus subtilis* can utilize deoxyribonucleosides and deoxyribose as a source of carbon and energy. After the deoxyribonucleoside uptake into the cell, the catabolic pathway begins with the phosphorolytic cleavage by the nucleoside phosphorylase, yielding the respective base and deoxyribose-1-phosphate, which is converted to deoxyribose-5-phosphate by phosphodeoxyribomutase to be cleaved to the acetaldehyde and glyceraldehyde-3-phosphate by deoxyriboaldolase. The three genes encoding the enzymes required for the metabolism of deoxyribonucleoside and deoxyribose, deoxyriboaldolase (*dra*), nucleoside uptake protein (*nupC*), and pyrimidine nucleoside phosphorylase (*pdp*) are coded by the *dra-nupC-pdp* operon. Their expression is negatively regulated at the level of transcription initiation by the DeoR repressor protein. The *deoR* gene, which codes for the 313 amino acid long repressor protein, is located immediately upstream of the *dra-nupC-pdp* operon.[1] The DeoR-specific operator consists of a palindromic sequence, which is located between the positions −60 and −43 relative to the transcription start site. Also, a direct repeat sequence that is identical to the 3′ half of the palindrome, located downstream to the palindrome, might function as a part of the DeoR binding site.[2] Both deoxyribose-1-phosphate and deoxyribose-5-phosphate induce the expression of the operon, but deoxyribose-5-phosphate seems to be the preferred effector.[2]

The DeoR regulator from *Bacillus subtilis* shows a significant sequence similarity to regulator proteins from the SorC family which occur in various bacteria species. The N-terminal DNA-binding domain is homologous to SorC-like proteins involved in the transcriptional regulation of sugar alcohol catabolism genes. The C-terminal effector-binding domain is homologous to SorC-like proteins involved in the transcriptional regulation of glucose metabolism genes and is probably binding with glyceraldehyde-3-phosphate as the effector molecule.[3]

Regulation of the *deo* operon by the DeoR regulator in *Escherichia coli* has been studied in great detail.[4] Although both the DeoR regulators from *B. subtilis* and *E. coli* contain a helix-turn-helix motif that is typical for many DNA-binding proteins[5,6] and they both form an octamer in the absence of DNA, there is very little sequence similarity between them, and there is no similarity between their DNA operator sites.[2,3,7]

To gain structural information on the effector binding by DeoR, we have prepared a recombinant effector-binding domain of the DeoR repressor protein from *B. subtilis* (referred to as C-DeoR) for X-ray crystallography analysis. We have developed the optimal protocols for the crystallization of C-DeoR free form and for C-DeoR complex with the effector molecule deoxyribose-5-phosphate. We have employed the thermofluor assay as a tool for the optimization of protein crystallizability[8] and obtained monocrystals of three crystal forms which are suitable for diffraction data collection.

Received: October 22, 2012
Revised: December 12, 2012
Published: December 19, 2012

EXPERIMENTAL SECTION

Protein Preparation. The coding sequence for the C-terminal effector-binding domain of DeoR, referred to here as C-DeoR (residues 56−313 of the NCBI reference sequence NP_391822.1), was cloned into the pET151/D-TOPO vector (Invitrogen, USA). The vector coded for an N-terminal His_6 tag, V5 epitope, and the tobacco etch virus (TEV) protease recognition site.

The C-DeoR protein was expressed and purified analogously to the protocol developed for other bacterial repressors.[9] The protein was overexpressed in *E. coli* BL21 (DE3) at 310 K on an LB broth (Sigma Aldrich, USA) supplemented with 0.8% (v/v) glycerol and 20 μg/mL ampicillin. At an OD_{600nm} value of about 1, the protein expression was induced with 1 mM isopropyl-β-D-thiogalactopyranoside. The cultivation proceeded at 293 K for 5 h and the cells were harvested by centrifugation.

The bacterial cells were lysed by sonication in 5 vol of lysis buffer (50 mM Tris·HCl, pH 7.5, 500 mM NaCl, 10 mM imidazole, 5% (v/v) glycerol, and 1 mM phenylmethylsulfonyl fluoride). Clarified lysate was purified using nickel-chelation chromatography on a His-select Nickel Affinity Gel column (Sigma Aldrich, USA) equilibrated in lysis buffer. To elute His_6-tagged protein, 250 mM imidazole in lysis buffer was used. The His_6 tag was cleaved off by a recombinant His_6-tagged TEV protease during an overnight dialysis against the lysis buffer at 298 K. The TEV protease and the cleaved His_6 tag were removed using a second nickel-chelation chromatography step. The protein was dialyzed against the protein storage buffer (either 20 mM Tris·HCl pH 7.5, 250 mM NaCl, 0.02% (v/v) β-mercaptoethanol or 20 mM trisodium citrate pH 7.0, 150 mM NaCl, 0.02% (v/v) β-mercaptoethanol), concentrated on Amicon Ultra concentrators (Millipore, USA), aliquoted, and stored at 203 K.

The protein was purified with a yield of 8 mg of protein from 1 L of bacterial culture. The protein purity was assessed by a silver-stained SDS-PAGE to be greater than 95% (see Figure 1, lane 2).

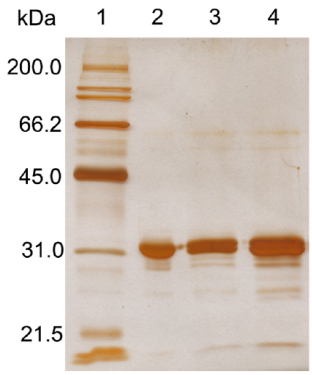

Figure 1. SDS-PAGE analysis of the C-DeoR protein preparation and C-DeoR crystals. 15% gel visualized by silver staining, lane 1 - protein molecular weight marker (BioRad, USA), lane 2 - 1.1 μg of purified C-DeoR protein, lane 3 - dissolved C-DeoR co-crystal with deoxyribose-5-phosphate, lane 4 - dissolved C-DeoR crystal.

In attempts to optimize the crystal quality, the protein was further purified using ion-exchange chromatography on the MonoQ column (Amersham Biosciences, USA) in 10 mM Tris·HCl pH 7.5 containing 0.02% (v/v) β-mercaptoethanol with a segmented gradient of sodium chloride using the Äkta Basic FPLC system (Amersham Biosciences, USA). The protein eluted as a single peak at 320 mM NaCl.

Crystallization Screening. The C-DeoR protein in the concentration of 14.6−22 mg/mL in a protein storage buffer was used for the initial crystallization screening. In some experiments the protein solution was supplemented with 50 mM deoxyribose-5-phosphate. The screening was performed by the vapor diffusion method with the help of the Gryphon crystallization workstation (Art Robbins Instruments, USA) in 96-well sitting drop Intelli-plates (Art Robbins Instruments, USA) using the JCSG+ Suite (Qiagen, Netherlands). A total volume of 450 nL of the protein and precipitant solution mixture in the ratio 1:2 or 2:1 was equilibrated over a 50 μL reservoir solution. Crystallization plates were stored at 291 K and checked regularly.

Crystallization Optimization. The experiments were set up manually in the hanging drop format in VDX48 plates (Hampton Research, USA) by mixing the protein and precipitant solutions in the ratio 1:2, 2:1 (total volume of 1.5 or 3 μL), or 1:1 (total volume of 2 μL). The reservoir volume was 150 or 200 μL and the temperature for all experiments was 291 K.

During the optimization of the initial crystallization conditions, the concentration of the crystallization solution as well as the protein concentration were varied, the effect of various additives (agarose, *n*-octyl-γ-D-glucoside, and *n*-dodecyl-γ-D-maltoside, glycerol, ethylene glycol, and 2-methyl-2,4-pentanediol) was tested. In some experiments, the reservoir was overlaid by 100 μL of oil barrier (Al's Oil, Hampton Research, USA) to slow down the evaporation.[10] To lower the number of crystallization nuclei and precipitation observed immediately after drop mixing, a crystallization mixture containing 6 μL of C-DeoR in the concentration of 22 mg/mL supplemented with 50 mM deoxyribose-5-phosphate, and 3 μL of condition number 77 of the JCSG+ Screen was incubated at 291 K. The mixture was centrifuged (for 20 min at 18500g) at time intervals of 30, 90, and 180 min from mixing, and the crystallization drops were set up after centrifugation. This approach did not help to lower the number of crystallization nuclei or the precipitation.

Counter-diffusion crystallization experiments were set up in single capillaries using the three-layer configuration.[11] Glass capillaries of 75 mm lengths and inner diameters of 0.2 mm (Hirschmann, Germany) were placed into the Granada Crystallization Boxes (Triana Sci&Tech, Spain) for storage. Four microliters of the protein solution at a concentration of 16 mg/mL were separated from the 40 μL of precipitant solution (200 mM trisodium citrate pH 5.5, 25% (w/v) PEG 3350) by 4 μL of 0.5% (w/v) low melting agarose (BioRad, USA).

The composition of protein crystals was analyzed by a Laemmli SDS-PAGE analysis of the crystals extensively washed by mother liquor and dissolved in water.

Thermofluor. Thermofluor assay was performed using real-time PCR LightCycler 480 II (Roche, Switzerland). The stabilizing effect of 16 buffers at a concentration of 100 mM was tested in the presence or absence of 200 mM NaCl following the procedure described in Ericsson et al., 2006[8] (phosphate buffers were excluded from the screening, because of possible interference with the ligand binding). The protein at a concentration of 0.08 mg/mL was tested in the presence of 8× concentrated Sypro Orange (Invitrogen, USA) in the total reaction volume of 25 μL in the LightCycler 480 Multiwell Plate 96 (Roche, Switzerland). The plate was sealed with the LightCycler 480 Sealing Foil (Roche, Switzerland), and a temperature gradient from 293 to 368 K with a rate of 0.83 K/min was applied. The fluorescence intensity was recorded at 580 nm, and the excitation wavelength was 465 nm. The melting temperature values, corresponding to the inflection points of the melting curves, were determined as the minima of the negative first derivative using the Roche LightCycler 480 SW 1.5 software.

Diffraction Data Collection and Processing. For the diffraction experiments, crystals were mounted into nylon loops (Hampton Research, USA), quick-soaked (for 3−5 s) in cryoprotectant solution containing mother liquor supplemented with 10% or 20% (v/v) glycerol, flash-cooled, and then stored in liquid nitrogen.

Three complete diffraction data sets were collected at 100 K with a 0.91841 Å wavelength and a MAR Mosaic (225 mm) detector at beamline MX14.2 of the BESSY, Berlin, Germany.[12] The crystal parameters and data collection statistics are listed in Table 1. All diffraction data sets were processed using the HKL-3000 package.[13]

dx.doi.org/10.1021/cg301551v | *Cryst. Growth Des.* 2013, 13, 844−848

Table 1. Data Collection Statistics for the Crystals of C-DeoR[a]

crystal form	I	II	III
deoxyribose-5-phosphate	+	+	−
wavelength (Å)	0.91841	0.91841	0.91841
resolution range (Å)	50−1.65 (1.71−1.65)	50−1.60 (1.66−1.60)	50−1.90 (1.97−1.90)
space group	$P222_1$	$C222_1$	$P3_1$ or $P3_2$
unit-cell parameters (Å; °)	40.4, 78.4, 91.3; 90.0, 90.0, 90.0	76.9, 78.9, 91.4; 90.0, 90.0, 90.0	63.3, 63.3, 150; 90.0, 90.0, 120.0
total no. of measured intensities[b]	218165	194099	251635
number of unique reflections	32823 (2759)	34660 (2284)	52424 (5253)
multiplicity	6.6 (5.0)	5.6 (3.3)	4.8 (4.5)
average $I/\sigma(I)$	59.9 (2.0)	42.8 (2.8)	44.7 (2.1)
completeness (%)	90.6 (77.4)	93.5 (62.3)	98.8 (98.2)
R_{merge}[c] (%)	3.5 (35.9)	4.0 (25.5)	4.4 (75.1)
overall B factor from Wilson plot (Å^2)	28.4	18.6	33.6
Matthews coefficient (A^3/Da)	2.56	2.42	3.02
no. of molecules in asymmetric unit	1	1	2
solvent content (%)	51	49	59

[a]The numbers in parentheses refer to the highest resolution shell. [b]The criterion for the observed reflection $I/\sigma(I) > 0$. [c]$R_{merge} = 100\sum_{hkl}\sum_i|I_i(hkl) - \langle I(hkl)\rangle|/\sum_{hkl}\sum_i I_i(hkl)$, where $I_i(hkl)$ is an individual intensity of the ith observation of reflection hkl and $\langle I(hkl)\rangle$ is the average intensity of reflection hkl with summation over all data.

RESULTS AND DISCUSSION

The C-terminal effector-binding domain of DeoR from *B. subtilis* (residues 56−313, referred to as C-DeoR) was expressed in *E. coli* and purified to homogeneity (Figure 1, lane 2). The recombinant C-DeoR contained 258 amino acid residues of its native sequence and an N-terminal sequence GIDPFT, which remained upon cleavage by the TEV protease.

The initial crystallization screening of C-DeoR in the presence of 50 mM deoxyribose-5-phosphate was performed with a protein stored in a buffer used in protein purification and with a JCSG+ Suite (Qiagen, Netherlands). Needle-shaped crystals (typical crystals shown in Figure 2A) were obtained after several days in 8 out of 96 conditions (see Figure 3A). Condition number 2 from the JCSG+ Screen (Figure 2A) was chosen for further optimization.

In the optimization experiments, a wide range of approaches was used to lower the number of crystals and increase their size and volume: (1) protein concentration was varied (8−18.5 mg/mL); (2) precipitant concentration was varied (12−20% (w/v) PEG 3000); (3) various additives known to affect protein solubility and nucleation were added (0.010−0.017% (w/v)

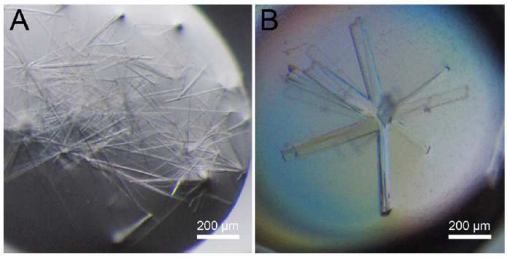

Figure 2. C-DeoR crystals obtained from the initial screening and optimization in the protein storage buffer containing 20 mM Tris·HCl pH 7.5, 250 mM NaCl, and 0.02% (v/v) β-mercaptoethanol: panel A: crystals from the initial screening (14.6 mg/mL C-DeoR, 50 mM deoxyribose-5-phosphate, 450 nL droplet, protein to precipitant ratio 1:2, condition number 2 from the JCSG+ Screen (0.1 M trisodium citrate pH 5.5, 20% (w/v) PEG 3000); panel B: optimized crystals (14.6 mg/mL C-DeoR, 50 mM deoxyribose-5-phosphate, 2 μL droplet, protein to precipitant ratio 1:1, 20% (v/v) ethylene glycol, 80% (v/v) condition number 2 from the JCSG+ Screen: 0.08 M trisodium citrate pH 5.5, 16% (w/v) PEG 3000. The crystals grew to their final size in 1 day.

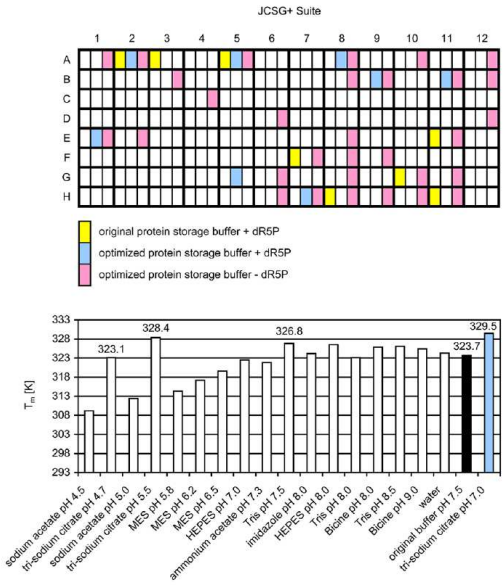

Figure 3. The crystallization screening and protein storage buffer optimization by the thermofluor assay: panel A: the crystallization screening plate scheme: the conditions of JCSG+ Suite (Qiagen, Netherlands) yielding crystals or microcrystals are highlighted in the colors for the original and the optimized protein storage buffers in the presence (+) or absence (−) of deoxyribose-5-phosphate (dR5P); panel B: the melting temperatures (T_m) obtained by thermofluor assay are shown for 16 screened buffers and water (white columns), the original protein storage buffer containing 20 mM Tris·HCl pH 7.5, 250 mM NaCl, and 0.02% (v/v) β-mercaptoethanol (black column) and the most stabilizing buffer containing 100 mM trisodium citrate pH 7.0 (blue). T_m values in Kelvins are indicated for the selected buffers.

agarose; 0.5% (w/v) of *n*-octyl-γ-D-glucoside or *n*-dodecyl-γ-D-maltoside; 10−40% (v/v) of glycerol or ethylene glycol or 2-methyl-2,4-pentanediol); (4) the capillary crystallization method was performed to screen a wide range of precipitant concentrations; and (5) the purity of the protein was improved by purification on ion-exchange chromatography. This extensive effort yielded plate-like crystals with maximal dimensions of 300 × 80 × 20 μm (Figure 2B) and a poor diffraction quality.

As optimization of the crystallization conditions was not successful we decided to change the protein storage buffer to achieve maximal protein solubility and stability. The optimization of the protein storage buffer composition was performed using thermofluor-based assay following the procedure described by Ericsson et al., 2006.[8] The effect of 16 buffers on protein thermal stability was tested in the presence or absence of 200 mM NaCl. The results of the analysis (Figure 3B) revealed the specific stabilizing effect of trisodium citrate pH 4.7 and pH 5.5; the optimal pH value for protein stability was around pH 7.5. The buffer combining a higher pH with trisodium citrate (100 mM trisodium citrate pH 7.0) showed the highest stabilizing effect with the melting temperature (T_m) being about 6 K higher than the original protein storage buffer. Phosphate buffers were not considered in this analysis, because of the possible interference with the ligand binding. The binding of the phosphate ion by bacterial repressors was shown before.[14,15] The addition of 200 mM NaCl did not increase protein stability in most buffers, and the difference between the T_m values for 100 mM trisodium citrate pH 7.0 in the presence and absence of 200 mM NaCl was not significant (data not shown). In the optimized buffer composition, 150 mM NaCl was included, because the precipitation of protein at high concentration was observed in the buffer without any salt.

On the basis of the results of thermofluor assay, the composition of the protein storage buffer was thus changed to 20 mM trisodium citrate pH 7.0, 150 mM NaCl, 0.02% (v/v) β-mercaptoethanol.

C-DeoR protein was dialyzed into the protein storage buffer with an optimized composition and the crystallization screening procedure using the JCSG+ Suite was repeated. C-DeoR supplemented with 50 mM deoxyribose-5-phosphate yielded crystals in 8 out of 96 conditions which were different from those obtained in the screening in the original protein storage buffer (Figure 3A). Most of the crystals were needle-shaped or plate-like, and often clustered, but condition number 77 (0.1 M HEPES pH 7.5, 12% (w/v) PEG 3350, 5 mM $CoCl_2$, 5 mM $CdCl_2$, 5 mM $MgCl_2$, and 5 mM $NiCl_2$) yielded three-dimensional crystals which grew to their final size of 70 × 60 × 40 μm in 5 days. This condition was therefore selected for further optimization.

An analogous crystallization screening experiment was conducted with C-DeoR in the optimized storage buffer in the absence of deoxyribose-5-phosphate. The initial crystals were obtained in 31 out of 96 conditions (see Figure 3A) after several days. Most of the crystals were needle-shaped or plate-like, and often clustered, but condition number 15 (0.1 M Bicine pH 8.5, and 20% (w/v) PEG 6000) yielded three-dimensional crystals with a size of 130 × 120 × 120 μm in one day and was therefore selected for further optimization. Three-dimensional crystals were also obtained in condition number 28 (0.1 M HEPES pH 6.5, and 10% (w/v) PEG 6000) after 7 days, but these were not optimized, because the optimization of the crystals from condition number 15 was already successful.

The optimization of the protein and precipitant concentration led to large three-dimensional crystals with a good diffraction quality allowing the collection of three complete data sets from three crystal forms (Figure 4). The presence of

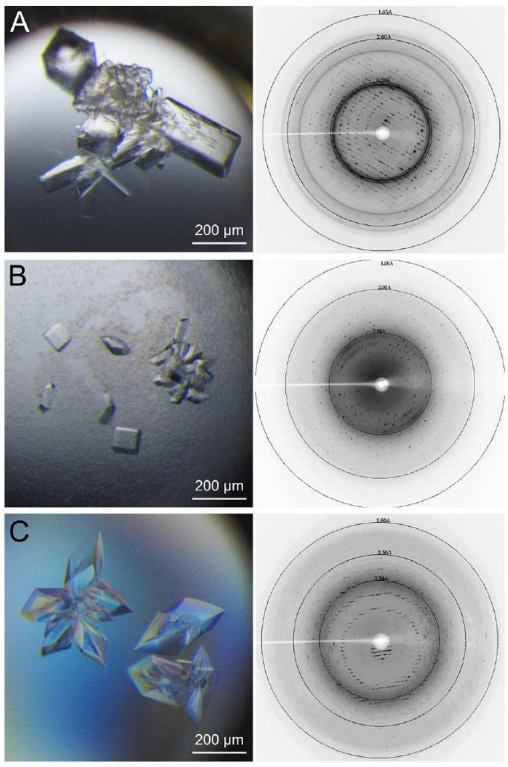

Figure 4. The optimized C-DeoR crystals and the corresponding X-ray diffraction images: panel A: crystal form I, panel B: crystal form II, panel C: crystal form III. For crystallization conditions see text; for diffraction data statistics see Table 1.

the C-DeoR protein in the crystals was confirmed by an SDS-PAGE analysis of the crystals washed in a cryoprotectant solution and dissolved in water as shown in Figure 1.

The crystals belonging to the $P222_1$ space group (crystal form I, Figure 4A, Table 1) were obtained for C-DeoR at 22 mg/mL in the presence of 50 mM deoxyribose-5-phosphate in conditions containing 0.08 M HEPES pH 7.5, 9.6% (w/v) PEG 3350, 4 mM $CoCl_2$, 4 mM $CdCl_2$, 4 mM $MgCl_2$, and 4 mM $NiCl_2$. A complete data set at a resolution of 1.65 Å was collected from a crystal soaked in mother liquor supplemented with 20% (w/v) glycerol (see Table 1 for data statistics).

The crystals belonging to the $C222_1$ space group (crystal form II, Figure 4B, Table 1) were obtained for C-DeoR at 16.5 mg/mL in the presence of 50 mM deoxyribose-5-phosphate in conditions containing 0.08 M HEPES pH 7.5, 9.6% (w/v) PEG 3350, 4 mM $CoCl_2$, 4 mM $CdCl_2$, 4 mM $MgCl_2$, and 4 mM $NiCl_2$. A complete data set at a resolution of 1.60 Å was collected from a crystal soaked in mother liquor supplemented with 20% (w/v) glycerol (see Table 1 for data statistics).

The crystals exhibiting the symmetry of space group *P*3 with systematic absences indicating the presence of a 3_1 or 3_2 screw axis (crystal form III, Figure 4C, Table 1) were obtained for C-DeoR at 12.5 mg/mL in the absence of deoxyribose-5-phosphate. The crystallization conditions contained 0.1 M Bicine pH 8.5, and 20% (w/v) PEG 6000. A complete data set at a resolution of 1.90 Å was collected from a crystal soaked in mother liquor supplemented with 10% (w/v) glycerol (see Table 1 for data statistics).

The calculated Matthews coefficient values (Table 1) suggested the presence of one molecule of C-DeoR in the asymmetric unit for the ligand-bound C-DeoR and two molecules for the ligand-free form. This correlates with the results of the oligomerization analysis done by size-exclusion chromatography which showed that a dimer is the biological unit of C-DeoR (data not shown).

The diffraction data will be used to determine the structure of C-DeoR by the molecular replacement using the available structures of homologous proteins: the putative sugar-binding transcriptional regulator from *Arthrobacter aurescens* TC1 (PDB code 3NZE; 52% sequence similarity, 30% sequence identity for 259 residues), probable *sor* operon regulator from *Shigella flexneri* (PDB code 3EFB; 49% sequence similarity, 31% sequence identity for 265 residues) and sorbitol operon regulator SorC from *Klebsiella pneumoniae* (PDB code 2W48, 50% sequence similarity, 30% sequence identity for 246 residues).[16]

■ AUTHOR INFORMATION

Corresponding Author

*Tel.: +420220183144; e-mail: rezacova@uochb.cas.cz.

Notes

The authors declare no competing financial interest.

J.P. is supported presently in part by Faculty of Science, Charles University in Prague.

■ ACKNOWLEDGMENTS

This work was supported by the Ministry of Education of the Czech Republic (research projects ME08016 and LK11205), and research projects AV0Z40550506 and AV0Z50520514 awarded by the Academy of Sciences of the Czech Republic and research project GA203/09/0820 awarded by Grant Agency of the Czech Republic. Diffraction data have been collected on MX14.2 operated by the Helmholtz-Zentrum Berlin (HZB) at the BESSY II electron storage ring (Berlin-Adlershof, Germany).[12] Authors wish to thank Devon Maloy for critical proofreading of the manuscript.

■ ABBREVIATIONS

DeoR, deoxyribonucleoside regulator; C-DeoR, C-terminal effector-binding domain of DeoR; *dra*, deoxyribonuclease coding gene; *nupC*, nucleoside uptake protein coding gene; *pdp*, pyrimidine nucleoside phosphorylase coding gene; *deo*, *E. coli* operon coding for enzymes involved in deoxyribonucleosides metabolism; SorC, sorbitol operon regulator; dR5P, deoxyribose-5-phosphate; T_m, melting temperature; *sor*, operon encoding enzymes for the metabolism of D-glucitol, sucrose and L-sorbose

■ REFERENCES

(1) Saxild, H. H.; Andersen, L. N.; Hammer, K. *J. Bacteriol.* **1996**, *178*, 424−434.
(2) Zeng, X.; Saxild, H. H. *J. Bacteriol.* **1999**, *181*, 1719−1727.
(3) Zeng, X.; Saxild, H. H.; Switzer, R. L. *J. Bacteriol.* **2000**, *182*, 1916−1922.
(4) Amouyal, M.; Mortensen, L.; Buc, H.; Hammer, K. *Cell* **1989**, *58*, 545−551.
(5) Harrison, S. C.; Aggarwal, A. K. *Annu. Rev. Biochem.* **1990**, *59*, 933−69.
(6) Pabo, C. O.; Sauer, R. T. *Annu. Rev. Biochem.* **1984**, *53*, 293−321.
(7) Dandanell, G.; Valentin-Hansen, P.; Larsen, J. E.; Hammer, K. *Nature* **1987**, *325*, 823−826.
(8) Ericsson, U. B.; Hallberg, B. M.; Detitta, G. T.; Dekker, N.; Nordlund, P. *Anal. Biochem.* **2006**, *357*, 289−298.
(9) Prochazkova, K.; Cermakova, K.; Pachl, P.; Sieglova, I.; Fabry, M.; Otwinowski, Z.; Rezacova, P. *Acta Crystallogr.* **2012**, *D68*, 176−185.
(10) Chayen, N. E. *Structure* **1997**, *5*, 1269−1274.
(11) Gavira, J. A.; de Jesus, W.; Camara-Artigas, A.; Lopez-Garriga, J.; Garcia-Ruiz, J. M. *Acta Crystallogr.* **2006**, *F62*, 196−199.
(12) Mueller, U.; Darowski, N.; Fuchs, M. R.; Forster, R.; Hellmig, M.; Paithankar, K. S.; Puhringer, S.; Steffien, M.; Zocher, G.; Weiss, M. S. *J. Synchrotron Radiat.* **2012**, *19*, 442−449.
(13) Minor, W.; Cymborowski, M.; Otwinowski, Z.; Chruszcz, M. *Acta Crystallogr.* **2006**, *D62*, 859−866.
(14) Rezacova, P.; Krejcirikova, V.; Borek, D.; Moy, S. F.; Joachimiak, A.; Otwinowski, Z. *Proteins* **2007**, *69*, 679−682.
(15) Rezacova, P.; Kozisek, M.; Moy, S. F.; Sieglova, I.; Joachimiak, A.; Machius, M.; Otwinowski, Z. *Mol. Microbiol.* **2008**, *69*, 895−910.
(16) de Sanctis, D.; McVey, C. E.; Enguita, F. J.; Carrondo, M. A. *J. Mol. Biol.* **2009**, *387*, 759−770.

7.2 Structure of the effector-binding domain of deoxyribonucleoside regulator DeoR from *Bacillus subtilis*

Background

In this work, which followed the results of the previous publication "Crystallization of the effector-binding domain of repressor DeoR from *Bacillus subtilis*", we aimed at a detailed structural characterization of the C-terminal effector-binding domain of deoxyribonucleoside regulator, DeoR, a repressor protein taking part in the carbon catabolite repression in *Bacillus subtilis*. In particular, we were interested in the structural aspects of effector binding by DeoR. From the known three-dimensional structures of other metabolic regulators from *Bacillus subtilis*, we can say that although the effector-binding domains of the individual repressors represent common conserved folds, the molecular mechanisms of the regulatory function of each repressor are quite unique. Therefore, a detailed study of the DeoR molecular mechanics would contribute to complex understanding of prokaryotic transcriptional regulation.

Summary

We determined crystal structures of the effector-binding domain of the deoxyribonucleoside regulator (C-DeoR) from *Bacillus subtilis* both in the free form and in the complex with the effector deoxyribose-5-phosphate. The effector-bound C-DeoR structure revealed a unique mode of effector binding through a reversible covalent Schiff-base double bond to a lysine residue in the effector-binding site. This is the first case of a transcriptional factor that binds the effector molecule covalently. The physiological nature of this covalent effector binding mode was confirmed by mutational analysis combined with differential scanning fluorimetry (Thermofluor assay) and by mass spectrometry analysis of the formation of the Schiff-base complex in solution. Detailed structural analysis of the free and effector-bound C-DeoR structures, supported by the size-exclusion chromatography data, allowed us to propose a model for the DeoR function as a molecular switch. Some of the key results of the publication are summarized in Figure 9.

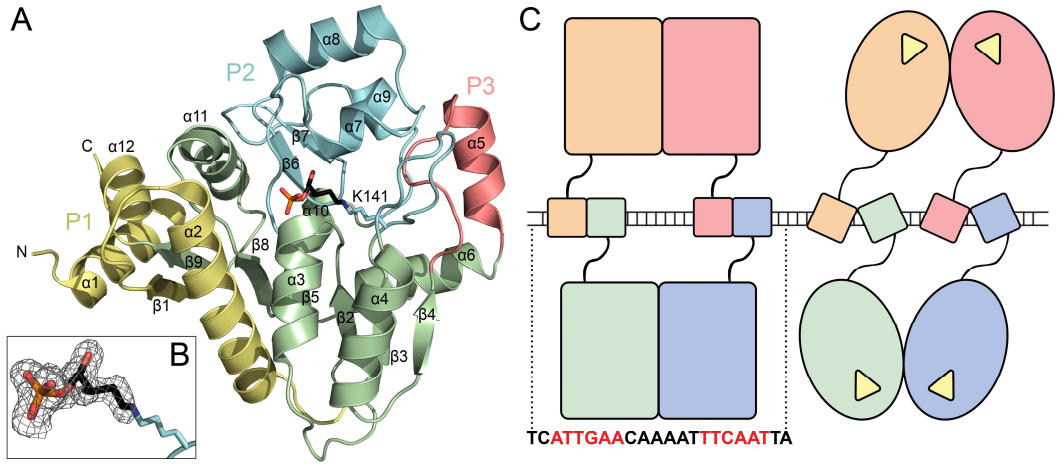

Figure 9: C-DeoR crystal structure and a model of DeoR function
A: Overall structure cartoon diagram with the topology description is shown for C-DeoR in complex with the effector deoxyribose-5-phosphate (shown in sticks). Double-Rossman-fold core (green) and peripheral subdomains (P1, P2, P3) are highlighted in colors. B: A detail of the effector molecule covalently bound to the effector-binding-site lysine residue is shown with the difference electron density map for the ligand contoured at 2.5 σ. C: Schematic representation of the tetrameric assembly of the full-length DeoR on the DNA operator site is shown in the high-affinity free state (left) and in the low-affinity effector-bound induced state (right).

My contribution

I participated in determination of crystal structure of the effector-bound C-DeoR, I determined the structure of free C-DeoR, refined both structure models and performed complete structure analysis. I purified the mutant and full-length C-DeoR proteins, performed the differential scanning fluorimetry (Thermofluor) assay and size-exclusion chromatography, prepared C-DeoR – effector adduct samples for mass spectrometry, and wrote the manuscript.

Structure of the effector-binding domain of deoxyribonucleoside regulator DeoR from *Bacillus subtilis.* Skerlova, J., Fabry, M., Hubalek, M., Otwinowski, Z. & Rezacova, P. (2014), *The FEBS Journal.* 281, 4280-4292.

the FEBS Journal

Structure of the effector-binding domain of deoxyribonucleoside regulator DeoR from *Bacillus subtilis*

Jana Škerlová[1,2], Milan Fábry[2], Martin Hubálek[1], Zbyszek Otwinowski[3] and Pavlína Řezáčová[1,2]

1 Institute of Organic Chemistry and Biochemistry, Academy of Sciences of the Czech Republic, Prague, Czech Republic
2 Institute of Molecular Genetics, Academy of Sciences of the Czech Republic, Prague, Czech Republic
3 UT Southwestern Medical Center, Dallas, TX, USA

Keywords
dimeric interface; effector binding; Schiff base; transcription repressor; X-ray crystallography

Correspondence
P. Řezáčová, Institute of Organic Chemistry and Biochemistry, Academy of Sciences of the Czech Republic, Flemingovo nam. 2, Prague 6, Czech Republic
Fax: +420 220 183 144
Tel: +420 220 183 144
E-mail: rezacova@uochb.cas.cz

(Received 27 March 2014, revised 15 May 2014, accepted 16 May 2014)

doi:10.1111/febs.12856

Deoxyribonucleoside regulator (DeoR) from *Bacillus subtilis* negatively regulates expression of enzymes involved in the catabolism of deoxyribonucleosides and deoxyribose. The DeoR protein is homologous to the sorbitol operon regulator family of metabolic regulators and comprises an N-terminal DNA-binding domain and a C-terminal effector-binding domain. We have determined the crystal structure of the effector-binding domain of DeoR (C-DeoR) in free form and in covalent complex with its effector deoxyribose-5-phosphate (dR5P). This is the first case of a covalently attached effector molecule captured in the structure of a bacterial transcriptional regulator. The dR5P molecule is attached through a Schiff base linkage to residue Lys141. The crucial role of Lys141 in effector binding was confirmed by mutational analysis and mass spectrometry of Schiff base adducts formed in solution. Structural analyses of the free and effector-bound C-DeoR structures provided a structural explanation for the mechanism of DeoR function as a molecular switch.

Databases
Atomic coordinates and structure factors for crystal structures of free C-DeoR and the covalent Schiff base complex of C-DeoR with dR5P have been deposited in the Protein Data Bank with accession codes 4OQQ and 4OQP, respectively.

Structured digital abstract
•C-DeoR and C-DeoR bind by x-ray crystallography (View interaction)
•DeoR and DeoR bind by molecular sieving (1, 2)

Introduction

The Gram-positive soil bacterium *Bacillus subtilis* can utilize deoxyribonucleosides and deoxyribose as sources of carbon and energy. The deoxyribonucleoside catabolic pathway involves three steps. First, the deoxyribonucleosides enter the cell, a process mediated by nucleoside uptake protein C. In the second step, the deoxyribonucleosides are cleaved by pyrimidine nucleoside phosphorylase (Pdp), yielding

Abbreviations
AU, asymmetric unit; C-DeoR, C-terminal domain of deoxyribonucleoside regulator; CggR, central glycolytic gene regulator; DeoR, deoxyribonucleoside regulator; dR1P, deoxyribose-1-phosphate; dR5P, deoxyribose-5-phosphate; Dra, deoxyriboaldolase; DSF, differential scanning fluorimetry; GabR, putative γ-aminobutyrate aminotransferase; Pdp, pyrimidine nucleoside phosphorylase; SorC, sorbitol operon regulator; TLS, translation, libration, screw.

deoxyribose-1-phosphate (dR1P), which is then converted to deoxyribose-5-phosphate (dR5P) by phosphodeoxyribomutase. In the third key step, dR5P is cleaved by deoxyriboaldolase (Dra) to acetaldehyde and glyceraldehyde-3-phosphate, which can enter further metabolic pathways. The genes that encode the three key enzymes of deoxyribonucleoside catabolism are grouped in one operon: *dra-nupC-pdp*. Expression of this operon is repressed at the level of transcription initiation by deoxyribonucleoside regulator (DeoR) protein, which is encoded by the *deoR* gene located immediately upstream of the *dra-nupC-pdp* operon [1].

The DeoR transcriptional regulator is homologous to the sorbitol operon regulator (SorC) family of regulatory proteins present in a wide range of bacterial species. These proteins typically contain a small N-terminal DNA-binding domain, which is responsible for the recognition and binding of the operator DNA, and a large C-terminal effector-binding domain, which is responsible for oligomerization of the regulator and transmission of the effector signal to the DNA-binding domain. The classical helix–turn–helix DNA-binding domain of DeoR (residues 1–55) shows significant sequence similarity to that of SorC-like proteins that regulate the catabolism of sugar alcohols [2,3]. DeoR recognizes a palindromic operator sequence located between positions 60 and 43 relative to the transcription start site, possibly together with an additional direct repeat sequence identical to the 3′ half of the palindrome, which is located downstream of the palindrome: 5′-ATTGAACAAAATTTCAATTACCAATTTACATATGTTCAA-3′ (the palindromic sequence and the direct repeat are underlined) [2].

The effector-binding domain of DeoR (residues 56–313) is homologous to that of SorC-like proteins that regulate glucose metabolism [3]. Both dR1P and dR5P have been shown to induce expression of the *dra-nupC-pdp* operon, but dR5P is considered the preferred effector [2]. To date, no crystal structures of DeoR from *B. subtilis* or its individual domains are available.

To gain structural information about effector recognition by DeoR, we prepared a recombinant effector-binding domain of DeoR from *B. subtilis* (referred to as C-DeoR) and determined crystal structures of C-DeoR in its free form and in complex with the effector dR5P. This structural information revealed that the effector molecule forms a Schiff base linkage with a lysine side chain in the C-DeoR effector-binding site. The physiological relevance of this interaction was supported by mutational and mass spectrometry analyses.

Results and discussion

Overall structure description and quality

The structure of C-DeoR (residues 56–313) in complex with the effector dR5P was solved by molecular replacement using phases derived from a homologous putative sugar-binding regulator (PDB code 3NZE). The structure was refined to a resolution of 1.6 Å (Table 1). The centred orthorhombic crystal contained 49% of solvent and one protein molecule per asymmetric unit (AU), from which residues 58–311 could be modelled into the electron density map. Four terminal residues (56, 57, 312, 313) were omitted from the final crystallographic model. Non-protein electron density in some regions of the structure was modelled as 264 water molecules and six cations (Co^{2+}, Cd^{2+}, Mg^{2+} and three Ni^{2+}). The cations originated from crystallization solutions (the crystallization droplets contained 1.3 mM $CoCl_2$, 1.3 mM $CdCl_2$, 1.3 mM $MgCl_2$ and 1.3 mM $NiCl_2$) and are not known to be important for protein function. Three Ni^{2+} ions bind to three histidine residues (His103, His288 and His304). The remaining three ions bind at interfaces with symmetrically related molecules distant from the effector-binding site and their binding most probably represents a crystallization artefact: Co^{2+} is coordinated by Asp226 and by residues His78 and Tyr97 from the symmetrically related molecule, Mg^{2+} is coordinated by Glu93 and symmetrically related His92, and Cd^{2+} is coordinated by Glu189 and His191 and symmetrically related His146.

The structure of C-DeoR in free form was solved by molecular replacement using the previously determined structure of the C-DeoR-effector complex and refined to 1.8 Å resolution (Table 1). The primitive trigonal crystal contained 58% of solvent and two protein molecules per AU. In both molecules, only residues 59–312 could be modelled into the electron density map, and four terminal residues (56, 57, 58, 313) were omitted from the final crystallographic model. The two molecules in the AU represent the biologically active dimer. The RMSD for the superposition of the 254 Cα atoms of the two protein chains in the AU is 0.090, a typical value for different crystal structures of identical proteins [4]. Non-protein electron density within the hydrogen bonding radius was modelled as 225 water molecules and two bicine molecules that originated from crystallization solutions.

The C-DeoR structure comprises a central NAD-binding double Rossmann fold core [5] composed of six parallel β-sheets (β2, β3, β4, β5, β8, β9) flanked by a total of five helices (α3, α4, α6, α10, α11) on both

Table 1. Crystal data and diffraction data collection and refinement statistics. Values in parentheses refer to the highest resolution shell. ADP, atomic displacement parameter. $R_{merge} = 100\sum_{hkl}\sum_i|I_i(hkl) - \langle I(hkl)\rangle|/\sum_{hkl}\sum_i I_i(hkl)$, where $I_i(hkl)$ is an individual intensity of the ith observation of reflection hkl and $\langle I(hkl)\rangle$ is the average intensity of reflection hkl with summation over all data. $R = ||F_o| - |F_c||/|F_o|$, where F_o and F_c are the observed and calculated structure factors, respectively. R_{free} is equivalent to R but is calculated for 5% of the reflections randomly chosen and omitted from the refinement process [6]. Diffraction data for the effector-bound C-DeoR were published previously [8].

	Effector-bound	Free
Data collection statistics		
Wavelength (Å)	0.918	0.918
Space group	$C222_1$	$P3_2$
Unit-cell parameters (Å; °)	76.9, 78.9, 91.4 90, 90, 90	63.1, 63.1, 150.1 90, 90, 120
No. of molecules in AU	1	2
Resolution range (Å)	50–1.60 (1.66–1.60)	50–1.80 (1.86–1.80)
Number of unique reflections	34 660 (2284)	57 887 (3293)
Multiplicity	5.6 (3.3)	3.8 (2.6)
Completeness (%)	93.5 (62.3)	93.1 (53.3)
R_{merge} (%)	4.0 (25.5)	4.8 (17.9)
Average $I/\sigma(I)$	42.8 (2.8)	72.6 (2.9)
Wilson B (Å^2)	18.6	28.6
Refinement statistics		
Resolution range (Å)	19.77–1.60 (1.64–1.60)	27.31–1.80 (1.84–1.80)
No. of reflections in working set	32 880	54 842
No. of reflections in test set	1750 (74)	2921 (110)
R (%)	15.44 (23.7)	19.28 (31.9)
R_{free} (%)	19.05 (28.6)	22.76 (34.4)
RMSD bond lengths (Å)	0.012	0.012
RMSD angles (°)	1.488	1.439
No. of atoms in AU	2385	4259
No. of water molecules in AU	264	225
Mean ADP value, protein/solvent/ligand (Å^2)	23.4/33.5/17.0	52.9/45.9/–
Residues in Ramachandran plot favoured regions[a] (%)	98.9	98.8
Residues in Ramachandran plot allowed regions[a] (%)	100	100
PDB code	4OQP	4OQQ

[a] As determined by MOLPROBITY [7].

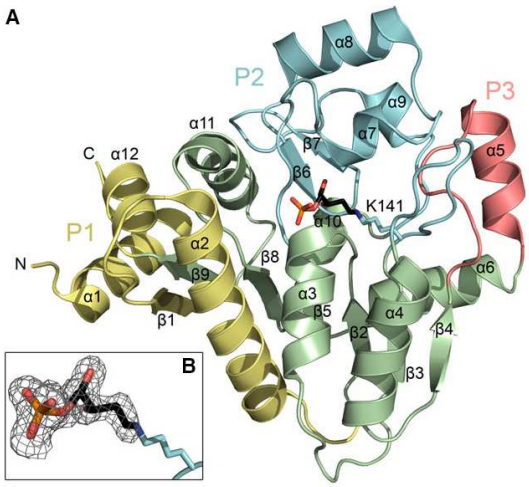

Fig. 1. Overall structure of effector-bound C-DeoR. (A) Cartoon representation of the C-DeoR structure coloured according to the subdomain architecture; the central double Rossmann fold core is shown in green, peripheral subdomain P1 in yellow, peripheral subdomain P2 in cyan and peripheral subdomain P3 in red. The dR5P Schiff base adduct is shown in stick representation with carbon atoms in black; nitrogen, oxygen and phosphorus atoms are coloured blue, red and orange, respectively. Secondary structure elements, Lys141 (K141) and the N- and C-termini are labelled. (B) A detailed view of the effector-binding site is shown with the $F_o - F_c$ electron density map contoured at 2.5σ, which was used to model the ligand.

sides (Fig. 1A). This α/β topology is further complemented by three additional, mostly helical, peripheral subdomains: (a) peripheral subdomain P1 (residues 58–109 and 303–311; α1, β1, α2, α12); (b) peripheral subdomain P2 (residues 141–151 and 208–262; α7, α8, β6, β7, α9); and (c) peripheral subdomain P3 (residues 171–189; α5). The effector-binding site is located at the interface between peripheral subdomains P1 and P2 and the central double Rossmann fold subdomain. In the effector-bound form of C-DeoR, the effector-binding site is occupied by dR5P, which forms a covalent Schiff base adduct with Lys141 (Fig. 1B).

A structure similarity search of the Protein Data Bank performed with the program DALI [9] identified numerous structural homologues among bacterial transcriptional regulators, especially those from the SorC family. The closest sequence and structural homologue of C-DeoR is the putative sugar-binding transcriptional regulator from *Arthrobacter aurescens* TC1 (PDB code 3NZE, sequence identity of 28% for 256 residues), which was used as a model for molecular replacement to solve the effector-bound C-DeoR structure. Superposition of the structure of this putative sugar-binding transcriptional regulator with the C-DeoR structures provides RMSD values of 1.9 and 2.2 Å for effector-bound and free C-DeoR, respectively. C-DeoR also exhibits high structural homology with the central glycolytic gene regulator from *B. subtilis* (CggR) (PDB code 3BXF, sequence identity of 22% for 245 residues), which has been well

characterized in terms of effector binding and oligomerization [10]. Superposition of the CggR structure with the C-DeoR structures provides RMSD values of 2.6 and 2.7 Å for effector-bound and free C-DeoR, respectively. The two proteins are similar in the area of the double Rossmann fold core but differ in their peripheral subdomains. Nevertheless, the position of the effector-binding site and binding orientation of the ligand in this site are very similar (Fig. 2A).

In addition to transcriptional regulators, we identified as structural homologues of C-DeoR many bacterial enzymes involved in sugar metabolism, such as 6-phosphogluconolactonase, glucose-6-phosphate-1-dehydrogenase and glucosamine-6-phosphate deaminase. This is an example of one common protein fold performing distinct enzymatic and regulatory functions. Interestingly, ribose-5-phosphate isomerase A from *Burkholderia thailandensis* (PDB code 3UW1) binds the linear form of ribose-5-phosphate in a position very similar to that of dR5P in C-DeoR (Fig. 2B) [11]. The sugar, however, does not form a covalent adduct in this *B. thailandensis* enzyme because the amino acid residue corresponding to Lys141 of C-DeoR is serine. Superposition of the ribose-5-phosphate isomerase structure with the effector-bound C-DeoR structure provides an RMSD value of 3.4 Å, although the sequence identity is only 12%.

The DALI structure similarity search [9] also identified several enzymes that carry pyridoxal phosphate as a prosthetic group bound via a Schiff base linkage with a lysine residue. These enzymes include 5-aminolevulinate synthase (PDB code 2BWN) [12], methionine gamma-lyase (PDB code 3ACZ), carbon-sulfur lyase involved in aluminium resistance (PDB code 3GWP) and L-allo-threonine aldolase (PDB code 2FM1). Superposition of any of these enzymes with the C-DeoR structures resulted in RMSD values of over 3.5 Å.

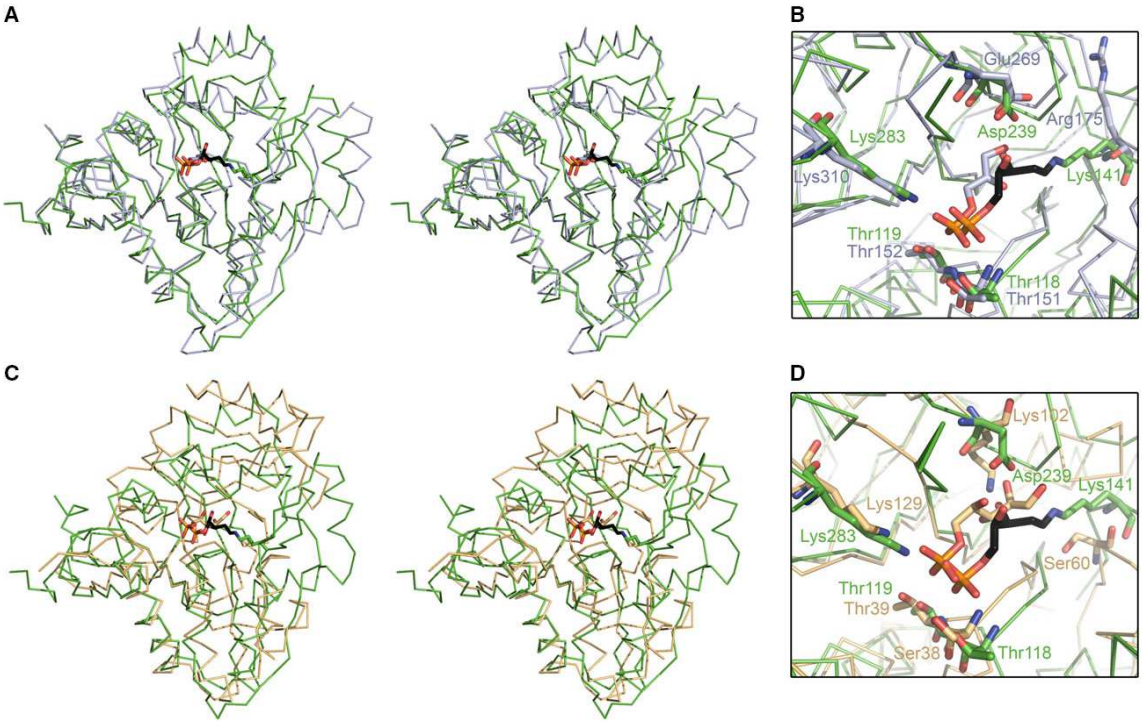

Fig. 2. Superposition of effector-bound C-DeoR with homologous structures. (A) Superposition of C-DeoR (green) with the central glycolytic gene regulator CggR (light blue, PDB code 3BXF) [10] in stereo view. (B) Detail of the ligand binding sites rotated by 50° along the *x*-axis relative to the view in (A). (C) Superposition of C-DeoR (green) with ribose-5-phosphate isomerase A from *B. thailandensis* (gold, PDB code 3UW1) [11] in stereo view. (D) Detail of the ligand binding sites rotated by 50° along the *x*-axis relative to the view in (C). The ligands are shown as sticks with carbon atoms in black (dR5P in C-DeoR), light blue (dihydroxyacetone phosphate in CggR) or gold (ribose-5-phosphate in ribose-5-phosphate isomerase A). Key amino acid residues in the ligand binding sites are highlighted in sticks. Nitrogen, oxygen and phosphorus atoms are coloured blue, red and orange, respectively.

Structural details of effector binding

The effector-binding site of DeoR is formed by residues Trp116, Thr118, Thr119 and Lys283 from the core subdomain, residue Tyr87 from peripheral subdomain P1, and residues Lys141, Thr208, Val209, Gly210, Asp239 and Cys241 from peripheral subdomain P2. The effector molecule dR5P forms a covalent Schiff base linkage with the amino group of Lys141 and is deeply buried in the effector-binding site. A 225.7 Å^2 surface area, which represents 65% of the dR5P total surface area, is involved in the binding interface. All effector hydroxyl groups are engaged in direct hydrogen bond interactions with the protein (Fig. 3A). Specifically, the O3 and O4 atoms of dR5P interact with the side chain of Asp239; the oxygen atoms from the phosphate moiety interact with Thr118, Thr119 and Lys283. The interaction of the phosphate moiety with the N-terminal tip of α3 of the double Rossmann fold (Thr118 and Thr119) is typical for dinucleotide binding Rossmann folds [5,13,14]. In addition, a water molecule (W 501) in the effector-binding site mediates hydrogen bond linkages of O5 and one oxygen atom of the phosphate moiety to amino acid residues Trp116, Thr119 and Met120 (Fig. 3A).

The Schiff base linkage of R5P to Lys141 is schematically shown in Fig. 3B. The imine bond of a Schiff base is generally formed by reaction of an aldehyde with an amine. In the case of C-DeoR, the aldehyde of dR5P reacts with the Lys141 side chain amine. In the C-DeoR crystal structure, the distance between Nζ of Lys141 and dR5P C1 is 1.29 Å, which clearly indicates the presence of a double bond. Schiff bases occur in enzymes carrying pyridoxal phosphate as a prosthetic group [15] and in rhodopsins, in which the retinal group is covalently bound via a Schiff base to a lysine residue [16]. One of these pyridoxal-phosphate-containing enzymes, the putative γ-aminobutyrate aminotransferase GabR from *B. subtilis*, has lost its enzymatic activity and has adapted to function as a transcriptional regulator [17]. The covalent attachment of pyridoxal phosphate to this transcriptional regulator of γ-aminobutyric acid metabolism is crucial for binding of the effector molecule γ-aminobutyric acid [17].

Furthermore, formation of Schiff base intermediates between the substrate and the catalytic lysine residue is a critical step in the catalytic mechanism of some aldolases [18–22] and other lyases, such as porphobilinogen synthase [23] and acetoacetate decarboxylase [24]. Among these enzymes, dR5P aldolase contains dR5P Schiff base adduct with the active site lysine, which represents an intermediate in its catalytic mechanism [25]. The structure of *Escherichia coli* dR5P aldolase, which captures the dR5P Schiff base complex with Lys201, has been solved at atomic resolution (PDB code 1JCJ) [25] and represents the only protein-dR5P adduct in the PDB to date. The Nζ–C bond length of 1.29 Å and Nζ–C–C angle of 125.3° are almost identical to the values found in our C-DeoR-dR5P structure (Nζ–C bond length of 1.29 Å and Nζ–C–C angle of 125.2°).

To our knowledge, the crystal structure of the C-DeoR adduct is the first example of a bacterial transcriptional regulator with a covalently bound effector molecule. To exclude the possibility that the covalent

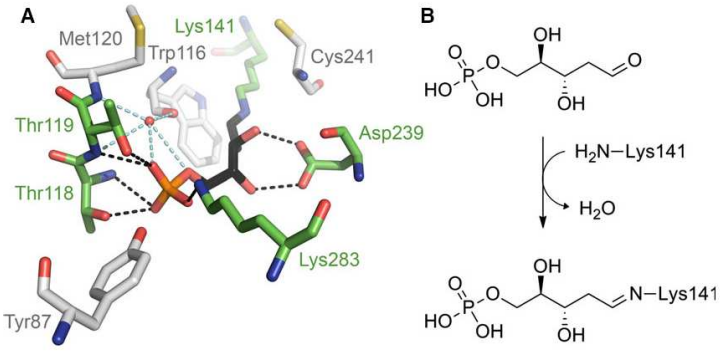

Fig. 3. Binding of dR5P to C-DeoR. (A) The dR5P Schiff base adduct is shown as sticks with carbon atoms in black. The C-DeoR residues in direct hydrogen bonds or a covalent bond (Lys141) with the effector are shown as sticks with green carbon atoms. Other residues within the van der Waals distance (4.2 Å) from the effector are shown as sticks with grey carbon atoms (Thr208, Val209 and Gly210 are not shown for clarity). Direct hydrogen bonds are indicated by black dotted lines; water-mediated hydrogen bonds are indicated by blue dotted lines. (B) Scheme of the formation of the covalent adduct of dR5P on Lys141.

attachment of the effector molecule to Lys141 was a crystallization artefact, we performed mutational analysis and explored Schiff base adduct formation in solution.

Mutational analysis

To evaluate the role of Lys141 in dR5P binding, we prepared four C-DeoR variants mutated at position 141 and tested them for effector binding. Specifically, we assayed dR5P binding to K141N, K141Q, K141R and K141A C-DeoR variants using differential scanning fluorimetry (DSF), also known as Thermofluor [26–28]. Ligand binding restrains the overall protein structure, resulting in higher stability. Thermal stabilization of a protein upon addition of ligand can therefore be used as a qualitative measure of effector binding which can give us a hint for effector affinity. The thermal unfolding transitions of wild-type and mutant C-DeoR variants were monitored by the fluorescence of SYPRO® Orange dye, and the melting temperature values (T_m) were estimated for increasing concentrations of dR5P (Fig. 4). Addition of the dR5P effector molecule significantly increased the T_m of wild-type C-DeoR (increase of ~9 °C), while the addition of dR1P did not stabilize the protein and even caused destabilization at high concentrations. We thus did not confirm dR1P binding to C-DeoR, although this sugar has been shown to induce expression of the *dra-nupC-pdp* operon [2]. Thermal stabilization of the C-DeoR mutants upon addition of dR5P was lower than that of wild-type which suggested that mutation of Lys141 significantly lowers or even disrupts the protein's affinity toward the effector molecule. We can

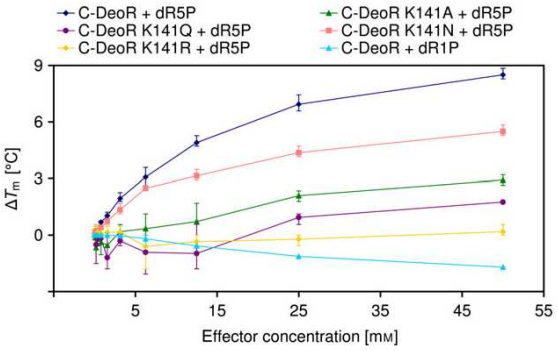

Fig. 4. Thermal stabilization of C-DeoR and C-DeoR mutant variants in the presence of deoxyribose-5-phosphate (dR5P) and deoxyribose-1-phosphate (dR1P). The T_m values were determined by DSF.

therefore conclude that Lys141, which provides the free amino group for formation of a Schiff base with the carbonyl group of dR5P, is crucial for effector binding.

Formation of C-DeoR-dR5P Schiff base adduct in solution

We followed the formation of a covalent Schiff base adduct between dR5P and C-DeoR in solution at low protein and effector concentrations using mass spectrometry (Fig. 5A). The Schiff base product was identified by MALDI-TOF in C-DeoR incubated with 1.8 mM dR5P, which is close to the upper concentration limit of this metabolite in *B. subtilis* [29]. Free C-DeoR was detected as a peak corresponding to m/z 29 335, while the reduced Schiff base C-DeoR adduct was detected at m/z 29 533. Time-dependent increase in the abundance of the higher molecular mass peak was observed (Fig. 5A). The difference in m/z values of 198 corresponds to the molecular mass of the dR5P residue upon Schiff base formation and subsequent reduction to 3,4-dihydroxy-5-(phosphonooxy)pentyl ($C_5H_{11}O_6P$). Incubation of K141N C-DeoR with 1.8 mM dR5P did not result in adduct formation, even after 16 h (Fig. 5B).

This mass spectrometry analysis confirmed that C-DeoR-dR5P Schiff base adducts formed in solution and were not merely crystallization artefacts. Furthermore, we confirmed that the presence of Lys141 is crucial for covalent binding of the effector to C-DeoR.

Effect of ligand binding on the structure and oligomerization of C-DeoR

To understand on a structural level how the effector molecule modulates DeoR function, we followed changes in C-DeoR structure upon effector binding. Superposition of the 237 Cα atoms of the effector-bound and free C-DeoR structures provides an RMSD value of 1.15 Å. The binding of dR5P induces major structural changes in the vicinity of the effector-binding site, mostly in peripheral subdomains P2 and P3. In contrast, the core double Rossmann fold and peripheral subdomain P1 structures remain almost unaffected (Fig. 6A). Major changes (with RMSD for main chain atoms over 1.8 Å) occur mainly in peripheral subdomain P2, specifically in helices α7 and α8 and residues 141–151, which form a loop connecting β3 and α4 (Fig. 6A). Structural changes in this loop region have been shown to be important for effector binding to the repressor CggR from *B. subtilis* [10]. While the loop region in CggR (residues 174–184)

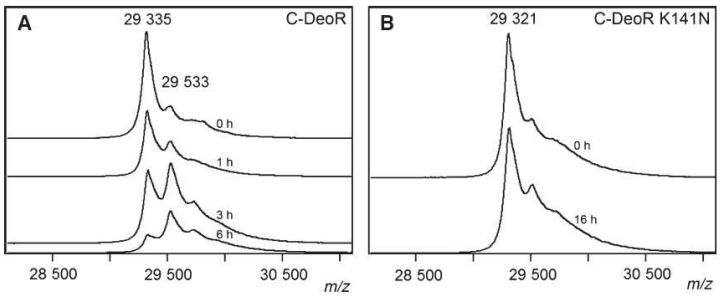

Fig. 5. Schiff base covalent adduct of dR5P with C-DeoR in solution. MALDI-TOF spectra of C-DeoR zoomed into the singly charged protein ion region are shown for wild-type C-DeoR (A) and K141N C-DeoR mutant (B). Incubation time (h) with dR5P is indicated for each spectrum. The *m*/*z* values for native wild-type C-DeoR (*m*/*z* 29 335), the reduced Schiff base adduct of wild-type C-DeoR (*m*/*z* 29 533) and native K141N mutant (*m*/*z* 29 321) are indicated. The small satellite peaks at higher *m*/*z* next to the main peaks are present in all the spectra independent of incubation with dR5P and most probably reflect some other type of protein modification unrelated to the Schiff base adduct. In the wild-type C-DeoR, the position of the satellite peak is almost identical to the position of the peak for covalently modified C-DeoR.

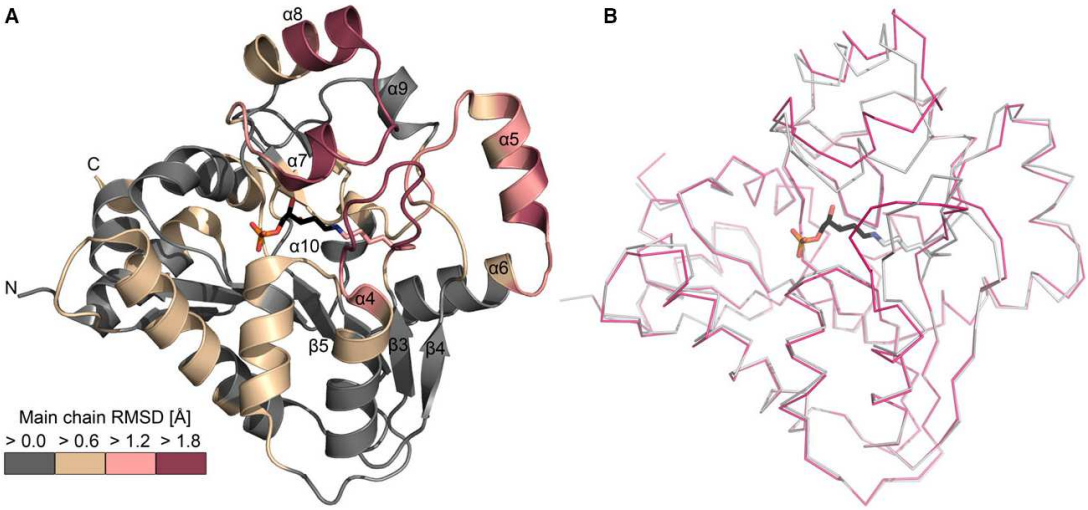

Fig. 6. Effector-induced structural changes in C-DeoR. (A) The extent of the structural changes in C-DeoR induced by effector binding is shown. Cartoon representation of the effector-bound C-DeoR structure is coloured according to increasing main chain RMSD for superposition of the free and effector-bound C-DeoR structures. The dR5P Schiff base adduct is shown as sticks with carbon atoms in black. N- and C-termini and the secondary structure elements discussed in the text are labelled. (B) Superposition of effector-bound C-DeoR (grey) with free C-DeoR (magenta).

undergoes a major structural change and acts as a flap that closes over the effector-binding site, the changes in C-DeoR are more subtle.

Upon attachment of dR5P to Lys141, which is located at the base of the loop, the downstream residues rearrange so that the tip of the loop extends toward the helical region of the P2 subdomain. The structural changes in the P2 subdomain can be qualitatively described as the grasp of an index finger (helical region) and thumb (loop region) around the effector-binding site (Fig. 6B). Helices α7 and α8 move toward the centre of the effector-binding site, and residues 220–223 in the region connecting α7 and α8 come into contact with the tip of the loop region (residues 146–149). This primary structural change induced by effector binding further propagates to peripheral subdomain P3 through residues 173–179, which are adjacent to the 141–151 loop region and to α5 (Fig. 6A).

Helix α5 and the 141–151 loop are involved in the dimeric interface, and we therefore investigated the effects of structural changes induced by effector binding on the protein's oligomeric state.

We analysed the oligomeric state of both C-DeoR and full-length DeoR in solution by analytical size-exclusion chromatography. The apparent molecular weight of C-DeoR as well as that of the full-length DeoR protein were estimated in the presence or absence of the effector molecule dR5P. These experiments revealed that C-DeoR forms dimers in solution which persist in the presence of dR5P. Full-length DeoR forms tetramers in solution and this oligomeric assembly is also observed in the presence of dR5P (Fig. 7). These results were corroborated by dynamic light scattering experiments which showed no change in particle size distribution upon addition of 50 mM dR5P to 750 μM C-DeoR and 120 μM full-length DeoR proteins, respectively (data not shown). Our results suggest that two distinct interfaces involved in oligomerization exist in the DeoR: the first one is formed by the C-terminal domains and the second one by the DNA-binding domains.

In an attempt to identify and characterize the interfaces mediating interaction of two C-DeoR, we performed a detailed analysis of the intermolecular contacts observed in both the free and effector-bound C-DeoR crystal structures. The crystal interfaces and the stability of potential assemblies were evaluated using methods available through the Protein Interfaces, Surfaces and Assemblies (PISA) server [30]. In the free C-DeoR structure, we identified a major interface of 1367.3 Å^2, which results in formation of a stable dimeric assembly of the two molecules present in the AU. The interface area represents approximately 12% of the total solvent-accessible surface area of each monomer, comprising 40 interacting residues from each chain (Fig. 8, Table 2). In the effector-bound C-DeoR structure, the interface area decreased to 841.3 Å^2, which represents approximately 7% of the total solvent-accessible surface area of each monomer and comprises 25 interacting residues from each chain (Fig. 8, Table 2). Dimeric assemblies of both the free and effector-bound C-DeoR were classified as stable based on the value of the free energy of dissociation of a potential assembly calculated by the PISA server [30]. The dimer of free C-DeoR is tightly packed and gets looser upon effector binding as documented by the distance between the two N-termini changing from 78 to 84 Å (Fig. 8A,C).

The interfacing residues are located in peripheral subdomain P3 in α5 and its connecting loop (comprising residues 170–179) and in peripheral subdomain P2, specifically in the 141–151 loop and in the region connecting α7 and α8 (residues 221–224). Another part of the interface area is located in the region of the central double Rossmann fold core adjacent to the P2 subdomain, specifically β3, α4, β4, α6, and the region connecting α4 and β4. The structural changes upon effector binding result in an overall loss of contact, which is most pronounced in the 141–151 loop and in the central double Rossmann fold core α4 (Table 2).

The dimeric assembly in C-DeoR crystal structures is similar to dimers observed for other effector-binding domains of the SorC/DeoR family, such as CggR from *B. subtilis* [10], putative sugar-binding transcriptional regulator from *A. aurescens* TC1 (PDB code 3NZE) and sorbitol operon regulator SorC from *Klebsiella pneumoniae* (PDB code 2W48) [31]. The crystal structure of SorC also revealed a tetrameric assembly

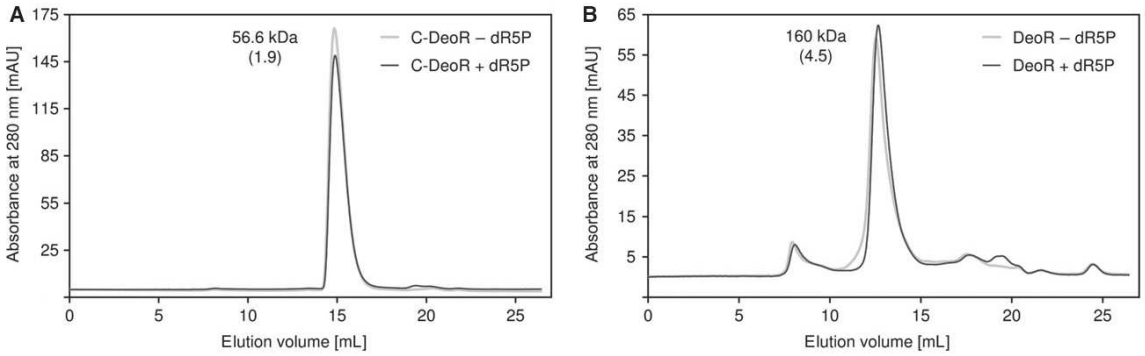

Fig. 7. C-DeoR oligomerization in solution. Elution profiles from size-exclusion chromatography of C-DeoR (A) and full-length DeoR (B) in the absence (grey) and presence (black) of dR5P are shown. The apparent molecular weights are indicated together with the ratio between the apparent molecular weights and the theoretical molecular weights of monomers (in parentheses).

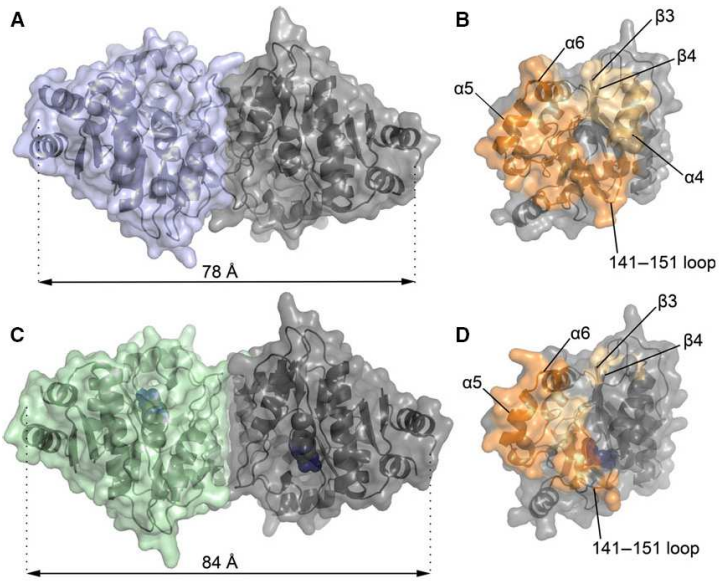

Fig. 8. Dimeric interface in C-DeoR crystal structures. (A) Cartoon surface representation of dimeric assembly for free C-DeoR. (B) Surface representation of the dimeric interface of free C-DeoR. Amino acid residues involved in the dimeric interface are shown in orange; interfacing residues with main chain RMSD over 1.2 Å for the superposition of free and effector-bound C-DeoR are highlighted in a darker orange colour. (C) Cartoon surface representation of dimeric assembly for effector-bound C-DeoR dimer. The dR5P molecules are shown as blue spheres. (D) Surface representation of the dimeric interface of dR5P-bound C-DeoR. The colour scheme is the same as in (B). The distances between the two N-termini in the dimer are indicated in (A) and (C). The views in (B) and (D) are the same, depicting C-DeoR monomers rotated by 90° relative to the views in (A) and (C), respectively. The secondary structure elements involved in the interface are labelled in (B) and (D).

formed by the full-length protein (Fig. 9A) which helped us to deduce the positions of N-terminal DNA-binding domains in DeoR, to understand DeoR oligomerization and to propose a model for modulation of DeoR function (Fig. 9B,C). DeoR was shown to bind DNA operator, which contains a palindromic binding sequence, as a tetramer or possibly cooperatively as two dimers [2,3]. In our model, the tetramer of DeoR with high affinity toward DNA is assembled through two distinct interfaces and can be regarded as a dimer of dimers (Fig. 9B). The first interface is mediated by a domain swap of the DNA-binding domains (similarly to the structure of SorC, Fig. 9A) while the second interface is formed by tightly packed effector-binding domains (interfaces observed in our crystal structures, Fig. 8). Upon effector binding, the interface between the two effector-binding domains loosens and results in a change in relative orientation of the N-terminal DNA-binding domains within the dimer (Fig. 9C). The tetrameric assembly is not disrupted but has a lower affinity toward the DNA and might be more easily displaced from the promoter region by RNA polymerase during transcription initiation.

This model is in agreement with our observation that the DeoR oligomeric state is not affected by dR5P (Fig. 7). The change in relative distance between the two N-termini in C-DeoR observed for the dimer in free and effector-bound form (Fig. 8A,C) gives us a hint of understanding about how the structural change upon effector binding is transmitted into the DNA-binding domains. The exact structural mechanism, however, has yet to be unravelled. Determining a crystal structure of full-length DeoR or DeoR-DNA operator complex may provide further insight.

Materials and methods

Protein expression and purification

Wild-type and mutant C-DeoR and full-length DeoR proteins were expressed in *E. coli* BL21(DE3) and purified as previously described [8,32]. Briefly, His-tagged proteins were subjected to nickel-chelation chromatography followed by His-tag cleavage with tobacco etch virus protease, a second nickel-chelation chromatography step, and dialysis against protein storage buffer optimized for crystallization

Table 2. Residues involved in the C-DeoR dimer interface. Amino acid residues with buried surface area (BSA) > 10% are listed; residues with main chain RMSD over 1.2 Å for the superposition of free C-DeoR with effector-bound C-DeoR are highlighted in bold. BSA was determined by the PISA server [30].

Residue	Location	C-DeoR BSA (%)	C-DeoR-dR5P BSA (%)
GLU 136	β3	19.6	0.9
GLY 143	141–151 loop	20.7	0
ILE 144	141–151 loop	72.0	59.5
SER 145	141–151 loop	81.2	20.4
HIS 146	141–151 loop	79.5	75.1
SER 147	141–151 loop	45.7	0
ARG 148	141–151 loop	19.9	52.6
ASN 150	141–151 loop	66.3	0
THR 151	141–151 loop	15.0	0
ALA 154	α4	57.2	0
GLU 155	α4	45.1	0
GLN 158	α4	66.6	0
THR 166	α4–β4	51.0	4.4
MET 167	β4	72.9	31.1
PRO 168	β4	76.3	27.0
ARG 169	β4	45.4	34.3
TYR 170	β4	46.8	0
PRO 172	β4–α5	84.0	68.9
LEU 173	β4–α5	95.7	26.9
PRO 174	β4–α5	92.1	28.7
VAL 176	β4–α5	77.2	0
PHE 177	β4–α5	100.0	5.6
ASP 178	β4–α5	58.9	39.2
ASN 179	β4–α5	1.4	22.1
ASP 181	α5	1.7	18.2
VAL 182	α5	88.1	88.4
MET 185	α5	55.1	72.3
VAL 186	α5	100.0	65.6
ASP 189	α5–α6	87.8	70.2
ARG 190	α6	30.1	2.1
HIS 191	α6	82.0	61.4
ILE 192	α6	91.2	83.6
ILE 195	α6	50.2	0
GLY 222	α7–α8	35.7	42.8
TYR 223	α7–α8	76.8	0

(20 mM tri-sodium citrate, pH 7.0–7.5, 150 mM NaCl, 0.02% (v/v) β-mercaptoethanol). The full-length DeoR protein was treated with benzonase prior to purification (25 U per 1 mL of low salt bacterial lyzate; 1 h at 25 °C; 2 mM $MgCl_2$).

For mutagenesis of Lys141, a 928 bp *Xba*I-*Sac*I subfragment was first cloned into pUC18 vector. K141A, K141R, K141N and K141Q mutations were introduced according to the QuikChange Site-Directed Mutagenesis Protocol (Stratagene, La Jolla, CA, USA) using the following pairs of mutagenic primers: K141**A**, 5′-GGTCGTCCAGCTG**GC**CGGCGGCATCAGCC, 5′-GGCTGATGCCGCCGGCCAGCTGGACGACC; K141**R**, 5′-GGTCGTCCAGCTG**CGC**GGCGGCATCAGCC, 5′-GGCTGATGCCGCCGCGCAGCTGGACGACC; K141Q, 5′-GGTCGTCCAGCTG**CAG**GGCGGCATCAGCC, 5′-GGCTGATGCCGCCCTGCAGCTGGACGACC; and K141N, 5′-GGTCGTCCAGCTG**AAC**GGCGCATCAGCC, 5′-GGCTGATGCCGCCGTTCAGCTGGACGACC. After sequence verification, the *Xba*I-*Sac*I fragments carrying the respective mutations were used to replace the wild-type fragment in the pET-151 expression plasmid.

Protein crystallization and diffraction data collection

Crystallization of C-DeoR in complex with dR5P and collection of the diffraction data have been published elsewhere [8]. Crystals of free C-DeoR were obtained at 18 °C using the hanging-drop vapour diffusion technique in VDX48 plates (Hampton Research, Aliso Viejo, CA, USA) with a reservoir solution (200 μL) of 0.08 M bicine, pH 8.5, 16% (w/v) PEG 6000. Droplets were prepared by mixing 0.5 μL of 22 $mg{\cdot}mL^{-1}$ C-DeoR stored in buffer containing 20 mM tri-sodium citrate, pH 7.0, 150 mM NaCl, 0.02% (v/v) β-mercaptoethanol with 1 μL of reservoir solution. Crystals were quick-soaked (45 s) in mother liquor supplemented with 10% (v/v) glycerol and flash-cooled in liquid nitrogen using nylon mounting loops (Hampton Research). A complete data set at 1.80 Å resolution was collected at −173 °C at beamline MX14.2 of the Berlin Electron Storage Ring Society for Synchrotron Radiation (BESSY), Germany [33]. The data set was processed using the HKL-3000 package [34]. The crystal parameters and data collection statistics are listed in Table 1. The low value of the completeness in the highest resolution shell is due to anisotropic diffraction of the crystals.

Structure determination and analysis

The structure of C-DeoR was determined by molecular replacement with the program MOLREP [35] using the structure of the effector-binding domain of the putative sugar-binding transcriptional regulator from *A. aurescens* TC1 (PDB code 3NZE, residues 5–263) as a search model. Model refinement was performed using the program REFMAC 5.7.0032 [36] from the CCP4 package [37] in combination with manual adjustments in COOT software [38]. In the final stages, translation, libration, screw (TLS) refinement was included [39] using 20 TLS groups for effector-bound C-DeoR and 10 TLS groups for each chain in the free C-DeoR dimer. The ligand was modelled after complete refinement of the C-DeoR and solvent model. MOLPROBITY server [7] was used for evaluation of the final model quality. The final refinement statistics are summarized in Table 1. The structures were analysed using the servers PISA [30] and DALI [9] and the programs LSQKAB (superpose) [40], BAVERAGE and CONTACT from the CCP4 package [37]. All the

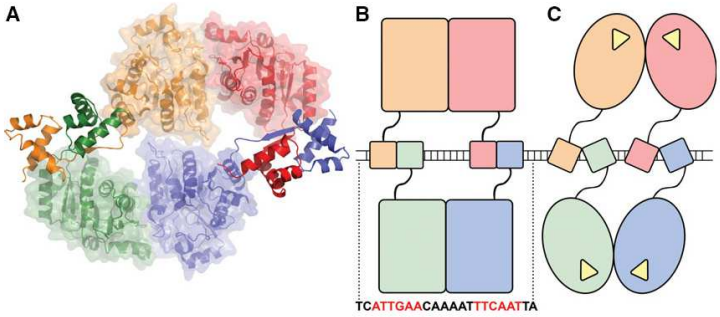

Fig. 9. Schematic model of DeoR function. (A) Tetrameric assembly of SorC from *K. pneumoniae* (PDB code 2W48) [31] is shown as a cartoon with differently coloured chains. Effector-binding domains (residues 60–314) are also represented as transparent surfaces. (B) Free DeoR tight tetramer bound to the DNA operator sequence; the palindrome is highlighted in red in the operator sequence. (C) Effector-bound less-tight DeoR tetramer loosely bound to the DNA operator sequence. dR5P is shown as yellow triangles. The colour coding in (B) and (C) is the same as in (A).

figures representing structures were created using PYMOL [41]. Atomic coordinates and structure factors for the crystal structures of free C-DeoR and the covalent Schiff base complex of C-DeoR with dR5P were deposited in the PDB with accession codes 4OQQ and 4OQP, respectively.

Differential scanning fluorimetry

Ligand titration was performed in 20 mM tri-sodium citrate, pH 7.5, 150 mM NaCl, 0.02% (v/v) β-mercaptoethanol as previously described [32]. A temperature gradient from 20 to 95 °C was applied at a rate of 0.83 °C·min^{-1} [8]. The concentration of wild-type C-DeoR and C-DeoR mutants (K141A, K141R, K141N and K141Q) was 1 μM; dR5P or dR1P concentrations ranged from 0.1 to 50 mM. Three parallel measurements were performed for each ligand concentration, and the T_m values were averaged.

Mass spectrometry

The formation of the covalent Schiff base adduct was analysed by UltrafleXtreme™ MALDI-TOF/TOF (Bruker Daltonics, Billerica, MA, USA). Wild-type or K141N C-DeoR (1 μM) was incubated with 1.8 mM dR5P in 20 mM tri-sodium citrate, pH 7.5, 150 mM NaCl, 0.02% (v/v) β-mercaptoethanol for 1, 3, 6 and 16 h at 25 °C in the presence of 50 mM $NaBH_3CN$, which reduced – and thus stabilized – the Schiff base product, a method widely used to study protein glycation [42]. Schiff base formation was terminated by addition of 50 mM hydroxylamine. The samples were desalted prior to mass spectrometry analysis on centrifugal Amicon Ultracel 10K filters (Merck Millipore, Billerica, MA, USA) by washing with deionized water. Protein sample (1 μL) was mixed with 1 μL of a saturated solution of sinapinic acid (Sigma-Aldrich, Saint Louis, MO, USA) in 30% (v/v) acetonitrile, 0.1% (v/v) trifluoroacetic acid and spotted on a MALDI target. The spectra were acquired in linear mode in the 5–35 kDa range. Calibration was performed with a protein standard mixture.

Size-exclusion chromatography

Analytical size-exclusion chromatography of both C-DeoR and full-length DeoR was performed in 20 mM tri-sodium citrate, pH 7.5, 150 mM NaCl, 0.02% (v/v) β-mercaptoethanol using an Äkta Basic FPLC system with a Superdex 200 10/300 GL Tricorn column (Amersham Biosciences, Little Chalfont, UK) at a flow rate of 0.5 mL·min^{-1}. The molecular weight calibration standards (Sigma-Aldrich) contained blue dextran (2000 kDa), bovine serum albumin (66 kDa), carbonic anhydrase (29 kDa), cytochrome *c* (12.4 kDa) and aprotinin (6.5 kDa). In the case of full-length DeoR, standards of higher molecular weights were used (Sigma-Aldrich): blue dextran (2000 kDa), bovine thyroglobulin (669 kDa), horse spleen apoferritin (443 kDa), sweet potato β-amylase (200 kDa), yeast alcohol dehydrogenase (150 kDa), bovine serum albumin (66 kDa) and carbonic anhydrase (29 kDa).

Acknowledgements

The authors wish to thank the following colleagues from the Institute of Organic Chemistry and Biochemistry AS CR in Prague: Jiří Brynda, Petr Pachl and Evžen Bouřa for their help with diffraction data collection, and Jitka Kredbova for her technical assistance with protein preparation. This work was supported by the Ministry of Education of the Czech Republic (project ME08016) and in part by research projects RVO 68378050 and 61388963 awarded by the Academy of Sciences of the Czech Republic. The use of MX14.2

operated by the Helmholtz-Zentrum Berlin at the BESSY II electron storage ring (Berlin-Adlershof, Germany) to collect diffraction data is acknowledged. JS is a student supported in part by the Faculty of Science, Charles University in Prague.

Author contributions

JS planned experiments, performed experiments, analysed data and wrote the paper; MF performed experiments; MH performed experiments and analysed data; ZO analysed data; PR planned experiments, analysed data and wrote the paper.

References

1 Saxild HH, Andersen LN & Hammer K (1996) DranupC-pdp operon of *Bacillus subtilis*: nucleotide sequence, induction by deoxyribonucleosides, and transcriptional regulation by the deoR-encoded DeoR repressor protein. *J Bacteriol* **178**, 424–434.

2 Zeng X & Saxild HH (1999) Identification and characterization of a DeoR-specific operator sequence essential for induction of dra-nupC-pdp operon expression in *Bacillus subtilis*. *J Bacteriol* **181**, 1719–1727.

3 Zeng X, Saxild HH & Switzer RL (2000) Purification and characterization of the DeoR repressor of *Bacillus subtilis*. *J Bacteriol* **182**, 1916–1922.

4 Betts MJ & Sternberg MJ (1999) An analysis of conformational changes on protein–protein association: implications for predictive docking. *Protein Eng* **12**, 271–283.

5 Dym O & Eisenberg D (2001) Sequence-structure analysis of FAD-containing proteins. *Protein Sci* **10**, 1712–1728.

6 Brunger AT (1992) Free R value: a novel statistical quantity for assessing the accuracy of crystal structures. *Nature* **355**, 472–475.

7 Lovell SC, Davis IW, Arendall WB III, de Bakker PI, Word JM, Prisant MG, Richardson JS & Richardson DC (2003) Structure validation by Calpha geometry: phi, psi and Cbeta deviation. *Proteins* **50**, 437–450.

8 Pisackova J, Prochazkova K, Fabry M & Rezacova P (2013) Crystallization of the effector-binding domain of repressor DeoR from *Bacillus subtilis*. *Cryst Growth Des* **13**, 844–848.

9 Holm L & Rosenstrom P (2010) Dali server: conservation mapping in 3D. *Nucleic Acids Res* **38**, W545–W549.

10 Rezacova P, Kozisek M, Moy SF, Sieglova I, Joachimiak A, Machius M & Otwinowski Z (2008) Crystal structures of the effector-binding domain of repressor central glycolytic gene regulator from *Bacillus subtilis* reveal ligand-induced structural changes upon binding of several glycolytic intermediates. *Mol Microbiol* **69**, 895–910.

11 Baugh L, Gallagher LA, Patrapuvich R, Clifton MC, Gardberg AS, Edwards TE, Armour B, Begley DW, Dieterich SH, Dranow DM *et al.* (2013) Combining functional and structural genomics to sample the essential Burkholderia structome. *PLoS One* **8**, e53851.

12 Astner I, Schulze JO, van den Heuvel J, Jahn D, Schubert WD & Heinz DW (2005) Crystal structure of 5-aminolevulinate synthase, the first enzyme of heme biosynthesis, and its link to XLSA in humans. *EMBO J* **24**, 3166–3177.

13 Bellamacina CR (1996) The nicotinamide dinucleotide binding motif: a comparison of nucleotide binding proteins. *FASEB J* **10**, 1257–1269.

14 Wierenga RK, Demaeyer MCH & Hol WGJ (1985) Interaction of pyrophosphate moieties with alpha-helixes in dinucleotide binding-proteins. *Biochemistry* **24**, 1346–1357.

15 John RA (1995) Pyridoxal phosphate-dependent enzymes. *Biochim Biophys Acta* **1248**, 81–96.

16 Palczewski K (2006) G protein-coupled receptor rhodopsin. *Annu Rev Biochem* **75**, 743–767.

17 Edayathumangalam R, Wu R, Garcia R, Wang Y, Wang W, Kreinbring CA, Bach A, Liao J, Stone TA, Terwilliger TC *et al.* (2013) Crystal structure of *Bacillus subtilis* GabR, an autorepressor and transcriptional activator of gabT. *Proc Natl Acad Sci USA* **110**, 17820–17825.

18 Lehwess-Litzmann A, Neumann P, Parthier C, Ludtke S, Golbik R, Ficner R & Tittmann K (2011) Twisted Schiff base intermediates and substrate locale revise transaldolase mechanism. *Nat Chem Biol* **7**, 678–684.

19 St-Jean M, Lafrance-Vanasse J, Liotard B & Sygusch J (2005) High resolution reaction intermediates of rabbit muscle fructose-1,6-bisphosphate aldolase: substrate cleavage and induced fit. *J Biol Chem* **280**, 27262–27270.

20 Lorentzen E, Siebers B, Hensel R & Pohl E (2005) Mechanism of the Schiff base forming fructose-1,6-bisphosphate aldolase: structural analysis of reaction intermediates. *Biochemistry* **44**, 4222–4229.

21 Allard J, Grochulski P & Sygusch J (2001) Covalent intermediate trapped in 2-keto-3-deoxy-6-phosphogluconate (KDPG) aldolase structure at 1.95-A resolution. *Proc Natl Acad Sci USA* **98**, 3679–3684.

22 Huynh N, Aye A, Li Y, Yu H, Cao H, Tiwari VK, Shin DW, Chen X & Fisher AJ (2013) Structural basis for substrate specificity and mechanism of N-acetyl-D-neuraminic acid lyase from *Pasteurella multocida*. *Biochemistry* **52**, 8570–8579.

23 Erskine PT, Newbold R, Roper J, Coker A, Warren MJ, Shoolingin-Jordan PM, Wood SP & Cooper JB (1999) The Schiff base complex of yeast 5-aminolaevulinic acid

dehydratase with laevulinic acid. *Protein Sci* **8**, 1250–1256.
24 Ho MC, Menetret JF, Tsuruta H & Allen KN (2009) The origin of the electrostatic perturbation in acetoacetate decarboxylase. *Nature* **459**, 393–397.
25 Heine A, DeSantis G, Luz JG, Mitchell M, Wong CH & Wilson IA (2001) Observation of covalent intermediates in an enzyme mechanism at atomic resolution. *Science* **294**, 369–374.
26 Pantoliano MW, Petrella EC, Kwasnoski JD, Lobanov VS, Myslik J, Graf E, Carver T, Asel E, Springer BA, Lane P *et al*. (2001) High-density miniaturized thermal shift assays as a general strategy for drug discovery. *J Biomol Screen* **6**, 429–440.
27 Lo MC, Aulabaugh A, Jin G, Cowling R, Bard J, Malamas M & Ellestad G (2004) Evaluation of fluorescence-based thermal shift assays for hit identification in drug discovery. *Anal Biochem* **332**, 153–159.
28 Ericsson UB, Hallberg BM, Detitta GT, Dekker N & Nordlund P (2006) Thermofluor-based high-throughput stability optimization of proteins for structural studies. *Anal Biochem* **357**, 289–298.
29 Bennett BD, Kimball EH, Gao M, Osterhout R, Van Dien SJ & Rabinowitz JD (2009) Absolute metabolite concentrations and implied enzyme active site occupancy in *Escherichia coli*. *Nat Chem Biol* **5**, 593–599.
30 Krissinel E & Henrick K (2007) Inference of macromolecular assemblies from crystalline state. *J Mol Biol* **372**, 774–797.
31 de Sanctis D, McVey CE, Enguita FJ & Carrondo MA (2009) Crystal structure of the full-length sorbitol operon regulator SorC from *Klebsiella pneumoniae*: structural evidence for a novel transcriptional regulation mechanism. *J Mol Biol* **387**, 759–770.
32 Prochazkova K, Cermakova K, Pachl P, Sieglova I, Fabry M, Otwinowski Z & Rezacova P (2012) Structure of the effector-binding domain of the arabinose repressor AraR from *Bacillus subtilis*. *Acta Crystallogr D Biol Crystallogr* **68**, 176–185.
33 Mueller U, Darowski N, Fuchs MR, Forster R, Hellmig M, Paithankar KS, Puhringer S, Steffien M, Zocher G & Weiss MS (2012) Facilities for macromolecular crystallography at the Helmholtz-Zentrum Berlin. *J Synchrotron Radiat* **19**, 442–449.
34 Minor W, Cymborowski M, Otwinowski Z & Chruszcz M (2006) HKL-3000: the integration of data reduction and structure solution – from diffraction images to an initial model in minutes. *Acta Crystallogr D Biol Crystallogr* **62**, 859–866.
35 Vagin A & Teplyakov A (2000) An approach to multi-copy search in molecular replacement. *Acta Crystallogr D Biol Crystallogr* **56**, 1622–1624.
36 Murshudov GN, Vagin AA & Dodson EJ (1997) Refinement of macromolecular structures by the maximum-likelihood method. *Acta Crystallogr D Biol Crystallogr* **53**, 240–255.
37 Collaborative Computational Project N (1994) The CCP4 suite: programs for protein crystallography. *Acta Crystallogr D Biol Crystallogr* **50**, 760–763.
38 Emsley P & Cowtan K (2004) Coot: model-building tools for molecular graphics. *Acta Crystallogr D Biol Crystallogr* **60**, 2126–2132.
39 Winn MD, Isupov MN & Murshudov GN (2001) Use of TLS parameters to model anisotropic displacements in macromolecular refinement. *Acta Crystallogr D Biol Crystallogr* **57**, 122–133.
40 Krissinel E & Henrick K (2004) Secondary-structure matching (SSM), a new tool for fast protein structure alignment in three dimensions. *Acta Crystallogr D Biol Crystallogr* **60**, 2256–2268.
41 Schrodinger LLC (2010) The PyMOL Molecular Graphics System, Version 1.3r1. Schrodinger LLC, Portland, OR, USA.
42 Farah MA, Bose S, Lee JH, Jung HC & Kim Y (2005) Analysis of glycated insulin by MALDI-TOF mass spectrometry. *Biochim Biophys Acta* **1725**, 269–282.

7.3 Optimization of the crystallizability of a single-chain antibody fragment

Background

Single-chain variable antibody fragments (scFvs) are engineered proteins of major therapeutic and diagnostic potential. Understanding the antigen-binding properties of the antibodies as well as employing various protein-engineering approaches including antibody humanization relies on the knowledge of antibody three-dimensional structure. Majority of scFv fragments tend to spontaneously oligomerize, which impairs their homogeneity, and therefore presents a major obstacle in crystallization. This work presents a new approach to scFv crystallizability optimization, demonstrated on a representative scFv fragment of anti-CD3 antibody MEM-57. The approach employs a Thermofluor-based assay to screen for optimal conditions both for stability and for oligomeric homogeneity of the scFv fragment. In the optimized conditions, scFv MEM-57 exhibited significantly improved ability to yield crystals.

Summary

We constructed a single-chain variable fragment (scFv) of anti-CD3 antibody MEM-57. Pre-crystallization biochemical and biophysical analysis of the purified protein using a combination of size-exclusion chromatography and dynamic light scattering revealed the presence of scFv dimer and higher oligomers and general heterogeneity of the sample, unfavorable for crystallization. Thermofluor assay was used to screen for the conditions optimal not only for protein stability, but also for protein sample oligomeric homogeneity, preferentially stabilizing scFv monomer. The beneficial effect of the optimized protein storage buffer was confirmed by the size-exclusion chromatography and dynamic light scattering data and finally by the results of crystallization screening trials. This approach may resolve the issue of unfavourable oligomerization of scFv fragments in general and result in scFv samples with improved crystallizability. The key results of the publication are summarized in Figure 10.

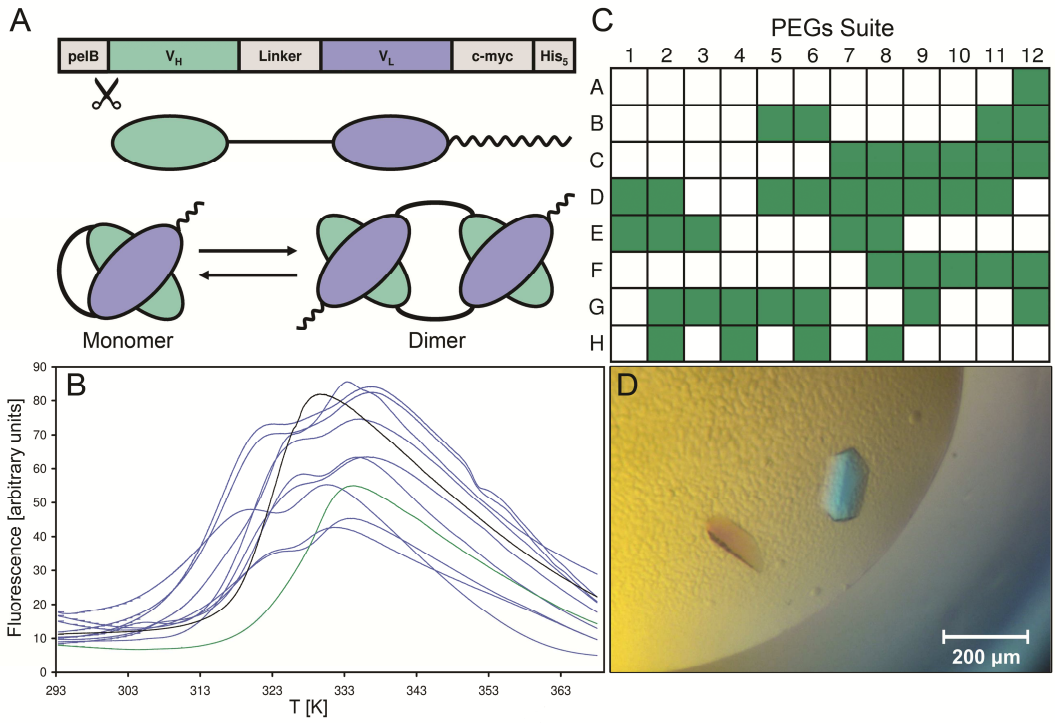

Figure 10: Optimization of crystallizability of scFv MEM-57
A: A schematic of the scFv MEM-57 gene construct and protein product is shown. V_H and V_L are the variable domains of the heavy and light IgG chains, respectively; pelB is a leader sequence targeting recombinant protein to the periplasm, c-myc and His_5 are immunodetection and purification tags, respectively. B: Thermofluor-based protein-unfolding curves for the original (black) and optimized (green) storage buffers are shown along with representative multiple-inflection curves (blue). C: A schematic of the crystallization screening plate containing the PEGs Suite (Qiagen) is shown. Conditions yielding crystals are highlighted in green. D: An example of crystals obtained using 100 mM HEPES pH 7.5, 25% (w/v) PEG 3000 is shown.

My contribution

I expressed and purified recombinant scFv MEM-57, performed all the biochemical and biophysical experiments: size-exclusion chromatography, Thermofluor assay, and dynamic light scattering. I performed the crystallization screening experiments, and wrote the manuscript.

Optimization of the crystallizability of a single-chain antibody fragment. Skerlova, J., Kral, V., Fabry, M., Sedlacek, J., Veverka, V. & Rezacova, P. (2014), *Acta Crystallographica Section F, Structural Biology and Crystallization Communications.* 70, 1701-1706.

Acta Crystallographica Section F
Structural Biology Communications
ISSN 2053-230X

Optimization of the crystallizability of a single-chain antibody fragment

Jana Škerlová, Vlastimil Král, Milan Fábry, Juraj Sedláček, Václav Veverka and Pavlína Řezáčová

Acta Cryst. (2014). F**70**, 1701–1706

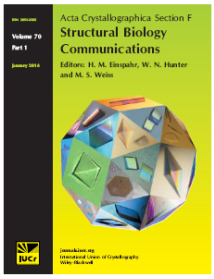

Acta Crystallographica Section F
Structural Biology Communications
ISSN 2053-230X

Optimization of the crystallizability of a single-chain antibody fragment

Jana Škerlová,[a,b,c] Vlastimil Král,[a] Milan Fábry,[a] Juraj Sedláček,[a] Václav Veverka[b] and Pavlína Řezáčová[a,b]*

[a]Institute of Molecular Genetics, ASCR, v.v.i., Vídeňská 1083, 14220 Prague 4, Czech Republic, [b]Institute of Organic Chemistry and Biochemistry, ASCR, v.v.i., Flemingovo nám. 2, 16610 Prague 6, Czech Republic, and [c]Faculty of Science, Charles University in Prague, Albertov 6, 12843 Prague 2, Czech Republic

Correspondence e-mail: rezacova@img.cas.cz

Received 12 September 2014
Accepted 13 October 2014

Single-chain variable antibody fragments (scFvs) are molecules with immense therapeutic and diagnostic potential. Knowledge of their three-dimensional structure is important for understanding their antigen-binding mode as well as for protein-engineering approaches such as antibody humanization. A major obstacle to the crystallization of single-chain variable antibody fragments is their relatively poor homogeneity caused by spontaneous oligomerization. A new approach to optimization of the crystallizability of single-chain variable antibody fragments is demonstrated using a representative single-chain variable fragment derived from the anti-CD3 antibody MEM-57. A Thermofluor-based assay was utilized to screen for optimal conditions for antibody-fragment stability and homogeneity. Such an optimization of the protein storage buffer led to a significantly improved ability of the scFv MEM-57 to yield crystals.

1. Introduction

Knowledge of protein three-dimensional structure is important for understanding protein function. The three-dimensional structure can, amongst other things, also provide a basis for protein-engineering approaches, especially in the case of antibody single-chain variable fragments (scFvs). X-ray crystallography is the principal method used in protein structure determination; close to 90% of all of the protein structures deposited in the Protein Data Bank to date have been determined using this method. The crystallization of the protein represents a common bottleneck in the process of structure determination, as a crystal is an essential requirement for diffraction experiments. The crystallization process is influenced by numerous factors, with the properties of the protein sample being the most important variable (Dale *et al.*, 2003). Therefore, pre-crystallization biochemical and biophysical characterization of the protein sample can help in successful crystallization (Zulauf & D'Arcy, 1992; Ericsson *et al.*, 2006). The use of pre-crystallization analysis is described here in detail for a single-chain variable fragment of the antibody MEM-57.

The monoclonal antibody MEM-57 (murine IgG2) recognizes the human CD3 antigen, which is expressed on the surface of T lymphocytes in complex with the T-cell receptor (Hilgert *et al.*, 1989). CD3 plays a role in the transduction of the activation signal after antigen recognition by the T-cell receptor (Weiss, 1990). The antibody MEM-57 shows similar effects (Hilgert *et al.*, 1989; Pan *et al.*, 2006) to the therapeutic anti-CD3 antibody OKT3 (Kung *et al.*, 1979; muromonab CD3, Orthoclone OKT3), which is used as an immunosuppressant in organ transplantation (Goldstein, 1987; Sgro, 1995; Chatenoud, 2003). The antibody MEM-57 could be used in diagnostics of autoimmune diseases, for T-cell lymphoma classification, as an immunosuppressant in transplantation (Hilgert *et al.*, 1989) or in cancer therapy in the therapeutic antibody format of a bispecific T-cell engager (Wolf *et al.*, 2005). Structural information on scFv MEM-57 would facilitate humanization of the antibody for therapeutic applications.

ScFv fragments are constructed as a fusion of the variable domains of the heavy (V_H) and light (V_L) immunoglobulin chains connected by a flexible linker, which stabilizes the noncovalent interaction between the V_H and V_L (Huston *et al.*, 1988; Bird *et al.*, 1988). The linker sequence $(Gly_4Ser)_3$ (Huston *et al.*, 1988) is universally used, as

Table 1
Sequence of the scFv MEM-57 recombinant fragment.

Heavy-chain variable domain (V_H)	EVQLQQSGGEPMKPGASVKISCKATGYTFNRYWIEWIKQR-PGHGLEWIGEILPGSGKTNYNEKFKGKATFTADISAN-TVHTQISSLTSEDSAVYYCARAYRYDGGYIMDYWGQG-TTVTVS
Linker	GGGGSGGGGSGGGGSGGGGS
Light-chain variable domain (V_L)	DIVMTQSPATLSVIPGDRVSLSCRASQSIRDSLHWYQQKS-HESPRLLIKYASQSISGIPSRFSGSGSGSDFTLSINS-VEPEDVGVYYCQNGHSFPLTFGAGTKLEIKR
c-Myc epitope (cloning artifact)	EQKLISEEDL
His_6 tag (cloning artifact)	NGT-HHHHH

it is flexible, hydrophilic, protease-resistant and does not interact with either domain (Papanastasiou *et al.*, 1999). A length of the linker of between 12 and 25 amino-acid residues (Jäger & Plückthun, 1999; Pantoliano *et al.*, 1991) allows the correct assembly of the two variable domains, resulting preferentially in the monomeric scFv form (Zdanov *et al.*, 1994; Whitlow *et al.*, 1994; Kortt *et al.*, 1994). However, a fraction of domain-swapped scFv dimers and higher oligomers can be also formed, which prevail when shorter linker sequences are used (Power *et al.*, 2003; Kortt *et al.*, 1997; Holliger *et al.*, 1993; Atwell *et al.*, 1999; Carmichael *et al.*, 2003). The preferred oligomeric form of the scFv depends not only on the length of the linker but, amongst other variables, also on the protein concentration and on the pH and the ionic strength of the storage buffer (Arndt *et al.*, 1998), which can be the subject of further optimization.

Here, we use the scFv MEM-57 fragment as a model to demonstrate the general approach of optimization of the storage-buffer composition for scFv fragments in order to enhance their crystallizability.

2. Experimental

2.1. Protein expression and purification

The coding sequences for IgG heavy-chain and light-chain variable domains were obtained from hybridoma total RNA using RT-PCR. The N-terminal primers corresponded either to the amino-acid sequence experimentally determined by N-terminal sequencing or, in the case of a blocked N-terminus, a mixture of degenerate primers (Orlandi *et al.*, 1989) was used. The C-terminal primers corresponded to the conserved sequence of the constant regions adjacent to the variable domains (Kabat *et al.*, 1991). The sequenced PCR products were re-amplified using modified primers to allow assembly of the (V_H)-$(Gly_4Ser)_4$-(V_L) scFv format, followed by a c-Myc tag sequence for anti-Myc antibody detection. Expression vectors were constructed using a modified pET-22b(+) vector, in which the scFv coding sequence is preceded by the pelB signal sequence, targeting the recombinant product into the periplasmic space, and is followed by a His_5 tag for purification.

The expression and isolation procedure was based on previously published protocols (Griep *et al.*, 1999; Kipriyanov *et al.*, 1997; Kaprálek *et al.*, 1991). *Escherichia coli* BL21 (DE3) cells transformed by an expression plasmid were inoculated to a final $OD_{550\,nm}$ of 0.1 in LB medium supplemented with 0.1 mg ml^{-1} ampicillin and 0.4%(*v*/*v*) glycerol and were cultured at 310 K. After reaching an $OD_{550\,nm}$ of 1.0, the cell cultures were supplemented with IPTG to a final concentration of 0.25 m*M* to induce recombinant protein expression and were cultured at 293 K for an additional 4 h. The cells were harvested by centrifugation and the soluble recombinant protein was isolated from the periplasmic space by hypotonic shock. The cells were washed in cold hypertonic buffer [30%(*w*/*v*) sucrose, 50 m*M* Tris pH 8.0, 1 m*M* EDTA, 1 m*M* PMSF; 10 ml of buffer per gram of cell paste] and centrifuged. The periplasmic space was then lysed by 45 min incubation at 273 K and 200 rev min^{-1} in cold hypotonic buffer (5 m*M* $MgSO_4$, 10 m*M* Tris pH 8.0, 1 m*M* PMSF); a volume of 20 ml buffer was used per gram of cell paste. The periplasmic protein fraction was cleared by centrifugation, dialyzed against 50 m*M* NaH_2PO_4 pH 8.0, 300 m*M* NaCl at 277 K and loaded onto an Ni-CAM HC Resin column (Sigma–Aldrich, USA) at a flow rate of 1 ml min^{-1}. The His_5-tagged protein was eluted using a step gradient of imidazole (5, 20, 50 and 200 m*M*). The eluted protein was dialyzed against 20 m*M* diethanolamine pH 8.4 and further purified by ion-exchange chromatography using an ÄKTAbasic FPLC system on a 1 ml MonoQ 5/50 GL Tricorn column (Amersham Biosciences, UK) at a flow rate of 1 ml min^{-1}. The protein was eluted using a segmented gradient of NaCl: 0–200 m*M* NaCl in 20 ml, 200 m*M*–1 *M* NaCl in 10 ml, 1 *M* NaCl in 5 ml and 1–0 *M* NaCl in 5 ml.

The purified protein was concentrated by ultrafiltration using Amicon Ultra concentrators (Merck Millipore, USA) and stored in 20 m*M* diethanolamine pH 8.4, 100 m*M* NaCl or 100 m*M* sodium phosphate pH 7.5, 200 m*M* NaCl at 203 K. Protein purity was monitored by silver-stained SDS–PAGE under nonreducing conditions.

2.2. Size-exclusion chromatography

Analytical size-exclusion chromatography (SEC) was performed using an ÄKTAbasic FPLC system on a 23 ml Superdex 200 10/300 GL Tricorn column (Amersham Biosciences, UK) at a flow rate of 0.5 ml min^{-1} in 20 m*M* diethanolamine pH 8.4, 100 m*M* NaCl or 100 m*M* sodium phosphate pH 7.5, 200 m*M* NaCl.

2.3. Thermofluor assay

The Thermofluor assay was performed according to a previously published protocol (Pisackova *et al.*, 2013; Procházková *et al.*, 2012) based on the procedure described previously (Ericsson *et al.*, 2006; Reinhard *et al.*, 2013). The stabilizing effect of 22 buffers at a concentration of 100 m*M* was tested in the presence or absence of 200 m*M* NaCl; the protein concentration was 0.2 mg ml^{-1}. The melting temperatures (T_m) were determined as the minima of the negative first derivatives of the melting curves using the *LightCycler* 480 Software (Roche, Switzerland).

2.4. Dynamic light scattering

Dynamic light-scattering (DLS) measurements were performed prior to setting up the crystallization trials using 15 µl concentrated (15 mg ml^{-1}) centrifuged protein samples at 532 nm, 90° angle and 293 K on a Laser-Spectroscatter 201 (GmbH Netzwerk RNA-Technologien, Germany).

2.5. Protein crystallization

The scFv MEM-57 protein at a concentration of 15 mg ml^{-1} was used for initial crystallization screening. Screening was performed at 291 K by the sitting-drop vapour-diffusion method with the help of a Gryphon crystallization workstation (Art Robbins Instruments, USA) in 96-well sitting-drop Intelli-Plates (Art Robbins Instruments, USA) using the commercial screening kit The PEGs Suite (Qiagen, Netherlands). A total volume of 450 nl of a mixture of the protein and precipitant solution in a 2:1 ratio, respectively, was equilibrated against 50 µl reservoir solution.

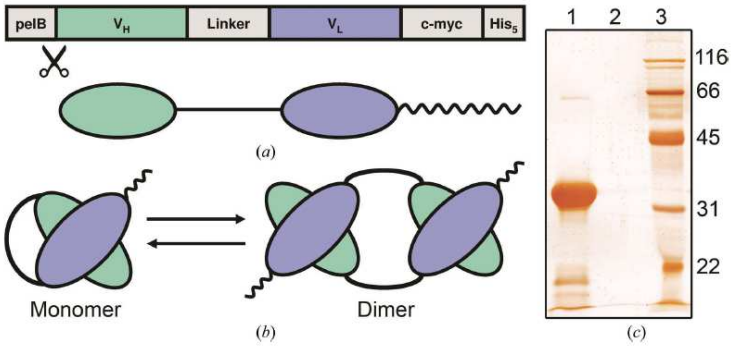

Figure 1
Scheme of the scFv MEM-57 antibody fragment. (*a*) A scheme of the scFv MEM-57 gene construct and the corresponding protein product; V_H and V_L are the variable domains of the heavy and light immunoglobulin chains, respectively, pelB is a leader sequence targeting recombinant product to the periplasm, c-Myc is a ten-amino-acid epitope and His_5 is the pentahistidine purification tag. (*b*) Quaternary structure of the scFv MEM-57 protein. In addition to scFv monomers, domain-swapped inter-chain scFv dimers can be formed. (*c*) The purity of scFv MEM-57 is shown in lane 1 on a silver-stained denaturing SDS–PAGE gel under nonreducing conditions; the molecular-weight standard is in lane 3 (molecular weights are indicated in kDa) and lane 2 is empty.

3. Results and discussion

The single-chain variable fragment (scFv) of the antibody MEM-57 was constructed: variable domains of the heavy and light chains were joined by a flexible linker and further equipped with an N-terminal pelB leader sequence and a C-terminal c-Myc tag and His_5 tag. A longer version of the classical $(Gly_4Ser)_3$ linker (Huston *et al.*, 1988) with the sequence $(Gly_4Ser)_4$ was used to favour the formation of scFv monomers (Table 1, Fig. 1). Fig. 1(*b*) illustrates the formation of inter-chain domain-swapped dimers, a typical feature of scFv fragments, which occurs in solution. To our knowledge, no other type of dimerization has been observed for scFv fragments.

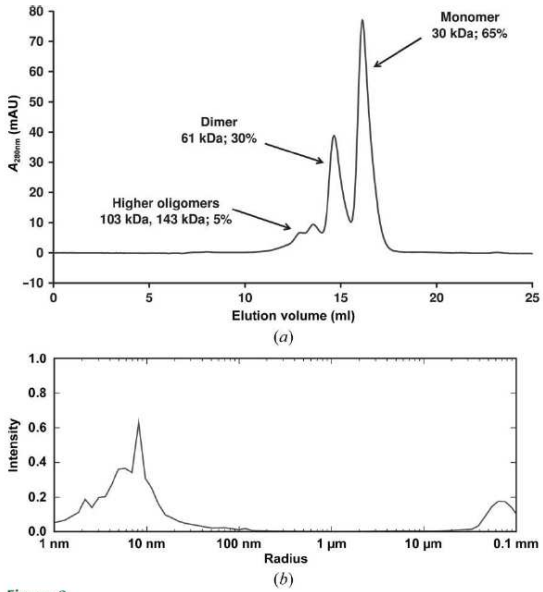

Figure 2
Inhomogeneity of scFv MEM-57 in the original storage buffer (20 m*M* diethanolamine pH 8.4, 100 m*M* NaCl). (*a*) Size-exclusion chromatographic analysis of scFv MEM-57 at 7.5 mg ml^{-1}. Apparent molecular weights are indicated for each peak together with the percentage of the individual oligomeric forms in the total protein content. (*b*) The DLS particle-size distribution reveals polydispersity of scFv MEM-57 at 15 mg ml^{-1}.

The N-terminal pelB leader sequence targets the recombinant product into the periplasmic space of *E. coli* and is cleaved off during transport. In this compartment, disulfide bridges are formed and the recombinant antibody fragment usually accumulates in a soluble form. The recombinant protein was isolated through selective opening of the periplasmic compartment by osmotic shock. A two-step purification protocol employing nickel-chelation chromatography and ion-exchange chromatography produced a moderate yield of pure protein, as analyzed by nonreducing denaturing SDS–PAGE (Fig. 1*c*). The yield of 3 mg scFv MEM-57 per litre of bacterial culture is comparable to the typical yields obtained for other recombinant antibody fragments prepared from *E. coli* periplasm (Kipriyanov *et al.*, 1997; Bayly *et al.*, 2002). The antigen-binding activity of the scFv MEM-57 fragment was confirmed by flow cytometry on CD3-positive Jurkat cells (data not shown).

The ratio between the monomeric and the multimeric forms of the purified scFv fragment was determined by analytical size-exclusion chromatography (SEC) under native conditions. An equilibrium was established between monomer, dimer and higher oligomers of scFv MEM-57 in the original storage buffer, which was 20 m*M* diethanolamine pH 8.4, 100 m*M* NaCl (Fig. 2*a*). The monomeric form represented about 65% of the total protein. Dynamic light scattering (DLS) was also used to evaluate the dispersity of the protein preparation at the high concentration used for crystallization experiments. The DLS analysis revealed protein sample polydispersity (Fig. 2*b*), which indicated a low probability of successful crystallization of the protein (Zulauf & D'Arcy, 1992).

The equilibrium between oligomeric scFv forms was established even after the monomeric and dimeric forms were separated using ion-exchange chromatography (MonoQ column, 20 m*M* diethanolamine pH 8.4, NaCl gradient; for details, see §2.1.). The scFv MEM-57 eluted in two peaks that probably corresponded to the scFv monomer and dimer (data not shown). When each fraction was separately analyzed by SEC analysis, an equilibrium between the monomer, dimer and higher oligomers similar to that shown in Fig. 2(*a*) was observed.

Because the inhomogeneity of the protein originating from the equilibrium between scFv monomer and oligomers is not favourable for protein crystallization, we decided to screen for a buffer

composition which would stabilize the protein in one of the existing forms. The Thermofluor assay (also known as differential scanning fluorimetry) is currently routinely used to screen for optimal protein storage buffer compositions for protein stability and conformational homogeneity (Ericsson *et al.*, 2006; Reinhard *et al.*, 2013). In our case, we not only used Thermofluor to evaluate protein stability, but we also followed the protein oligomeric state, which was reflected by a specific shape of the melting curve. A screen consisting of 22 buffers at pH 4.5–8.5 was used in the presence or absence of 200 m*M* NaCl (Ericsson *et al.*, 2006). Conditions in which the protein exhibited a multiple-inflection melting curve, indicating the presence of multiple oligomeric forms, were excluded from further analysis of the melting temperature (T_m). In the T_m analysis, the buffer in which the protein exhibited a single-inflection curve with the highest T_m (331 K) was selected as the optimal protein storage buffer (100 m*M* sodium phosphate pH 7.5, 200 m*M* NaCl; see Fig. 3). The protein-unfolding curve for the original protein storage buffer also included a second inflection, which was more apparent in the negative first derivative of the curve as a second minimum.

SEC and DLS analyses were performed on the scFv MEM-57 protein in the optimized buffer. SEC confirmed an improved oligomeric homogeneity of the protein sample, as illustrated in Fig. 4(*a*). The equilibrium between the monomer and dimer has shifted significantly in the favour of the monomeric form; the monomer represented 88% of the total protein (compared with 65% of monomer in the original storage buffer). DLS analysis revealed a monomodal particle-size distribution (Fig. 4*b*).

The positive effect of the optimized storage buffer composition on protein crystallizability was confirmed by the results of the initial crystallization trials; protein crystals were obtained in 41 out of 96 screened conditions (Fig. 5).

Selected crystals obtained in the screening diffracted to a maximal resolution of 6 Å (data not shown) when tested for X-ray diffraction at 120 K using a MAR345 image-plate system and a Nonius FR591 rotating-anode generator (Bruker Nonius B.V., Netherlands). Optimization of the diffraction quality of the crystals is currently in progress. This includes optimization of the crystallization conditions, cryoprotection optimization and optimization of the protein construct (specifically introducing cleavable tags at either the C-terminus or the N-terminus). The use of an epitope-derived peptide to stabilize the oligomeric state and/or antigen-binding site, a strategy successfully used previously for other scFv fragments (Rezacova *et al.*, 2001, 2005), cannot be used for our antibody fragment as the epitope of MEM-57 is not linear but structural.

4. Conclusions

Pre-crystallization analysis of protein samples using a combination of biochemical and biophysical methods such as size-exclusion chromatography, dynamic light scattering and the Thermofluor assay can be used to help protein crystallization. We have employed these methods to optimize the stability and also the oligomeric homogeneity of scFv MEM-57 for crystallization. This approach resolved

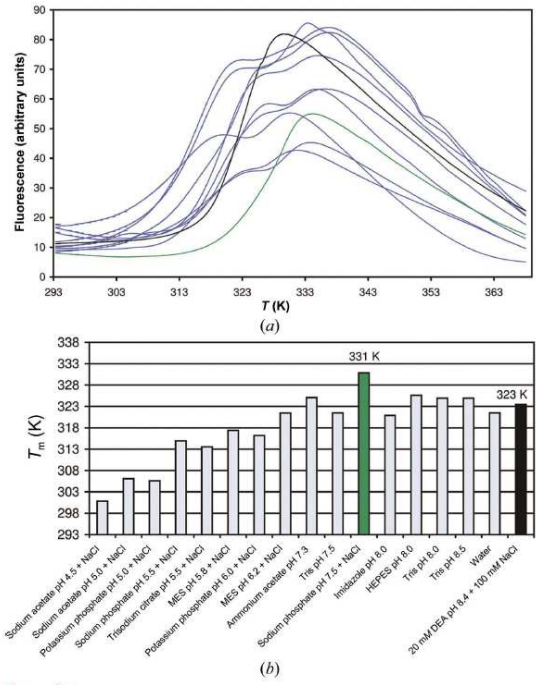

Figure 3
Thermofluor assay for scFv MEM-57. (*a*) Thermofluor-based protein-unfolding curves for the original (black) and optimized (green) storage buffers are shown along with representative multiple-inflection curves which were excluded from further melting-temperature (T_m) analysis (blue). (*b*) Melting temperatures for storage buffers with the melting temperatures of other single-inflection buffers. The original and optimized storage buffers are highlighted in black and green, respectively.

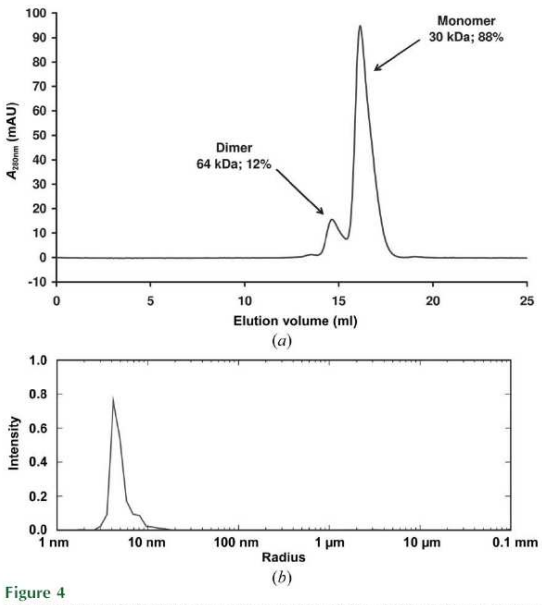

Figure 4
Homogeneity of scFv MEM-57 in the optimized storage buffer (100 m*M* sodium phosphate pH 7.5, 200 m*M* NaCl). (*a*) Size-exclusion chromatographic analysis of scFv MEM-57 at 7.5 mg ml^{-1}. Apparent molecular weights are indicated for each peak together with the percentage of the individual oligomeric forms in the total protein content. The discrepancy in the apparent molecular weights for the scFv dimer in the original and optimized buffer (compare with Fig. 2*a*) might be caused by the regeneration and recalibration of the SEC column between these two runs. (*b*) The DLS particle-size distribution reveals monodispersity of scFv MEM-57 at 15 mg ml^{-1}.

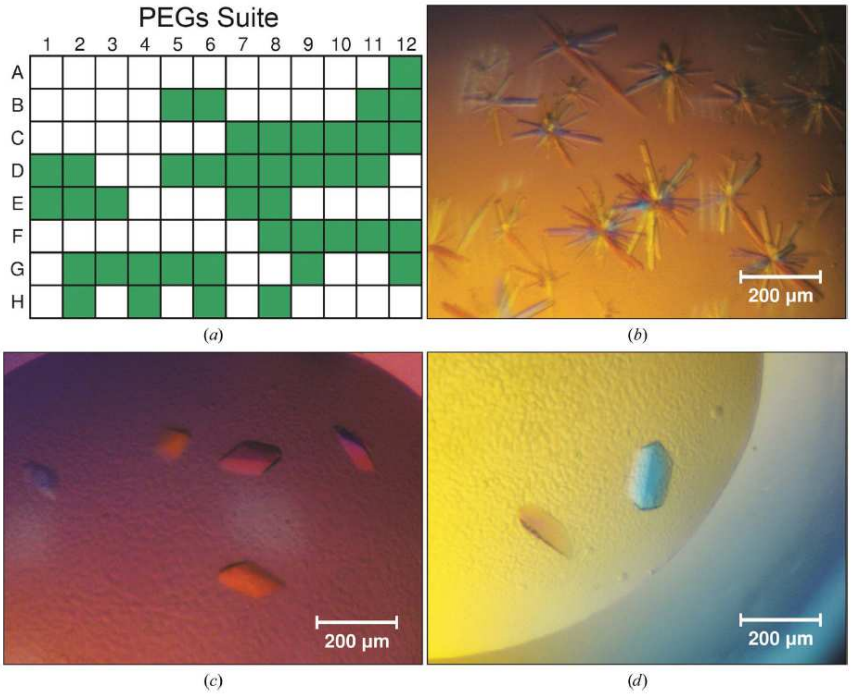

Figure 5
Crystallization of scFv MEM-57 in the optimized storage buffer. (*a*) A scheme of the crystallization screening plate containing The PEGs Suite (Qiagen, Netherlands) is shown with the conditions yielding crystals highlighted in green. (*b*) An example of crystals obtained using 100 m*M* HEPES pH 7.5, 15%(*w*/*v*) PEG 20 000. (*c*) An example of crystals obtained using 200 m*M* sodium fluoride, 20%(*w*/*v*) PEG 3350. (*d*) An example of crystals obtained using 100 m*M* HEPES pH 7.5, 25%(*w*/*v*) PEG 3000.

the issue of unfavourable oligomerization of the scFv fragment by stabilization of the monomeric form and thus resulted in a protein sample with improved crystallizability.

This work was supported by the Charles University in Prague, project GA UK No. 567012. This work was also supported in part by projects RVO 61388963 and 68378050 awarded by the Academy of Sciences of the Czech Republic and by the Ministry of Education of the Czech Republic – LK11205 (program 'NAVRAT').

References

Arndt, K. M., Müller, K. M. & Plückthun, A. (1998). *Biochemistry*, **37**, 12918–12926.
Atwell, J. L., Breheney, K. A., Lawrence, L. J., McCoy, A. J., Kortt, A. A. & Hudson, P. J. (1999). *Protein Eng.* **12**, 597–604.
Bayly, A. M., Kortt, A. A., Hudson, P. J. & Power, B. E. (2002). *J. Immunol. Methods*, **262**, 217–227.
Bird, R. E., Hardman, K. D., Jacobson, J. W., Johnson, S., Kaufman, B. M., Lee, S. M., Lee, T., Pope, S. H., Riordan, G. S. & Whitlow, M. (1988). *Science*, **242**, 423–426.
Carmichael, J. A., Power, B. E., Garrett, T. P. J., Yazaki, P. J., Shively, J. E., Raubischek, A. A., Wu, A. M. & Hudson, P. J. (2003). *J. Mol. Biol.* **326**, 341–351.
Chatenoud, L. (2003). *Nature Rev. Immunol.* **3**, 123–132.
Dale, G. E., Oefner, C. & D'Arcy, A. (2003). *J. Struct. Biol.* **142**, 88–97.
Ericsson, U. B., Hallberg, B. M., DeTitta, G. T., Dekker, N. & Nordlund, P. (2006). *Anal. Biochem.* **357**, 289–298.
Goldstein, G. (1987). *Transplant. Proc.* **19**, 1–6.
Griep, R. A., van Twisk, C., Kerschbaumer, R. J., Harper, K., Torrance, L., Himmler, G., van der Wolf, J. M. & Schots, A. (1999). *Protein Expr. Purif.* **16**, 63–69.
Hilgert, I., Horejsi, V. & Kristofova, H. (1989). Czechoslovakia Patent 253 687.
Holliger, P., Prospero, T. & Winter, G. (1993). *Proc. Natl Acad. Sci. USA*, **90**, 6444–6448.
Huston, J. S., Levinson, D., Mudgett-Hunter, M., Tai, M.-S., Novotný, J., Margolies, M. N., Ridge, R. J., Bruccoleri, R. E., Haber, E., Crea, R. & Oppermann, H. (1988). *Proc. Natl Acad. Sci. USA*, **85**, 5879–5883.
Jäger, M. & Plückthun, A. (1999). *FEBS Lett.* **462**, 307–312.
Kabat, E. A., Wu, T. T., Perry, H. M., Gottesman, K. S. & Foeller, C. (1991). *Sequences of Proteins of Immunological Interest*, 5th ed. Bethesda: National Institutes of Health.
Kaprálek, F., Jecmen, P., Sedlácek, J., Fábry, M. & Zadrazil, S. (1991). *Biotechnol. Bioeng.* **37**, 71–79.
Kipriyanov, S. M., Moldenhauer, G. & Little, M. (1997). *J. Immunol. Methods*, **200**, 69–77.
Kortt, A. A., Lah, M., Oddie, G. W., Gruen, C. L., Burns, J. E., Pearce, L. A., Atwell, J. L., McCoy, A. J., Howlett, G. J., Metzger, D. W., Webster, R. G. & Hudson, P. J. (1997). *Protein Eng.* **10**, 423–433.
Kortt, A. A., Malby, R. L., Caldwell, J. B., Gruen, L. C., Ivancic, N., Lawrence, M. C., Howlett, G. J., Webster, R. G., Hudson, P. J. & Colman, P. M. (1994). *FEBS J.* **221**, 151–157.
Kung, P., Goldstein, G., Reinherz, E. L. & Schlossman, S. F. (1979). *Science*, **206**, 347–349.
Orlandi, R., Güssow, D. H., Jones, P. T. & Winter, G. (1989). *Proc. Natl Acad. Sci. USA*, **86**, 3833–3837.
Pan, Q., Brodeur, J. F., Drbal, K. & Dave, V. P. (2006). *Mol. Immunol.* **43**, 1741–1750.
Pantoliano, M. W., Bird, R. E., Johnson, S., Asel, E. D., Dodd, S. W., Wood, J. F. & Hardman, K. D. (1991). *Biochemistry*, **30**, 10117–10125.
Papanastasiou, D., Mamalaki, A., Eliopoulos, E., Poulas, K., Liolitsas, C. & Tzartos, S. J. (1999). *J. Neuroimmunol.* **94**, 182–195.
Pisackova, J., Prochazkova, K., Fabry, M. & Rezacova, P. (2013). *Cryst. Growth Des.* **13**, 844–848.
Power, B. E., Doughty, L., Shapira, D. R., Burns, J. E., Bayly, A. M., Caine, J. M., Liu, Z., Scott, A. M., Hudson, P. J. & Kortt, A. A. (2003). *Protein Sci.* **12**, 734–747.

Procházková, K., Čermáková, K., Pachl, P., Sieglová, I., Fábry, M., Otwinowski, Z. & Řezáčová, P. (2012). *Acta Cryst.* D**68**, 176–185.
Reinhard, L., Mayerhofer, H., Geerlof, A., Mueller-Dieckmann, J. & Weiss, M. S. (2013). *Acta Cryst.* F**69**, 209–214.
Rezacova, P., Brynda, J., Lescar, J., Fabry, M., Horejsi, M., Sieglova, I., Sedlacek, J. & Bentley, G. A. (2005). *J. Struct. Biol.* **149**, 332–337.
Rezacova, P., Lescar, J., Brynda, J., Fabry, M., Horejsi, M., Sedlacek, J. & Bentley, G. A. (2001). *Structure*, **9**, 887–895.
Sgro, C. (1995). *Toxicology*, **105**, 23–29.
Weiss, A. (1990). *J. Clin. Invest.* **86**, 1015–1022.
Whitlow, M., Filpula, D., Rollence, M. L., Feng, S. L. & Wood, J. F. (1994). *Protein Eng.* **7**, 1017–1026.
Wolf, E., Hofmeister, R., Kufer, P., Schlereth, B. & Baeuerle, P. A. (2005). *Drug Discovery Today*, **10**, 1237–1244.
Zdanov, A., Li, Y., Bundle, D. R., Deng, S.-J., MacKenzie, C. R., Narang, S. A., Young, N. M. & Cygler, M. (1994). *Proc. Natl Acad. Sci. USA*, **91**, 6423–6427.
Zulauf, M. & D'Arcy, A. (1992). *J. Cryst. Growth*, **122**, 102–106.

7.4 Molecular mechanism for the action of the anti-CD44 monoclonal antibody MEM-85

Background

Human hyaluronate receptor CD44 plays an important role in various physiological processes including cell adhesion and migration, such as hematopoiesis, lymphocyte homing, tissue healing, but also tumor metastasis. The transmembrane glycoprotein CD44 binds hyaluronate through the extracellular hyaluronate-binding domain (HABD), which induces an allosteric conformational change, resulting in CD44 HABD shedding. Murine monoclonal antibody MEM-85 recognizes CD44 HABD and might be of therapeutic interest as it has been shown to inhibit growth of lung cancer cells in murine models. MEM-85 cross-blocks hyaluronate binding to CD44 and also induces CD44 shedding, similar to hyaluronate-induced CD44 shedding, by an unknown mechanism. The epitope recognized by MEM-85 has not been unambiguously identified. Therefore, a detailed structural study of the MEM-85 – CD44 HABD interaction would shed light on the molecular mechanism of MEM-85 function.

Summary

We constructed a single-chain variable fragment (scFv) of murine antibody MEM-85 against the hyaluronate-binding domain (HABD) of human CD44. Flow cytometry and fluorescence microscopy confirmed that scFv MEM-85 binds native CD44 on cell surface. Thermofluor assay revealed high thermal stability of the antibody fragment. We prepared recombinant $^{15}N/^{13}C$-labeled CD44 HABD, which was able to bind hyaluronate, as shown by NMR. We analyzed the antigen binding of both scFv and IgG MEM-85 using surface plasmon resonance (SPR). Preparation of a stable homogeneous complex of scFv MEM-85 and CD44 HABD allowed us to employ NMR and small-angle X-ray scattering (SAXS) analyses. We acquired a set of three-dimensional NMR spectra for the sequence-specific backbone resonance assignments for CD44 HABD. We used the minimal shift approach to assess the extent of the chemical shift perturbation upon scFv MEM-85 binding. By this approach, we identified the epitope, located in the C-terminal portion of CD44 HABD, which was corroborated with the results of a mutational analysis of the identified epitope residues combined with SPR measurements. Finally, we obtained a low-resolution *ab initio* SAXS structure of the complex together with a rigid body model of the complex using the

available high-resolution structures. The key results of the publication are summarized in Figure 11.

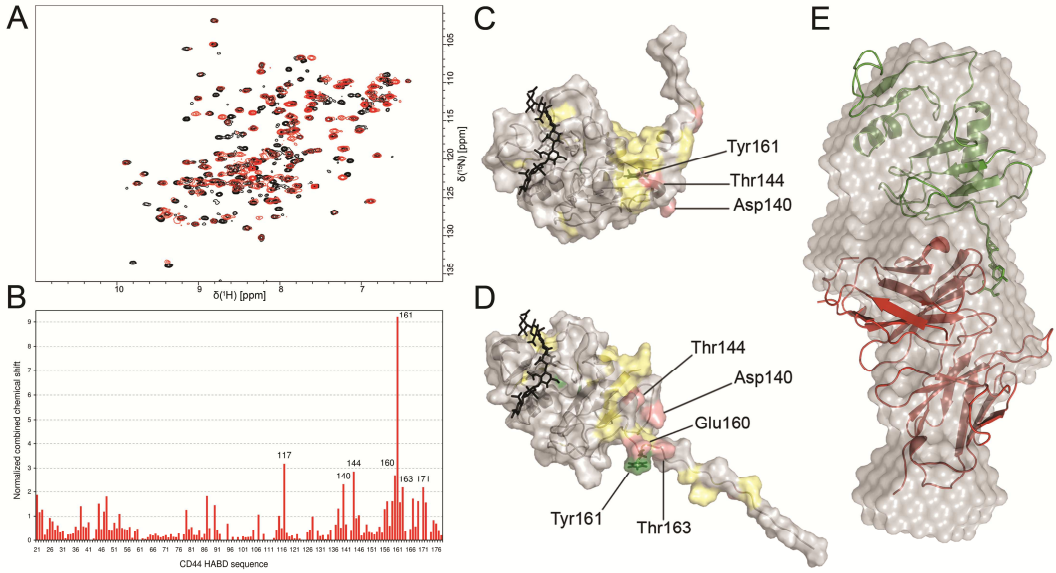

Figure 11: Identification of MEM-85 binding epitope in CD44 HABD
A: Two-dimensional $^{15}N/^{1}H$ HSQC spectra are shown for free $^{15}N/^{13}C$-CD44 HABD (black) and $^{15}N/^{13}C$-CD44 HABD in complex with scFv MEM-85 (red). B: Histogram of minimal combined chemical shift versus the protein sequence is shown for $^{15}N/^{13}C$-CD44 HABD. C: Significantly perturbed residues are mapped on the surface of free CD44 HABD. D: Significantly perturbed residues are mapped on the surface of hyaluronate-bound CD44 HABD. E: SAXS *ab initio* envelope (grey) is shown in superposition with the rigid body model of scFv MEM-85 (red) and CD44 HABD (green).

My contribution

I participated in the construction of the CD44 HABD expression vectors, prepared protein samples for all experiments, participated in the flow cytometry and fluorescence microscopy experiments, performed size-exclusion chromatography, dynamic light scattering, and Thermofluor assay. I performed the sequence-specific backbone NMR assignments and the chemical shift perturbation analysis by the minimal shift method. I prepared samples for SAXS measurements, participated in SAXS data analysis, and I wrote the manuscript.

Molecular mechanism for the action of the anti-CD44 monoclonal antibody MEM-85. Skerlova, J., Kral, V., Kachala, M., Fabry, M., Bumba, L., Svergun, D. I., Tosner, Z., Veverka V. & Rezacova, P. (2015), under consideration in *Journal of Structural Biology.*

Molecular mechanism for the action of the anti-CD44 monoclonal antibody MEM-85

Jana Škerlová[a,b,c], Vlastimil Král[b], Michael Kachala[d], Milan Fábry[b], Ladislav Bumba[e], Dmitri I. Svergun[d], Zdeněk Tošner[f], Václav Veverka[a,*], and Pavlína Řezáčová[a,b,*]

[a]Institute of Organic Chemistry and Biochemistry, AS CR, v.v.i., Flemingovo nam. 2, Prague 6, 166 10, Czech Republic; [b]Institute of Molecular Genetics, AS CR, v.v.i., Videnska 1083, Prague 4, 142 20, Czech Republic; [c]Department of Biochemistry, Faculty of Science, Charles University in Prague, Albertov 6, 128 40 Prague 2, Czech Republic; [d]European Molecular Biology Laboratory, Hamburg Outstation, c/o Deutsches Elektronen-Synchrotron (DESY), Notkestrasse 85, D-22603 Hamburg, Germany; [e]Institute of Microbiology, AS CR, v.v.i., Videnska 1083, Prague 4, 142 20, Czech Republic; [f]Faculty of Science, Charles University in Prague, Albertov 6, 128 40 Prague 2, Czech Republic

[*]To whom correspondence should be addressed: Pavlína Řezáčová, Institute of Organic Chemistry and Biochemistry of the ASCR, v.v.i., Flemingovo nam. 2, Prague 6, 166 10, Czech Republic; tel: +420 220 183 144; fax: +420 220 183 144; e-mail: rezacova@uochb.cas.cz

Correspondence may also be addressed to Václav Veverka, Institute of Organic Chemistry and Biochemistry of the ASCR, v.v.i., Flemingovo nam. 2, Prague 6, 166 10, Czech Republic; tel: +420 220 183 135; fax: +420 220 183 144; e-mail: veverka@uochb.cas.cz

Abstract

The hyaluronate receptor CD44 plays role in cell adhesion and migration and is involved in tumor metastasis. The extracellular domain of CD44 comprises the hyaluronate-binding domain (HABD) and the membrane-proximal stem region; the short intracellular portion interacts with adaptor proteins and triggers signaling pathways. Binding of hyaluronate to CD44 HABD induces an allosteric conformational change, which results in CD44 shedding. A poorly characterized epitope in human CD44 HABD is recognized by the murine monoclonal antibody MEM-85, which cross-blocks hyaluronate binding to CD44 and also induces CD44 shedding. MEM-85 is of therapeutic interest, as it inhibits growth of lung cancer cells in murine models. In this work, we employed a combination of biophysical methods to determine the MEM-85 binding epitope in CD44 HABD and to provide detailed insight into the mechanism of MEM-85 action. In particular, we constructed a single-chain variable fragment (scFv) of MEM-85 as a tool for detailed characterization of the CD44 HABD – antibody complex and identified residues within CD44 HABD involved in the interaction with scFv MEM-85 by NMR spectroscopy and mutational analysis. In addition, we built a rigid body model of the CD44 HABD – scFv MEM-85 complex using a low-resolution structure obtained by small-angle X-ray scattering. The MEM-85 epitope is situated in the C-terminal part of CD44 HABD, rather than the hyaluronate-binding groove, and the binding of MEM-85 induces a structural reorganization similar to that induced by hyaluronate. Therefore, the mechanism of MEM-85 cross-blocking of hyaluronate binding is likely of an allosteric, relay-like nature.

Keywords

CD44, epitope mapping, monoclonal antibody, MEM-85, NMR, SAXS

Abbreviations

CDR – complementarity determining region, D_{max} – maximum particle distance, FBS – fetal bovine serum, GAM – goat anti-mouse, HABD – hyaluronate-binding domain, HSQC – heteronuclear single quantum coherence, $I(0)$ – forward scattering, IPTG - isopropyl β-D-1-thiogalactopyranoside, *MM* – molecular mass, O – ordered, PBS – phosphate buffered saline, PD – partially disordered, PDB – Protein Data Bank, $P(r)$ – pair-distance distribution function, R_g – radius of gyration, s – scattering vector, SAXS – small-angle X-ray scattering, scFv – single-chain variable fragment, SPR – surface plasmon resonance, TEV – tobacco etch

virus, V_H – variable domain of the IgG heavy chain, V_L – variable domain of the IgG light chain, V_p – Porod volume, wt – wild type

INTRODUCTION

CD44, a type I transmembrane glycoprotein expressed in many mammalian cells, is the principal receptor for hyaluronate (Aruffo et al., 1990), a major component of the extracellular matrix, and plays an important role in cell adhesion and migration. These cellular events are involved in numerous biological processes, including hematopoiesis and lymphocyte homing (Naor et al., 1997), which is initiated by a CD44 mediated rolling adhesion of lymphocytes to endothelial cells presenting hyaluronate (DeGrendele et al., 1996). CD44 also plays a role in various pathological processes, such as tumor-cell migration and metastasis (Nagano and Saya, 2004; Naor et al., 1997).

The extracellular portion of CD44 comprises an N-terminal hyaluronate-binding domain (HABD), followed by a glycosylated stem region. Alternative splicing of the CD44 gene results in several stem region variants. The cytoplasmic tail of CD44 interacts with the cytoskeleton and is involved in intracellular signaling (Ponta et al., 2003). Three-dimensional structures of mouse and human HABD have been solved both by NMR and X-ray crystallography (Banerji et al., 2007; Takeda et al., 2006; Teriete et al., 2004). HABD adopts a novel form of C-lectin-type fold, which can be denoted as: β0 - β0' - **β1 - α1 - α2 - β3 - β4 - β5 - β6 -** β7 - β8 - β9 - α3 (Fig. 6A). The hyaluronate-binding Link module (in bold), conserved among the family of hyaluronate-binding proteins (Day and Prestwich, 2002), is extended in HABD by an extension lobe formed by β0 and β0' at the N-terminus and a C-terminal extension comprising β7, β8, β9, and α3 (Teriete et al., 2004). This additional extension lobe is essential for structural integrity and hyaluronate binding (Banerji et al., 1998; Peach et al., 1993).

The NMR structure of HABD in complex with hyaluronate (Takeda et al., 2006) revealed that the protein undergoes a significant allosteric conformational change upon ligand binding. In this rearrangement, the β9 strand and α3 helix become unstructured, and the β8 strand changes its position relative to the β0 strand, which provides enhanced flexibility of the HABD C-terminus (Takeda et al., 2006). Therefore, the ligand-free state is referred to as "ordered" (O) and the ligand-bound state as "partially disordered" (PD). The murine CD44 HABD structure in the O-conformation has also been captured by X-ray crystallography in the ligand-bound state, since the ordered state is favorable for crystallization (Banerji et al.,

2007). Both conformational states of CD44 HABD exhibit affinity toward hyaluronate and exist in a two-state conformational equilibrium (Ogino et al., 2010). In comparison to the O-conformation, the PD-conformation exhibits higher affinity toward hyaluronate and higher resistance to cell detachment from a hyaluronate-coated surface (Ogino et al., 2010).

The conformational equilibrium between the PD and O states has been proposed to be essential for formation of new receptor-ligand interactions at the rolling front and their disruption at the rear edge in CD44-mediated cell rolling (Ogino et al., 2010). The ligand-induced shift in equilibrium toward the PD-conformation also "extends" the membrane-proximal stem region of CD44 and thus enhances the proteolytic susceptibility of cleavage sites in the stem region (Takeda et al., 2006). This mechanism of ligand-induced CD44 shedding is involved in the regulation of cell motility and migration (Cichy and Pure, 2003; Nagano and Saya, 2004; Okamoto et al., 1999).

The murine IgG2 antibody MEM-85 raised against human CD44 HABD (Bazil et al., 1989) has been shown to block hyaluronate binding to CD44 (Bajorath et al., 1998; Sandmaier et al., 1998). MEM-85 antibody binding induces CD44 shedding, similar to hyaluronate-induced CD44 shedding (Bazil and Horejsi, 1992) MEM-85 might be of therapeutic interest, as it has recently been shown to inhibit growth of lung cancer cells in murine models (Godar, S., personal communication). The HABD epitope recognized by MEM-85 has not yet been unambiguously identified. Results from a mutational analysis suggested that the epitope lies at the N-terminal part of HABD (Anstee et al., 1991; Bajorath et al., 1998; Stefanova et al., 1989), and residues Lys38, Arg41, and Tyr42 have been shown to be important for MEM-85 binding (Bajorath et al., 1998). Some consider the MEM-85 epitope to be structural (Bajorath et al., 1998), while others have shown that MEM-85 binds CD44 under denaturing non-reducing conditions (Stefanova et al., 1989), which implicates a sequential epitope additionally stabilized by a disulfide bridge.

Here, we present a detailed characterization of the interaction of MEM-85, a monoclonal antibody with therapeutic potential, with hyaluronate receptor CD44 implicated in tumor-cell migration. With the aim of exploring rather enigmatic epitope recognized by MEM-85, we constructed a single-chain variable fragment (scFv) of MEM-85 and prepared its stable complex with CD44 HABD. We carried out epitope mapping by NMR chemical shift perturbation analysis, which allowed us to identify the epitope of MEM-85 antibody in CD44 HABD and uncover the structural changes induced by antibody binding. Using small-angle X-ray scattering (SAXS), we modeled the complex of CD44 HABD and scFv MEM-85, which provided further insight into the mechanism of MEM-85 action.

MATERIAL AND METHODS

Construction of CD44 HABD expression plasmid

Construction of *pCD44HABD* was based on the work of Banerji et al. (1998) and Teriete et al. (2004). HABD, which encompasses residues 21-178 of transcript variant 4 of human CD44, was amplified from cloned cDNA (Cat. No. SC128160, OriGene, Rockville, MD, USA) using the following primers: forward, 5'-GCCCGCTAGCCAGATCGATTTGAATATAACC; reverse, 5'-CCGAATTCACACGTCATCATCAGTAGGGTTG. To obtain a construct of CD44 HABD with a His_6 tag, the vector *pMCSG7* (T7 promoter-driven, originally designed for ligation-independent cloning) (Stols et al., 2002) was modified so that the N-terminal His_6 tag was followed by a TEV (tobacco etch virus) protease cleavage site and amino acid residues SNAAS, where AS corresponds to an *Nhe*I site. The CD44 HABD coding fragment was, after sequence verification, cloned as an *Nhe*I - *EcoR*I insert (recognition sites are underlined in the primer sequences) into this modified vector. Cleavage with TEV protease thus yields a product in which CD44 HABD (residues 21-178) is preceded by SNAAS at the N-terminus.

CD44 HABD mutations D140 + T144A, Y161A, and E160A + T163A were introduced into the coding sequence of CD44 HABD in *pUC18* according to the QuikChange Site-Directed Mutagenesis Protocol (Stratagene, La Jolla, CA, USA) using the following pairs of mutagenic primers: D140 + T144 (5'-CCAATGCCTTTGCCGGCCCAATTGCCATAACTATTG, 5'-CAATAGTTATGGCAATTGGGCCGGCAAAGGCATTGG), Y161A (5'-GTCCAG AAAGGAGAAGCGCGCACGAATCCTGAAGAC, 5'-GTCTTCAGGATTCGTGCGCGC TTCTCCTTTCTGGAC), E160 + T163 (5'-GTCCAGAAAGGAGCATACCGCGCGAAT CCTGAAGAC, 5'-GTCTTCAGGATTCGCGCGGTATGCTCCTTTCTGGAC). After sequence verification, the *Nhe*I-*EcoR*I fragments carrying the respective mutations were used to replace the wild-type fragment in the *pCD44HABD* expression plasmid.

Expression and purification of CD44 HABD

The expression and purification of CD44 HABD was based on a published protocol (Banerji et al., 1998). Recombinant CD44 HABD was expressed in *E. coli* BL21 (DE3) in the LB medium. Transformed cells were grown at 37 °C to an optical density $OD_{550\ nm}$ of 1.5 and induced by addition of isopropyl β-D-1-thiogalactopyranoside (IPTG) to a final concentration of 0.4 mM. At 4 h post-induction, cells were harvested, suspended in wash buffer (50 mM

Tris, pH 8.0, 50 mM NaCl, 5 mM EDTA), taken through one cycle of freezing and thawing, partially homogenized using a Dounce homogenizer and taken through four cycles of homogenization on EmulsiFlex-C3 (Avestin, Ottawa, ON, Canada). The inclusion body pellet was sonicated (three 60-s pulses) on ice in 10% (v/v) Triton X-100 in wash buffer and centrifuged. The Triton-washed pellet was sonicated (three 60-s pulses) on ice in wash buffer and centrifuged. This procedure yielded purified inclusion bodies, which were denatured in 50 mM MES, pH 6.5, 8 M urea, 0.1 mM EDTA, 0.1 mM DTT (120 mg/ml inclusion bodies) by rotating overnight at 4 °C. After removal of insoluble material by centrifugation, the protein was refolded by rapid 250-fold dilution into 100 mM Tris, pH 8.5, 400 mM L-arginine, 2.5 mM reduced glutathione, 2.5 mM oxidized glutathione (480 μM CD44 HABD) and slowly stirred at 4 °C for 48 h before dialysis into 50 mM NaH_2PO_4, pH 8.0, 300 mM NaCl for nickel-chelation chromatography. Refolded protein was concentrated by nickel-chelation chromatography on 9 ml HIS-Select Nickel Affinity Gel column (Cat. No. P6611, Sigma-Aldrich, St. Louis, MO, USA) in 50 mM NaH_2PO_4, pH 8.0, 300 mM NaCl with a flow rate of 1 ml/min and eluted using 200 mM imidazole. Eluted protein was dialyzed into phosphate-buffered saline (PBS) and further purified by size-exclusion chromatography using an Äkta Basic FPLC system with a 124 ml HiLoad 16/600 Superdex 200 pg column (GE Healthcare, Little Chalfont, UK) in PBS at a flow rate of 1 ml/min. The N-terminal His_6 tag was removed by incubation with His_6-tagged TEV protease in PBS at 4 °C for 48 h. The cleaved product was separated from His_6-tagged TEV protease and uncleaved CD44 HABD by nickel-chelation chromatography on 2 ml HIS-Select Nickel Affinity Gel column (Cat. No. P6611, Sigma-Aldrich, St. Louis, MO, USA) in PBS with a flow rate of 1 ml/min. Recombinant product was concentrated in an Amicon Ultra concentrator (Merck Millipore, Billerica, MA, USA), and protein purity was analyzed by 15% SDS-PAGE according to Laemmli (1970). For the preparation of $^{15}N/^{13}C$-labeled protein, cells were grown in minimal medium supplemented with 1 g/l $(^{15}NH_4)_2SO_4$ (Cat. No. NLM-713-10, Cambridge Isotope Laboratories Inc., Tewksbury, MA, USA) and 4 g/l ^{13}C-*D*-glucose (Cat. No. CLM-1396-5, Cambridge Isotope Laboratories Inc., Tewksbury, MA, USA) (Renshaw et al., 2004; Veverka et al., 2006).

Construction of scFv MEM-85 expression plasmid

The coding sequences for the variable domains of the monoclonal antibody MEM-85 heavy and light chains (V_H and V_L, respectively) were obtained by RT-PCR using total RNA from MEM-85 hybridoma cells (kindly provided by Václav Hořejší, Institute of Molecular

Genetics, AS CR, v.v.i.). The N-terminal primers reflected the experimentally determined amino acid sequences, and the C-terminal primers corresponded to constant regions adjacent to the variable domains (Kabat et al., 1991). PCR products were sequenced and used as templates for reamplification with modified primers, allowing assembly of the V_L and V_H coding DNA fragments into the scFv molecule in the format (V_H)-$(Gly_4Ser)_4$-(V_L). The scFv molecule contains 115 N-terminal residues from the heavy chain linked to 114 N-terminal residues from the light chain, followed by a c-myc tag sequence (EQKLISEEDL) to allow detection of scFv MEM-85 with anti-myc antibody and by a His_5 tag to allow product isolation and purification by nickel-chelation chromatography. For expression in *E. coli* BL21(DE3) cells, we used the pET22b(+)-derived vector, *pscFvMEM-85*, in which the scFv coding sequence is preceded by the pelB signal sequence, directing translocation of the product into the periplasmic space.

Expression and purification of scFv MEM-85

Recombinant scFv MEM-85 was expressed in *E. coli* BL21 (DE3) in the LB medium. Transformed cells were grown at 37 °C to the optical density $OD_{550\ nm}$ of 1.0, induced by addition of IPTG to a final concentration of 0.25 mM, and cultured at 20 °C. At 4 h post-induction, cells were harvested. The product, which accumulated in a soluble form in the periplasmic space of the host cells, was isolated by hypotonic shock and purified by nickel-chelation chromatography on 6 ml HIS-Select Nickel Affinity Gel column (Cat. No. P6611, Sigma-Aldrich, St. Louis, MO, USA) in 50 mM NaH_2PO_4, pH 8.4, 300 mM NaCl with a flow rate of 1 ml/min. Bound protein was eluted using a segmented gradient of imidazole. The protein was further purified by ion-exchange chromatography on a 1 ml MonoQ 5/50 GL Tricorn column mounted on an Äkta Basic FPLC system (GE Healthcare, Little Chalfont, UK) in 20 mM diethanolamine, pH 8.4, using a segmented gradient of NaCl. Finally, the recombinant product was concentrated in Amicon Ultra concentrators (Merck Millipore, Billerica, MA, USA), and protein purity was analyzed by 15% SDS-PAGE according to Laemmli (1970).

Biochemical and biophysical characterization of proteins

Size-exclusion chromatography

Formation of the complex of CD44 HABD and scFv MEM-85 was analyzed by size-exclusion chromatography using an Äkta Basic FPLC system on a 23 ml Superdex 200

10/300 GL Tricorn column (GE Healthcare, Little Chalfont, UK) in phosphate-buffered saline (PBS) at a flow rate of 0.5 ml/min.

Thermofluor assay

Thermofluor assay was performed according to published protocols (Pisackova et al., 2013; Prochazkova et al., 2012; Skerlova et al., 2014), based on the procedure described by Ericsson et al. (2006). The stabilizing effects of 22 buffers (100 mM concentrations) were tested in the presence or absence of 200 mM NaCl; the protein concentration was 0.2 mg/ml.

Fluorescence microscopy

Fluorescence microscopy was performed to assay the antigen binding activity of recombinant scFv MEM-85. $CD44^+$ MOLT-4 cells were cultured overnight at 37 °C on poly-L-lysine-coated microscopic cover slides. After formaldehyde fixation and blocking with 10% fetal bovine serum (FBS) in PBS, the cells were incubated in a humidity chamber for 1 hour with scFv MEM-85 or IgG MEM-85 (Cat. No. 11-221-C100, Exbio, Vestec, Czech Republic) at concentrations ranging from 1 μM to 100 nM in 10% FBS in PBS, washed in PBS, and incubated for 1 hour with FITC-conjugated secondary antibodies: anti-c-myc/FITC clone 9E10 (Cat. No. 1F-433-C100, Exbio, Vestec, Czech Republic) for scFv MEM-85 and GAM/FITC (goat anti-mouse antibody conjugated with fluorescein isothiocyanate, Cat. No. 115-095-164, Jackson ImmunoResearch Laboratories, West Grove, PA, USA) for IgG MEM-85 (30 nM in 10% FBS in PBS). The slides were washed in PBS, treated with 78 mg/ml mowiol, 1.5 μg/ml N-propylgalate and 6.3 mg/ml DAPI, and analyzed using an Olympus IX81 fluorescence microscope (Olympus, Shinjuku, Tokio, Japan).

Flow cytometry

Flow cytometry was performed on $CD44^+$ MOLT-4 cells and $CD44^-$ Jurkat cells to assay the antigen binding activity of recombinant scFv MEM-85. Cells ($2 \cdot 10^5$ cells per well) were incubated for 20 minutes on ice in a microtiter U-bottom plate (Nalge Nunc International, Penfield, NY, USA) with scFv or IgG MEM-85 (Cat. No. 11-221-C100, Exbio, Vestec, Czech Republic) at concentrations ranging from 10 μM to 10 nM in 1% BSA in PBS. After washing in PBS, cells were incubated for 20 minutes on ice with the following secondary FITC-conjugated antibodies: anti-c-myc/FITC clone 9E10 (Cat. No. 1F-433-C100, Exbio, Vestec, Czech Republic) for scFv MEM-85 and GAM/FITC (Cat. No. 115-095-164, Jackson ImmunoResearch Laboratories, West Grove, PA, USA) for IgG MEM-85 (30 nM in 1% BSA in PBS). After washing in PBS, cells were suspended in 200 μl PBS supplemented with 1 μg/ml propidium iodide and measured on FACS Aria (Becton, Dickinson and

Company, Franklin Lakes, NJ, USA). The data were analyzed using FlowJo 7.2.5 software (Tree Star, Ashland, OR, USA).

Surface plasmon resonance

All surface plasmon resonance (SPR) measurements were performed at 25 °C using an HTG sensor chip mounted on a ProteOn XPR36 Protein Interaction Array System (Bio-rad, Hercules, CA, USA). The His-tagged proteins were diluted to final concentrations of 20 µg/ml (scFv MEM-85) or 5 µg/ml (CD44 HABD wild-type, wt, or mutants) in running buffer (PBS with 0.05% Tween 20) and captured on a Ni^{2+}-NTA-functionalized HTG chip (Bio-rad, Hercules, CA, USA) at a flow rate of 30 µl/min using a ProteOn HTG Capturing Kit (Bio-rad, Hercules, CA, USA). The analyte proteins were serially diluted in the running buffer (0.312, 0.625, 1.25, 2.5, and 5 µM CD44 HABD; 31, 62, 125, 250, and 500 nM IgG MEM-85 – Cat. No. 11-221-C100, Exbio, Vestec, Czech Republic) and injected in parallel over the immobilized proteins at a flow rate of 30 µl/min. The sensorgrams were corrected for the sensor background by interspot referencing (the sites within the 6×6 array which were not exposed to ligand immobilization but were exposed to analyte flow), and double-referenced by subtraction of analyte (channels 1–5) using a "blank" injection (channel 6). The data were analyzed globally by fitting both the association and dissociation phases simultaneously for five different analyte concentrations using the 1:1 Langmuir-type binding model and the bivalent analyte model to determine the kinetic rate constants. The Langmuir-type model assumes the interaction between proteins A and B resulting in a direct formation of the final complex: A + B ↔ AB, where k_a and k_d are the association and dissociation rate constants, respectively. The equilibrium dissociation constant, K_D, was determined as $K_D = k_d/k_a$. The bivalent analyte model assumes a two-step process: A + B ↔ AB → AB + B ↔ AB_2, where formation of the AB complex is followed by subsequent interaction of the AB complex with another B molecule. Parameters k_{a1} and k_{d1} are the rate constants for the formation of the AB complex, while k_{a2} and k_{d2} are the rate constants for the formation of the AB_2 complex. An apparent equilibrium dissociation constant, K_{D1}, was determined as $K_{D1} = k_{d1}/k_{a1}$.

Epitope mapping

NMR spectroscopy

Sets of double- and triple-resonance NMR spectra were acquired at 308 K on a 600 MHz Bruker Avance spectrometer with triple-resonance ($^{15}N/^{13}C/^{1}H$) cryoprobes (Bruker, Billerica, MA, USA) for a 300 µl sample containing 580 µM $^{15}N/^{13}C$-labeled CD44 HABD and for a 250 µl sample containing 150 µM $^{15}N/^{13}C$-labeled CD44 HABD and 300 µM unlabeled scFv

MEM-85. Two-dimensional $^{15}N/^{1}H$ HSQC (heteronuclear single quantum coherence) spectra were acquired for a 350 µl sample containing 100 µM ^{15}N-labeled CD44 HABD, and for a 350 µl sample containing 200 µM ^{15}N-labeled CD44 HABD and 210 to 620 µM hyaluronate hexamer (Contipro Group, Dolni Dobrouc, Czech Republic). The sample buffer was PBS supplemented with 5% D_2O. Essentially complete sequence-specific resonance assignment was obtained for free CD44 HABD, as previously described (Renshaw et al., 2004; Veverka et al., 2006). To determine the epitope in CD44 HABD, antibody-induced perturbations of $^{15}N/^{13}C$-labeled CD44 HABD signals in HNCO spectra were monitored employing the minimal backbone chemical shift method (^{15}N, $^{13}C'$, and ^{1}H) (Cheng et al., 2013). The minimum changes in the positions of HNCO peaks for the free and antibody-bound CD44 HABD were calculated and plotted against the protein sequence. This histogram identified CD44 HABD residues significantly affected by antibody binding, which were mapped onto the structures of free CD44 HABD (Protein Data Bank, PDB, code 1POZ; Teriete et al., 2004) and CD44 HABD in complex with hyaluronate hexamer (PDB code 2I83; Takeda et al., 2006) using the PYMOL Molecular Graphics System (Version 1.3r1 Schrodinger, LLC. 2010).

Small-angle X-ray scattering

Small-angle X-ray scattering (SAXS) data were obtained on the European Molecular Biology Laboratory P12 beamline on the PETRA III storage ring (DESY, Hamburg, Germany) with a PILATUS 2M pixel detector (DECTRIS, Baden, Switzerland). The measurements were performed with a sample-detector distance of 3.1 m and wavelength of 1.24 Å. A range of momentum transfer of $0.0028 < s < 0.45$ Å^{-1} (scattering vector $s = 4\pi \sin(\theta)/\lambda$, where 2θ is the scattering angle) was covered with this set-up. The CD44 HABD – scFv MEM-85 sample was measured at 3 different concentrations ranging from 1.3 to 5.0 mg/ml. We observed little concentration dependence; therefore, we extrapolated to zero concentration. To test for radiation damage, a 1-s exposure time was divided into 20 50-ms frames. No radiation damage was detected when the frames were compared. The collected data were processed with PRIMUS (Konarev et al., 2003) and the forward scattering *I(0)* and radius of gyration (R_g) were calculated using the Guinier approximation (Guinier, 1939). The same parameters as well as the pair-distance distribution function *P(r)* and the maximum particle dimension (D_{max}) were computed with the program GNOM (Svergun, 1992). The excluded volume of the hydrated particle (the Porod volume) was also calculated with GNOM. The molecular mass of the complex was estimated by comparison of the forward scattering of the sample to

that of a reference solution of bovine serum albumin (72 kDa). The low resolution *ab initio* models of the CD44 HABD – scFv MEM-85 complex were built using the program DAMMIN (Svergun, 1999). The algorithm employs simulated annealing to determine the shape of the macromolecule represented as densely packed beads within a sphere with diameter D_{max} by minimizing the discrepancy (χ^2) between experimental and modeled scattering curves. For the CD44 HABD – scFv MEM-85 complex, 10 initial models were calculated and then averaged with the DAMAVER (Volkov and Svergun, 2003) program. The rigid body modeling of the CD44 HABD – scFv MEM-85 complex was performed with SASREF (Petoukhov and Svergun, 2005) with specified contact conditions using the solution structure of CD44 HABD without the flexible tail residues 164-178 (PDB code 2I83; Takeda et al., 2006) and a model scFv MEM-85 created using the RosettaAntibody modeling server (Sircar et al., 2009). The final model was fitted into the *ab initio* envelope using the SUPCOMB program (Kozin and Svergun, 2001). For modeling of the full-length structure including the flexible tail (residues 164-178), CORAL software (Petoukhov and Svergun, 2005; Petoukhov et al., 2012) was used. The last 15 residues of CD44 were marked as missing for CORAL input and were reconstructed by the program as a C-alpha trace. The program combines rigid body modeling with the modeling of missing fragments (loops or termini) as a C-alpha trace and optimizes the structure by simulated annealing.

RESULTS

Protein preparation

CD44 HABD was heterologously expressed in *E. coli*, refolded from inclusion bodies (Banerji et al., 1998), and purified to homogeneity using a combination of nickel-chelation and size-exclusion chromatography with a final yield of 3 mg native monomeric CD44 HABD per 1 l cell culture. The recombinant HABD consisted of 158 amino acid residues from the native CD44 sequence (residues 21-178) and an additional short N-terminal sequence (SNAAS), which remained following cleavage of the polyhistidine affinity tag by TEV protease. The correct folding of recombinant CD44 HABD was confirmed by monitoring its hyaluronate-binding activity by NMR. In particular, ^{15}N-labeled CD44 HABD was titrated with hyaluronate, and changes in the positions of CD44 HABD backbone amide signals in two-dimensional ^{15}N/^{1}H HSQC spectra were followed. The hyaluronate-induced changes are clearly visualized in an overlay of the ^{15}N/^{1}H HSQC spectra for free ^{15}N-CD44

HABD and ^{15}N-CD44 HABD in complex with hyaluronate hexamer (Fig. A.1 in Appendix A).

The MEM-85 antibody fragment (scFv MEM-85) contained 115 N-terminal residues of the heavy chain connected to 114 N-terminal residues of the light chain by a flexible linker $(GGGGS)_4$ and was equipped with a C-terminal c-myc epitope and His_5 tag. The scFv MEM-85 protein was expressed as soluble protein in the periplasm of *E. coli* and purified to homogeneity using a combination of nickel-chelation and ion-exchange chromatography with a yield of 0.3 mg per 1 l cell culture.

We performed flow cytometry to test the binding of scFv MEM-85 to native CD44 expressed on MOLT-4 cells. The shift in the FITC fluorescence intensity of the live MOLT-4 cell population upon incubation of cells with scFv MEM-85 (Fig. 1A) confirmed the antigen-binding activity of the antibody fragment. These results were corroborated by results from fluorescence microscopy experiments. The green fluorescence of the FITC-conjugated secondary antibody, which recognizes the c-myc of scFv MEM-85 bound to CD44 on the MOLT-4 cell membrane, confirmed the antibody binding (Fig. 1B).

The kinetics of the interaction between CD44 HABD and scFv MEM-85 was assessed by surface plasmon resonance. His-tagged scFv MEM-85 was immobilized to the sensor chip and probed in parallel with serially diluted CD44 HABD. Fig. 1C shows a typical interaction kinetics characterized by the association and dissociation phases of the sensorgram. Kinetic parameters of the interaction were calculated from global fitting of the concentration-dependent binding curves. The data fitted well to a Langmuir-type binding model, indicating a simple 1:1 interaction between CD44 HABD and scFv MEM-85. The ratio between the calculated dissociation (k_d = 1.0(± 0.2)·10^{-2} s^{-1}) and association (k_a = 2.5(± 0.4)·10^4 M^{-1} s^{-1}) rate constants allowed us to determine the equilibrium dissociation constant (K_D) with a value of 430 ± 60 nM.

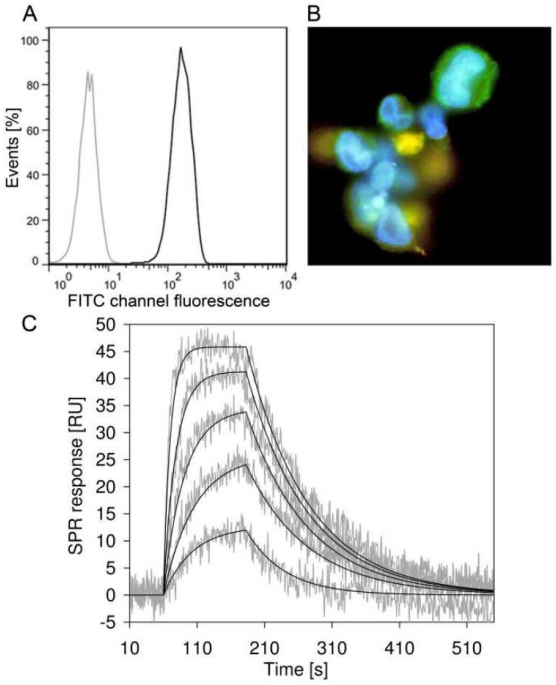

Figure 1: Binding of scFv MEM-85 to CD44

A: Flow cytometry on MOLT-4 cells incubated with the secondary anti-myc/FITC antibody only (gray) and with scFv MEM-85-myc followed by the secondary anti-myc/FITC (black). **B:** Fluorescence microscopy on MOLT-4 cells with DAPI stained nuclei (blue) incubated with scFv MEM-85-myc followed by the secondary anti-myc/FITC (green fluorescence on the cell membrane). **C:** One-shot kinetic analysis of the interaction between CD44 HABD and scFv MEM-85 is shown. His-tagged scFv MEM-85 was immobilized to the sensor chip and probed in parallel with serially diluted CD44 HABD (5.0, 2.5, 1.25, 0.625, and 0.312 μM). The experimental binding curves (gray lines) were globally fitted with a 1:1 Langmuir model and the fitted curves are superimposed as thin black lines on top of the sensorgrams.

Thermofluor assay was used to evaluate the thermal stability of scFv MEM-85 in various buffers. The antibody fragment was stable in all tested buffers, with melting temperatures ranging from 67 to 69 °C.

We prepared a stable equimolar complex of CD44 HABD and scFv MEM-85, as confirmed by analytical size-exclusion chromatography of the complex and individual binding partners (Fig. 2). The protein complex sample showed the high homogeneity and monodispersity

needed for SAXS experiments, as analyzed by dynamic light scattering at a concentration of 8.5 mg/ml (Fig. A.2 in Appendix A).

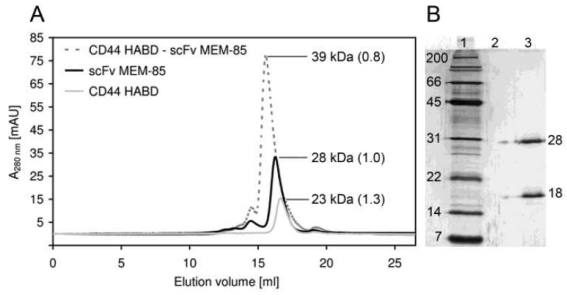

Figure 2: Recombinant CD44 HABD and scFv MEM-85 form a stable homogeneous complex.

A: Size-exclusion chromatograms for the CD44 HABD – scFv MEM-85 complex (dashed gray line), free scFv MEM-85 (black), and free CD44 HABD (gray) are shown. Apparent molecular weights are indicated for each peak with the ratios between the apparent molecular weight and the theoretical molecular weight in parentheses. **B:** SDS-PAGE analysis of size-exclusion chromatography fractions is shown. Lane 1: molecular weight standard; lane 2: empty; lane 3: CD44 HABD – scFv MEM-85 elution peak. Molecular weights in kDa are indicated.

NMR mapping of the MEM-85 epitope in CD44 HABD

We used NMR spectroscopy to identify the CD44 HABD residues involved in MEM-85 binding. Comparison of the two-dimensional $^{15}N/^{1}H$ HSQC spectra for free $^{15}N/^{13}C$-labeled CD44 HABD and a complex of $^{15}N/^{13}C$-labeled CD44 HABD with unlabeled scFv MEM-85 (Fig. 3A) revealed shifts in the positions of CD44 HABD backbone amide signals. To facilitate a detailed analysis of the antibody-induced changes in the CD44 HABD NMR spectra, we obtained essentially complete sequence-specific backbone resonance assignments for free CD44 HABD in conditions suitable for both free proteins as well as the complex. Specifically, we assigned 95% of backbone $^{1}H^{N}$, ^{15}N, $^{13}C'$, and $^{13}C\alpha/\beta$ CD44 HABD atoms based on a set of standard triple-resonance NMR experiments. Backbone amide signals were assigned for 92% of the residues, but could not be assigned for residues Tyr42, Ala98, Thr108, Asn110, Thr111, Ser112, and Cys129 due to significant line broadening within several regions, most likely caused by conformational heterogeneity on a timescale unfavorable for the used NMR experiments. We used a minimal shift approach to assess the

extent of changes in the positions of CD44 HABD backbone resonance signals (^{15}N, $^{13}C'$, and $^{1}H^{N}$) resulting from the binding of scFv MEM-85. For this analysis, residues Cys77, Asn94, Ile96, Asn100, and Ile106 were not taken into account, as they exhibited very weak backbone amide signals. The histogram of normalized combined chemical shifts against the CD44 HABD sequence in Fig. 3B indicates that the major antibody-induced changes primarily lie within the C-terminal parts of CD44 HABD; only some of the minor changes occur closer to the N-terminus. The specific C-terminal antibody-affected residues are Asp140, Thr144, Glu160, Tyr161, Thr163, and Ser171. Significantly higher normalized combined minimal shifts were also identified for residue Tyr117. Binding of scFv MEM-85 to CD44 HABD also resulted in a substantial sharpening of the signals of C-terminal CD44 HABD residues, as inferred from a comparison of the relative signal heights for residues 172-177 in the free and antibody-bound states of CD44 HABD, suggesting increased flexibility within this region upon antibody binding.

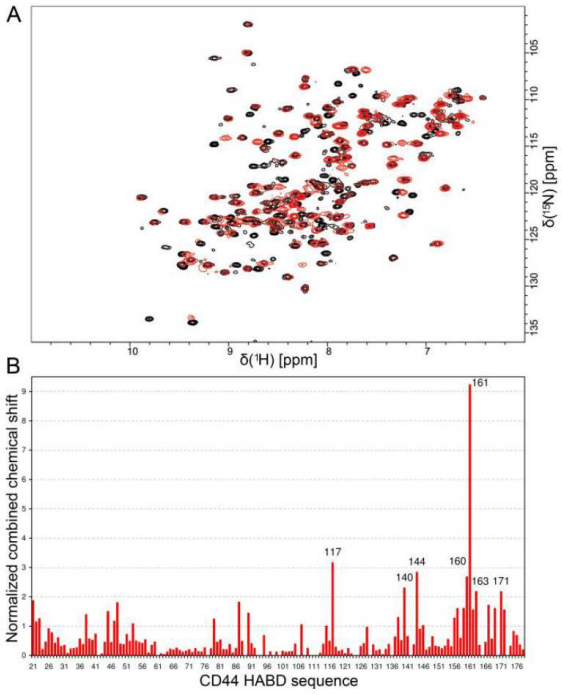

Figure 3: NMR chemical shift perturbations of CD44 HABD upon scFv MEM-85 binding **A:** Two-dimensional $^{15}N/^{1}H$ HSQC spectra are shown for free $^{15}N/^{13}C$-CD44 HABD (black) and $^{15}N/^{13}C$-CD44 HABD in complex with scFv MEM-85 (red). **B:** Histogram of minimal combined shift versus the protein sequence is shown for $^{15}N/^{13}C$-CD44 HABD. Numbers of

residues with normalized combined chemical shift values higher than 2 are indicated above the corresponding bars.

Mutational analysis

To validate the hypothesis that the MEM-85 epitope is located in the C-terminal extension lobe of CD44 HABD, we prepared CD44 HABD mutants and evaluated their affinities for MEM-85. Five CD44 HABD residues that were significantly perturbed upon MEM-85 binding (Asp140, Thr144, Glu160, Tyr161, and Thr163; Fig. 3B) were mutated to alanines. In particular, a single mutant (Y161A) and two double mutants (D140A + T144A and E160A + T163A) were constructed, and their interactions with MEM-85 were investigated using SPR. The CD44 HABD mutants were immobilized through the N-terminal His tag to the sensor chip and probed in parallel with serially diluted MEM-85 antibody. Real-time interactions of MEM-85 with CD44 HABD wt and mutant proteins are illustrated in Fig. 4. Since antibodies possess two identical epitope-binding regions on a single molecule, the kinetic data were fitted to both 1:1 Langmuir-type and bivalent analyte models. As expected, the interaction between MEM-85 and CD44 HABD proteins was significantly better described (in terms of reduced χ^2 and residual statistics) by the bivalent analyte model. The calculated association and dissociation rate constants (k_{a1}, k_{a2}, k_{d1}, and k_{d2}) as well as the apparent equilibrium dissociation constants (K_{D1}) for the bivalent binding model are listed in Table 1. The data analysis revealed that MEM-85 binds CD44 HABD with K_{D1} in the nanomolar range (K_{D1} of 4.0 ± 1.7 nM). Y161A and E160A + T163A mutants exhibited significant decrease in the binding affinity for IgG MEM-85 (K_{D1} of 32.6 ± 13.4 nM and 34.3 ± 12.8 nM, respectively). This decrease was caused by a combination of slower association and faster dissociation rates of the complex, as reflected in k_{a1} and k_{d1} rate constant values, respectively (Table 1). The binding affinity of the D140A + T144A mutant (K_{D1} of 5.4 ± 2.1 nM) was similar to that of the wt CD44 HABD.

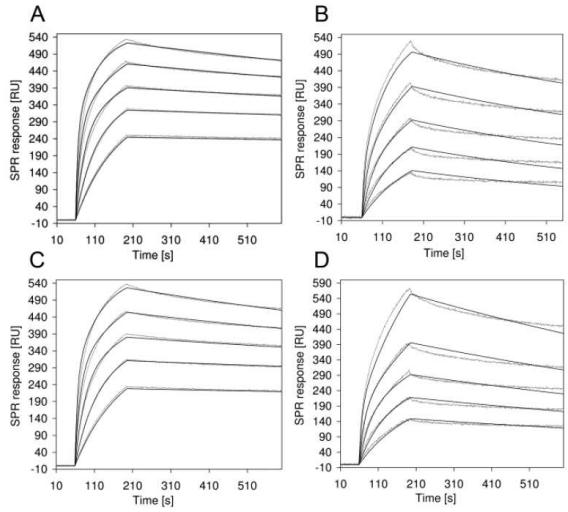

Figure 4: SPR analysis of the interaction of IgG MEM-85 with immobilized CD44 HABD mutants

One-shot kinetic analyses are shown for interactions of IgG MEM-85 with wild-type CD44 HABD **(A)**, Y161A CD44 HABD **(B)**, D140A + T144A CD44 HABD **(C)**, and E160A + T163A CD44 HABD **(D)**. His-tagged CD44 HABD was immobilized to the sensor chip and probed in parallel with serially diluted IgG MEM-85 (500, 250, 125, 62, and 31 nM) The experimental binding curves (gray lines) were globally fitted with a bivalent analyte model and the fitted curves are superimposed as thin black lines on top of the sensorgrams.

Table 1: Kinetic and binding affinity constants for the interactions between MEM-85 and CD44 HABD mutants

CD44 HABD	k_{a1} ($\cdot 10^4$) [$M^{-1}s^{-1}$]	k_{d1} ($\cdot 10^{-4}$) [s^{-1}]	K_{D1}* [nM]	k_{a2} ($\cdot 10^{-1}$) [$M^{-1}s^{-1}$]	k_{d2} ($\cdot 10^1$) [s^{-1}]
wild type	9.1 ± 3.2	3.8 ± 1.5	4.0 ± 1.7	5.5 ± 1.9	2.1 ± 0.8
Y161A	3.0 ± 1.2	9.8 ± 3.1	32.6 ± 13.4	4.1 ± 1.4	5.5 ± 2.1
D140A + T144A	8.1 ± 2.6	4.4 ± 1.6	5.4 ± 2.1	1.5 ± 0.6	7.3 ± 2.5
E160A + T163A	2.8 ± 0.9	9.7 ± 2.9	34.3 ± 12.8	3.6 ± 1.6	4.4 ± 1.9

*The apparent equilibrium dissociation constant of the complex, K_{D1}, was determined as k_{d1}/k_{a1}.

Small-angle X-ray scattering (SAXS)

A low-resolution structure of the CD44 HABD – scFv MEM-85 complex in solution was obtained using SAXS. The experimental scattering curve is shown in Fig. 5A, and overall

parameters of the complex are presented in Table 2. The molecular weight of the CD44 HABD – scFv MEM-85 complex was estimated by comparing the forward scattering intensity of the sample with that of a reference solution of bovine serum albumin. The experimentally determined molecular weight of the sample was approximately 44 kDa, which corresponds to a monomeric complex with 1:1 stoichiometry, which is in agreement with our results from analytical size-exclusion chromatography (39 kDa, Fig. 2A) and the actual molecular weight calculated from the protein sequences (46 kDa). The excluded volume of the hydrated particle (Porod volume) was $5.7 \cdot 10^4$ Å^3, and the calculated dry volume (Peptide Property Calculator web tool available at http://www.basic.northwestern.edu/biotools/proteincalc.html; Harpaz et al., 1994) was approximately the same ($5.6 \cdot 10^4$ Å^3).

We calculated the radius of gyration (R_g) directly from the scattering curve using Guinier approximation; the R_g was 26.9 Å for the CD44 HABD – scFv MEM-85 complex. The maximum dimension of the particle (D_{max}) derived from the pair-distance distribution function was 94 Å (Fig. 5B).

A low-resolution *ab initio* model of the complex was obtained by generation of 10 dummy atom structures using DAMMIN (Svergun, 1999) and subsequent generation of an average model (using DAMAVER; Volkov and Svergun, 2003) with a fixed core for another DAMMIN run. The final model obtained from this run (Fig. 5C) has an elongated shape.

Table 2: Overall parameters of the SAXS experiment

Data collection parameters	
Instrument	EMBL P12 beamline storage ring PETRA III (DESY, Hamburg)
Beam geometry [mm^2]	0.2 x 0.12
Wavelength [Å]	1.24
q-Range [Å^{-1}]	0.003 – 0.448
Exposure time [s]	1 (20 x 50 ms)
Concentration range [mg/ml]	1.3 – 5.0
Temperature [K]	298
Structural parameters	
$I(0)$ (relative) from P(r)	8,363 ± 135
R_g [Å] from $P(r)$	28.1 ± 0.5
$I(0)$ [cm^{-1}] from Guinier	8,235 ± 23
R_g [Å] from Guinier	26.9 ± 1.4
D_{max} [Å]	94 ± 10
Porod volume estimate [Å^3]	57,000 ± 200
Dry volume calculated from sequence [Å^3]	56,177

Molecular mass determination	
Molecular mass *MM* [Da] from Porod volume (V_p·0.6)	34,200
Molecular mass *MM* [Da] from forward scattering	43,750
Calculated monomeric *MM* from sequence	46,427
Software employed	
Data processing	PRIMUS
Ab initio analysis	DAMMIN, DAMAVER
Rigid-body modelling	SASREF
3D graphic representations	PYMOL

D_{max}: maximal particle dimension; *MM*: molecular mass; R_g: radius of gyration; V_p: Porod volume. The dry volume was calculated using the Peptide Property Calculator web tool available at http://www.basic.northwestern.edu/biotools/proteincalc.html (Harpaz et al., 1994).

To further illustrate the binding of scFv MEM-85 to CD44 HABD, rigid body modeling of the CD44 complex was performed with the program SASREF (Petoukhov and Svergun, 2005) using the NMR solution structure of CD44 HABD in the PD-conformation without the flexible tail residues 164-178 (PDB code 2I83; Takeda et al., 2006) and a model of scFv MEM-85 created using the RosettaAntibody modeling server (Sircar et al., 2009). In the first modeling series, six options for paratope (complementarity determining region loops L1, L2, L3, H1, H2, and H3) were specified as possible sites of interaction with the epitope (residues 160-163 of CD44 HABD). In ten modeling runs, only two heavy chain CDR loops (H2 and H3) were successfully selected for interaction with epitope. The next step of the modeling was performed with these paratopes specified in the contact conditions. Models obtained in five runs were almost identical to each other. The final model of CD44 HABD and scFv MEM-85 was superimposed with the *ab initio* envelope using the SUPCOMB program (Kozin and Svergun, 2001) (Fig. 5A and 5C). The SAXS data and the rigid body model of the CD44 HABD – scFv MEM-85 complex can be accessed in the Small Angle Scattering Biological Databank: http://www.sasbdb.org/data/SASDAG7/.

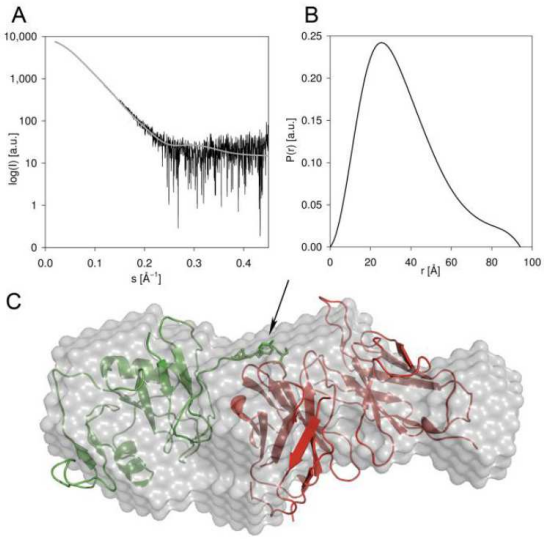

Figure 5: SAXS scattering data and rigid body model for the CD44 HABD – scFv MEM-85 complex

A: The solution scattering pattern for the CD44 HABD – scFv MEM-85 complex (black) is shown with the fit of the theoretical scattering of the rigid body model of the complex (shown in panel **C**) to the SAXS experimental data (gray), where χ^2 = 1.24. **B:** The plot of the pair-distance distribution function $P(r)$ is shown for the CD44 HABD – scFv MEM-85 complex with a maximum particle distance (D_{max}) of 94 Å. **C:** The rigid body model of the complex of CD44 HABD (green; PDB code 2I83; Takeda et al., 2006) and scFv MEM-85 model (red; Sircar et al., 2009) is shown fitted into the SAXS *ab initio* envelope. The disordered C-terminal portion of CD44 HABD (residues 164-178) is excluded from the model. The epitope is indicated with an arrow, and residues Glu160, Tyr161, and Thr163 are shown as sticks.

The theoretical scattering curve calculated for the rigid body model of the complex in which the epitope was defined as residues 160-163 of CD44 HABD exhibited a very good fit when superimposed with the *ab initio* SAXS envelope (χ^2 = 1.24; see Fig. 5 and Fig. A.3 in Appendix A). However, when this modeling was performed with the epitope defined as residues 38-42 of CD44 HABD, which had been previously identified as important for MEM-85 binding (Bajorath et al., 1998), the modeling program SASREF (Petoukhov and Svergun, 2005) could not fit the experimental scattering data with any model with a reasonably good fit (χ^2 = 2.01 for the best fit; see Fig. A.3).

Modeling of the entire structure with the flexible C-terminus of CD44 HABD (residues 164-178) was performed in CORAL (Petoukhov and Svergun, 2005; Petoukhov et al., 2012) with the same contact conditions as for the SASREF (Petoukhov and Svergun, 2005) rigid body modeling. The program was run five times to check the consistency of modeling. The resulting models only differed in the position of the flexible tail part. The rigid part of CD44 HABD in the CORAL models is only slightly rotated compared to the models created without the tail part, but the mutual orientation of the molecules remains the same. This indicates that the position of the flexible tail has no major influence on the overall structure of the complex. A representative model of full-length CD44 HABD in complex with scFv MEM-85 is shown in Fig. A.4A in Appendix A with the fit of the theoretical scattering curve of the model into the experimental SAXS data (Fig. A.4B), where $\chi^2 = 1.29$.

DISCUSSION

We constructed a recombinant scFv fragment of the monoclonal antibody MEM-85, which specifically recognizes CD44 HABD and might have therapeutic potential (Godar, S., personal communication). We successfully confirmed scFv MEM-85 binding to native, cell-surface CD44 using flow cytometry and fluorescence microscopy (Fig. 1A and 1B) and to recombinant CD44 HABD using SPR (Fig. 1C). Comparison of the affinities of IgG and scFv MEM-85 for CD44 HABD (Figs. 1C and 4, Table 1) showed that the apparent affinity of IgG MEM-85 for CD44 HABD (K_D = 4.0 ± 1.7 nM) is approximately two orders of magnitude higher than that of scFv MEM-85 (K_D = 430 ± 60 nM). This finding is in agreement with the general trend of antibody scFv fragments having lower antigen affinity than their parental immunoglobulins (Adams and Schier, 1999). The lower binding affinity of scFv MEM-85 to CD44 HABD is predominantly due to the quick dissociation kinetics of scFv MEM-85 from its complex with CD44 HABD. This suggests that avidity of MEM-85 plays a role in binding of bivalent immunoglobulin to CD44 HABD.

The scFv fragment of MEM-85 has relatively high thermal stability, as revealed by Thermofluor assay. Preparation of a highly stable, homogeneous, and monodisperse complex of scFv MEM-85 with CD44 HABD (Fig. 2 and Fig. A.2) allowed us to employ NMR and SAXS methods to characterize the CD44 HABD epitope recognized by MEM-85 in detail and analyze conformational changes in CD44 HABD induced by antibody binding.

We identified the CD44 HABD residues involved in scFv MEM-85 binding using chemical shift perturbation analysis of the backbone NMR signals (^{15}N, $^{13}C'$, and $^{1}H^{N}$) of $^{15}N/^{13}C$-

labeled CD44 HABD (Fig. 3). To interpret these perturbations and outline the antibody epitope, we used models of the three-dimensional structures of CD44 HABD and located the affected residues on their surfaces. Both conformational states of CD44 HABD, the O-conformation (Teriete et al., 2004) and the hyaluronate-bound PD-conformation (Takeda et al., 2006), were used for analysis (Fig. 6). We found that the most affected residues are situated in the extension lobe and clustered into a patch formed by the far N-terminus (β0) and, more importantly, by the C-terminal region including β8 (significantly perturbed residues Asp140 and Thr144), β9 (Glu160), the loop between β9 and α3 (Tyr161 and Thr163), and also extending into the unstructured C-terminal tail (Ser171). Another highly perturbed residue is Tyr117, which is located in β6, deeply buried in the core of CD44 HABD. Some of the minor changes occur in the vicinity of the hyaluronate-binding groove (Tyr79, Val87, Arg90, Leu107, and Asp115). For CD44 HABD topology, see Fig. 6A.

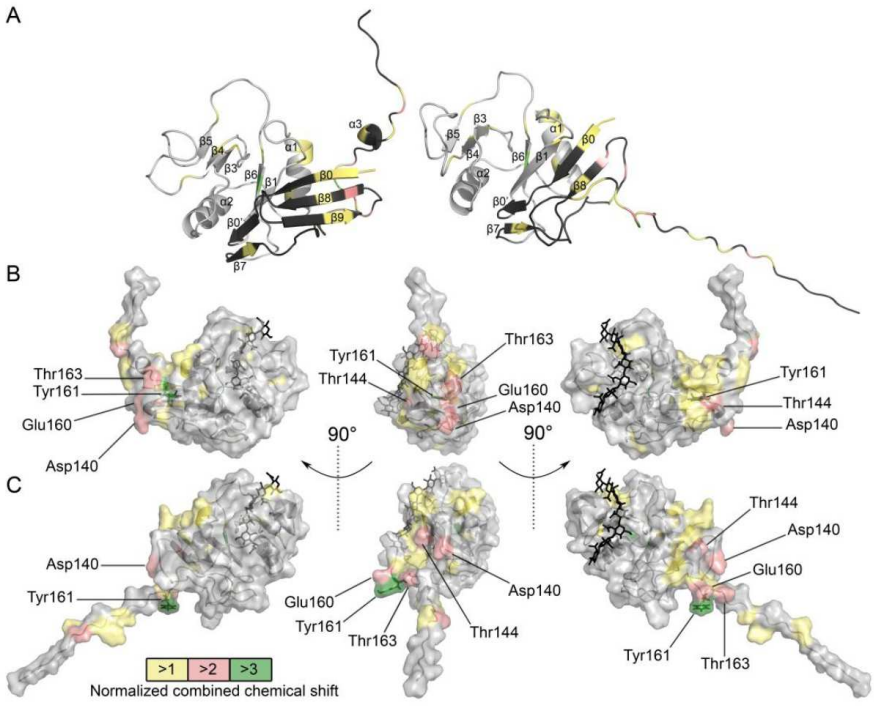

Figure 6: Mapping of the CD44 HABD epitope recognized by MEM-85.

A: Cartoon representations of CD44 HABD in the O- and PD-conformations are shown with numbered secondary structure elements. The Link module is shown in gray and the extension lobe in black. In all panels, residues with normalized combined chemical shift values higher than 1 (yellow), 2 (salmon), and 3 (green) are highlighted. **B:** Residues perturbed upon MEM-

85 binding are mapped on the surface of the free CD44 HABD structure (PDB code 1POZ; Teriete et al., 2004). **C:** Residues perturbed upon MEM-85 binding are mapped on the surface of hyaluronate-bound CD44 HABD (PDB code 2I83; Takeda et al., 2006). Tyr161 is highlighted in sticks, and residues selected for mutational analysis are indicated in panels **B** and **C**. The hyaluronate octamer bound to the crystal structure of the murine CD44 HABD – hyaluronate complex (PDB code 2JCQ; Banerji et al., 2007) is superposed onto the structures in panels **B** and **C**.

The location of the MEM-85 epitope around residues 160-163 was corroborated by our SAXS model of the CD44 HABD – scFv MEM-85 complex. The rigid body model with this epitope definition provided better fit of the theoretical scattering curve to the SAXS experimental data (χ^2 = 1.24) than the model with the epitope defined as residues 38-42 (χ^2 = 2.01; see Fig. A.3). This is also supported by the results of mutational analysis, in which mutations of Glu160, Tyr161, and Thr163 (but not Asp140 and Thr144) to alanine significantly lowered the affinity of IgG MEM-85 towards CD44 HABD (Fig. 5, Table 1).

The C-terminus of CD44 HABD undergoes major allosteric rearrangements upon hyaluronate binding (compare Fig. 6B and 6C) that mainly involve β0, β8, β9, and α3 from the extension lobe and lead to enhanced flexibility of the CD44 HABD C-terminus (Ogino et al., 2010; Takeda et al., 2006). The most important residue for transition between the O-conformation and the PD-conformation is Tyr161 (Ogino et al., 2010). We showed that Tyr161 has the highest normalized combined chemical shift upon MEM-85 binding, and we therefore suggest that similar conformational changes occur upon MEM-85 binding. Sharpening of the backbone NMR signals of CD44 HABD C-terminal residues upon antibody binding also points to a change toward a more flexible conformation in this region.

The hyaluronate-induced conformational transition into the O-state exposes the CD44 stem region, which is rendered more susceptible to proteolytic cleavage (Takeda et al., 2006), resulting in CD44 shedding from the cell surface. Interestingly, MEM-85 is also able to induce CD44 shedding (Bazil and Horejsi, 1992), and thus we might expect transition to the O-state upon MEM-85 binding. Based on our structural data, we suggest that this conformational change is triggered by direct contact of MEM-85 with the epitope surrounding Tyr161 in the extension lobe.

To explain the observation that MEM-85 interferes with hyaluronate binding (Bajorath et al., 1998; Sandmaier et al., 1998), we analyzed residues with moderate antibody-induced

perturbations. We hypothesized that primary rearrangement of the CD44 HABD C-terminus upon antibody binding is likely accompanied by an allosteric conformational change transmitted into the hyaluronate-binding groove. We observed moderate antibody-induced perturbations within the Link module in the vicinity of the hyaluronate-binding groove (residues 79, 87, 90, 107, and 115) and in the adjacent helix α1 (residues 45, 47, 48, and 53). These perturbations, however, are relatively small to be caused by direct contact with the antigen-binding loops of the antibody. Direct contacts of CD44 HABD residues with the complementarity determining regions of MEM-85, which contain a total of 11 aromatic residues (Kabat et al., 1991), would result in larger changes in the CD44 HABD spectra (Addis et al., 2014; Wilkinson et al., 2009). Additionally, one of the most greatly perturbed residues, Tyr117, lies deep in the core of the HABD domain in β6, which connects the hyaluronate-binding "subdomain" and the C-terminal "subdomain" and might be one of the key residues for transmission of the conformational change into the hyaluronate-binding groove area. Therefore, the mechanism of MEM-85 cross-blocking of hyaluronate binding (Bajorath et al., 1998; Sandmaier et al., 1998) might be of an allosteric, relay-like nature, rather than physical competition for the hyaluronate-binding site.

Residues Lys38, Arg41, and Tyr42, which had been previously identified by mutational analysis to be important for MEM-85 binding (Bajorath et al., 1998), exhibited low to moderate normalized combined chemical shifts (Tyr42 was not assigned). They are located in a patch stretching from the MEM-85 epitope toward the hyaluronate-binding groove, and they are very likely to play a role in the antibody-induced conformational change.

CONCLUSIONS

The work presented here led to an unambiguous determination of the MEM-85 binding epitope in CD44 HABD using a combination of NMR and SAXS techniques and suggested the mechanism of antibody interference with the biological function of CD44. Strikingly, MEM-85 does not directly compete with the binding of hyaluronate, but acts through an allosteric, relay-like mechanism. In particular, it binds to the C-terminal extension lobe region of CD44 HABD and induces a conformational rearrangement which is further propagated into the hyaluronate-binding groove. Antibody MEM-85 triggers a structural transition of CD44 from "ordered" into "partially disordered" state, similar to the one observed upon hyaluronate binding, leading to CD44 shedding from the cell surface.

Acknowledgments

J.S. thanks Petr Těšina for his help with the NMR sequence-specific resonance assignment. This work was supported by Charles University in Prague, project GA UK No. 567012. This work was also supported in part by projects RVO 61388963 and 68378050 awarded by the Academy of Sciences of the Czech Republic and by the Ministry of Education of the Czech Republic, projects LK11205 (program 'NAVRAT') and LO1304 (program 'NPU I'), and project GACR 15-11851S awarded by The Grant Agency of the Czech Republic. M.K. acknowledges support from the European Commission (the 7th Framework Programme) Marie Curie grant IDPbyNMR (contract No 264257).

Conflict of interest disclosure statement and role of the funding source

We wish to confirm that there are no conflicts of interest associated with this publication. The funding sources had no role in the study design, data collection, analysis, and interpretation, in the writing of the report, or in the decission to submit the manuscript for publication.

References

Adams, G.P., Schier, R., 1999. Generating improved single-chain Fv molecules for tumor targeting. J. Immunol. Methods 231, 249-260.

Addis, P.W., Hall, C.J., Bruton, S., Veverka, V., Wilkinson, I.C., Muskett, F.W., Renshaw, P.S., Prosser, C.E., Carrington, B., Lawson, A.D., Griffin, R., Taylor, R.J., Waters, L.C., Henry, A.J., Carr, M.D., 2014. Conformational Heterogeneity in Antibody-Protein Antigen Recognition: Implications for High Affinity Protein Complex Formation. J. Biol. Chem. 289, 7200-7210.

Anstee, D.J., Gardner, B., Spring, F.A., Holmes, C.H., Simpson, K.L., Parsons, S.F., Mallinson, G., Yousaf, S.M., Judson, P.A., 1991. New monoclonal antibodies in CD44 and CD58: their use to quantify CD44 and CD58 on normal human erythrocytes and to compare the distribution of CD44 and CD58 in human tissues. Immunology 74, 197-205.

Aruffo, A., Stamenkovic, I., Melnick, M., Underhill, C.B., Seed, B., 1990. CD44 is the principal cell surface receptor for hyaluronate. Cell 61, 1303-1313.

Bajorath, J., Greenfield, B., Munro, S.B., Day, A.J., Aruffo, A., 1998. Identification of CD44 residues important for hyaluronan binding and delineation of the binding site. J. Biol. Chem. 273, 338-343.

Banerji, S., Day, A.J., Kahmann, J.D., Jackson, D.G., 1998. Characterization of a functional hyaluronan-binding domain from the human CD44 molecule expressed in Escherichia coli. Protein Expression Purif. 14, 371-381.

Banerji, S., Wright, A.J., Noble, M., Mahoney, D.J., Campbell, I.D., Day, A.J., Jackson, D.G., 2007. Structures of the Cd44-hyaluronan complex provide insight into a fundamental carbohydrate-protein interaction. Nat. Struct. Mol. Biol. 14, 234-239.

Bazil, V., Horejsi, V., 1992. Shedding of the CD44 adhesion molecule from leukocytes induced by anti-CD44 monoclonal antibody simulating the effect of a natural receptor ligand. J. Immunol. 149, 747-753.

Bazil, V., Stefanova, I., Hilgert, I., Kristofova, H., Vanek, S., Bukovsky, A., Horejsi, V., 1989. Monoclonal antibodies against human leucocyte antigens. III. Antibodies against CD45R, CD6, CD44 and two newly described broadly expressed glycoproteins MEM-53 and MEM-102. Folia biologica (Prague, Czech Republic) 35, 289-297.

Cheng, X., Veverka, V., Radhakrishnan, A., Waters, L.C., Muskett, F.W., Morgan, S.H., Huo, J., Yu, C., Evans, E.J., Leslie, A.J., Griffiths, M., Stubberfield, C., Griffin, R., Henry, A.J., Jansson, A., Ladbury, J.E., Ikemizu, S., Carr, M.D., Davis, S.J., 2013. Structure and interactions of the human programmed cell death 1 receptor. J. Biol. Chem. 288, 11771-11785.

Cichy, J., Pure, E., 2003. The liberation of CD44. J. Cell Biol. 161, 839-843.

Day, A.J., Prestwich, G.D., 2002. Hyaluronan-binding proteins: tying up the giant. J. Biol. Chem. 277, 4585-4588.

DeGrendele, H.C., Estess, P., Picker, L.J., Siegelman, M.H., 1996. CD44 and its ligand hyaluronate mediate rolling under physiologic flow: a novel lymphocyte-endothelial cell primary adhesion pathway. J. Exp. Med. 183, 1119-1130.

Ericsson, U.B., Hallberg, B.M., Detitta, G.T., Dekker, N., Nordlund, P., 2006. Thermofluor-based high-throughput stability optimization of proteins for structural studies. Anal. Biochem. 357, 289-298.

Guinier, A., 1939. La diffraction des rayons X aux tres petits angles; application a l'etude de phenomenes ultramicroscopiques. Annales de Physique (Paris, France) 12, 161-237.

Harpaz, Y., Gerstein, M., Chothia, C., 1994. Volume changes on protein folding. Structure 2, 641-649.

Kabat, E.A., Wu, T.T., Perry, H.M., Gottesman, K.S., Foeller, C., 1991. Sequences of Proteins of Immunological Interest, fifth ed. Department of Health and Human Services, National Institute of Health, Bethesda.

Konarev, P.V., Volkov, V.V., Sokolova, A.V., Koch, M.H.J., Svergun, D.I., 2003. PRIMUS - a Windows-PC based system for small-angle scattering data analysis. J. Appl. Crystallogr. 36, 1277-1282.

Kozin, M.B., Svergun, D.I., 2001. Automated matching of high- and low-resolution structural models. J. Appl. Crystallogr. 34, 33-41.

Laemmli, U.K., 1970. Cleavage of structural proteins during the assembly of the head of bacteriophage T4. Nature 227, 680-685.

Nagano, O., Saya, H., 2004. Mechanism and biological significance of CD44 cleavage. Cancer Sci. 95, 930-935.

Naor, D., Sionov, R.V., Ish-Shalom, D., 1997. CD44: structure, function, and association with the malignant process. Adv. Cancer Res. 71, 241-319.

Ogino, S., Nishida, N., Umemoto, R., Suzuki, M., Takeda, M., Terasawa, H., Kitayama, J., Matsumoto, M., Hayasaka, H., Miyasaka, M., Shimada, I., 2010. Two-state conformations in the hyaluronan-binding domain regulate CD44 adhesiveness under flow condition. Structure 18, 649-656.

Okamoto, I., Kawano, Y., Tsuiki, H., Sasaki, J., Nakao, M., Matsumoto, M., Suga, M., Ando, M., Nakajima, M., Saya, H., 1999. CD44 cleavage induced by a membrane-associated metalloprotease plays a critical role in tumor cell migration. Oncogene 18, 1435-1446.

Peach, R.J., Hollenbaugh, D., Stamenkovic, I., Aruffo, A., 1993. Identification of hyaluronic acid binding sites in the extracellular domain of CD44. J. Cell Biol. 122, 257-264.

Petoukhov, M.V., Svergun, D.I., 2005. Global rigid body modeling of macromolecular complexes against small-angle scattering data. Biophys. J. 89, 1237-1250.

Petoukhov, M.V., Franke, D., Shkumatov, A.V., Tria, G., Kikhney, A.G., Gajda, M., Gorba, C., Mertens, H.D., Konarev, P.V., Svergun, D.I., 2012. New developments in the program package for small-angle scattering data analysis. J. Appl. Crystallogr. 45, 342-350.

Pisackova, J., Prochazkova, K., Fabry, M., Rezacova, P., 2013. Crystallization of the Effector-Binding Domain of Repressor DeoR from Bacillus subtilis. Cryst. Growth Des. 13, 844-848.

Ponta, H., Sherman, L., Herrlich, P.A., 2003. CD44: from adhesion molecules to signalling regulators. Nat. Rev. Mol. Cell Biol. 4, 33-45.

Prochazkova, K., Cermakova, K., Pachl, P., Sieglova, I., Fabry, M., Otwinowski, Z., Rezacova, P., 2012. Structure of the effector-binding domain of the arabinose repressor AraR from Bacillus subtilis. Acta Crystallogr., Sect. D: Biol. Crystallogr. 68, 176-185.

Renshaw, P.S., Veverka, V., Kelly, G., Frenkiel, T.A., Williamson, R.A., Gordon, S.V., Hewinson, R.G., Carr, M.D., 2004. Sequence-specific assignment and secondary structure determination of the 195-residue complex formed by the Mycobacterium tuberculosis proteins CFP-10 and ESAT-6. J. Biomol. NMR 30, 225-226.

Sandmaier, B.M., Storb, R., Bennett, K.L., Appelbaum, F.R., Santos, E.B., 1998. Epitope specificity of CD44 for monoclonal antibody-dependent facilitation of marrow engraftment in a canine model. Blood 91, 3494-3502.

Sircar, A., Kim, E.T., Gray, J.J., 2009. RosettaAntibody: antibody variable region homology modeling server. Nucleic Acids Res. 37, W474-479.

Skerlova, J., Kral, V., Fabry, M., Sedlacek, J., Veverka, V., Rezacova, P., 2014. Optimization of the crystallizability of a single-chain antibody fragment. Acta Crystallogr., Sect. F: Struct. Biol. Cryst. Commun. 70, 1701-1706.

Stefanova, I., Hilgert, I., Bazil, V., Kristofova, H., Horejsi, V., 1989. Human leucocyte surface glycoprotein CDw44 and lymphocyte homing receptor are identical molecules. Immunogenetics 29, 402-404.

Stols, L., Gu, M.Y., Dieckman, L., Raffen, R., Collart, F.R., Donnelly, M.I., 2002. A new vector for high-throughput, ligation-independent cloning encoding a tobacco etch virus protease cleavage site. Protein Expression Purif. 25, 8-15.

Svergun, D.I., 1992. Determination of the regularization parameter in indirect-transform methods using perceptual criteria. J. Appl. Crystallogr. 25, 495-503.

Svergun, D.I., 1999. Restoring low resolution structure of biological macromolecules from solution scattering using simulated annealing. Biophys. J. 76, 2879-2886.

Takeda, M., Ogino, S., Umemoto, R., Sakakura, M., Kajiwara, M., Sugahara, K.N., Hayasaka, H., Miyasaka, M., Terasawa, H., Shimada, I., 2006. Ligand-induced structural changes of the CD44 hyaluronan-binding domain revealed by NMR. J. Biol. Chem. 281, 40089-40095.

Teriete, P., Banerji, S., Noble, M., Blundell, C.D., Wright, A.J., Pickford, A.R., Lowe, E., Mahoney, D.J., Tammi, M.I., Kahmann, J.D., Campbell, I.D., Day, A.J., Jackson, D.G., 2004. Structure of the regulatory hyaluronan binding domain in the inflammatory leukocyte homing receptor CD44. Mol. Cell 13, 483-496.

Veverka, V., Lennie, G., Crabbe, T., Bird, I., Taylor, R.J., Carr, M.D., 2006. NMR assignment of the mTOR domain responsible for rapamycin binding. J Biomol Nmr 36, 3.

Volkov, V.V., Svergun, D.I., 2003. Uniqueness of ab initio shape determination in small angle scattering. J. Appl. Crystallogr. 36, 860-864.

Wilkinson, I.C., Hall, C.J., Veverka, V., Shi, J.Y., Muskett, F.W., Stephens, P.E., Taylor, R.J., Henry, A.J., Carr, M.D., 2009. High Resolution NMR-based Model for the Structure of a scFv-IL-1 beta Complex: Potential for NMR as a Key Tool in Therapeutic Antibody Design and Development. J. Biol. Chem. 284, 31928-31935.

Supplementary material

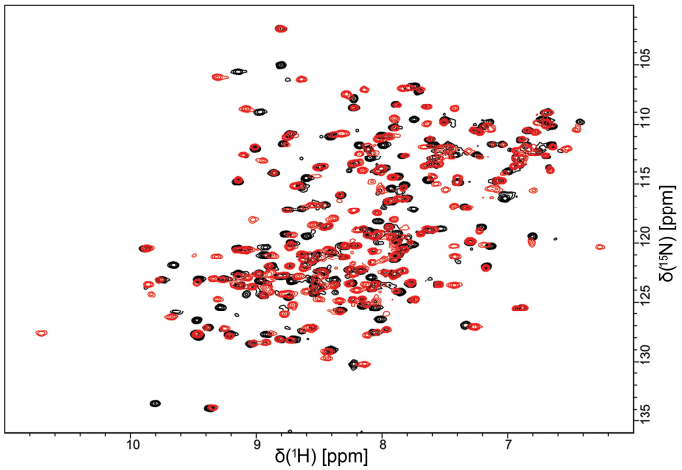

Figure A.1: Binding of hyaluronate hexamer to CD44 HABD

Two-dimensional $^{15}N/^{1}H$ HSQC spectra are shown for free ^{15}N-CD44 HABD (black) and ^{15}N-CD44 HABD in complex with hyaluronate hexamer (red).

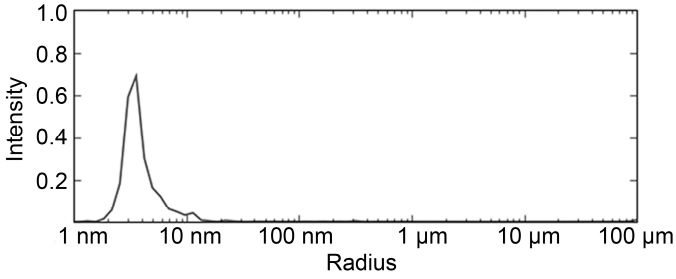

Figure A.2: The CD44 HABD – scFv MEM-85 complex is monodisperse.

Mean particle size distribution determined by dynamic light scattering indicates monodispersity of the complex at a concentration of 8.5 mg/ml.

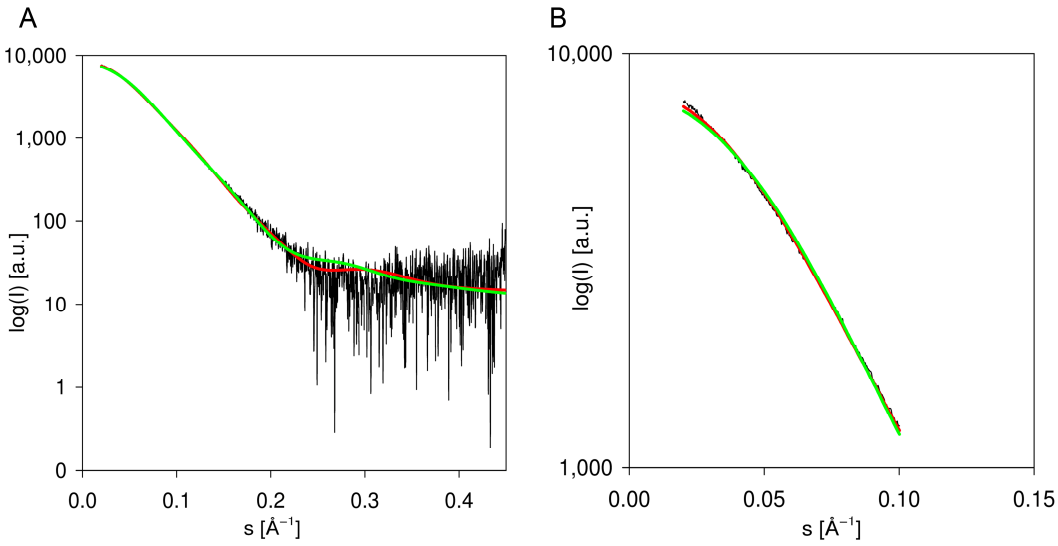

Figure A.3: Rigid body model fit to SAXS data

A: Fit of the theoretical scattering of the rigid body model of the CD44 HABD – scFv MEM-85 complex to SAXS experimental data (black) is shown for epitope residues 160-163 (red), where χ^2 = 1.24, and for epitope residues 38-42 (green), where χ^2 = 2.01. **B:** The enlarged section of the curves in panel **A** is shown at low scattering vector values (*s*).

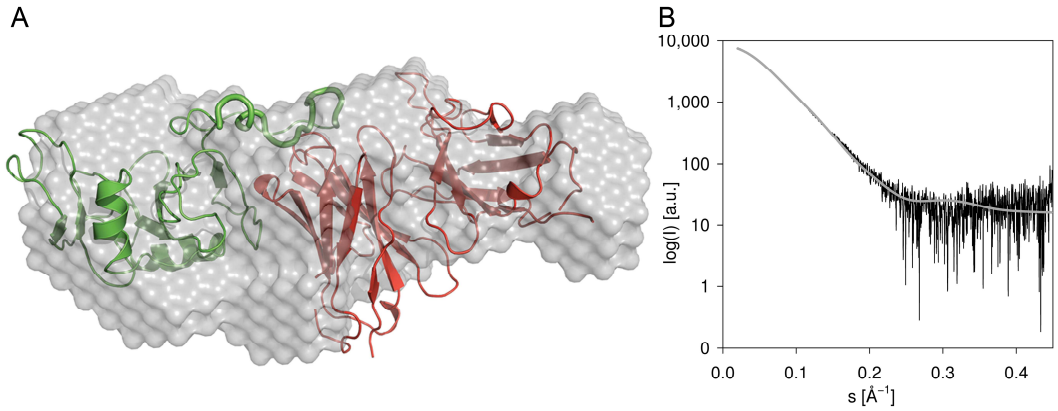

Figure A.4: CD44 HABD and scFv MEM-85 SAXS model with flexible tail

A: The CORAL model of the complex of CD44 HABD (green; PDB code 2I83) (5) and scFv MEM-85 model (6) (red) is shown fitted into the SAXS *ab initio* envelope. The disordered C-terminal portion of CD44 HABD (residues 164-178) is modeled as a C-alpha trace (shown in bold). **B:** Fit of the theoretical scattering of the CORAL model of the CD44 HABD – scFv MEM-85 complex to the SAXS experimental data (black), where χ^2 = 1.29 is shown in gray.

8 Discussion

8.1 Structural studies of deoxyribonucleoside regulator form *Bacillus subtilis*

Structural data on several key transcriptional regulators from *B. subtilis* obtained so far indicate that although the effector-binding domains of the repressors represent conserved folds typical for individual protein families, each of them exhibits a unique mode of action determined by specific effector-induced structural changes and oligomerization pattern. Therefore, structural studies of several members of the *B. subtilis* families of transcriptional regulators are necessary for the full understanding of the distinct molecular mechanisms of carbon catabolite repression in Gram-positive bacteria and also gene regulation in general. In this part of the work, we focused on X-ray crystallographic analysis of the C-terminal effector-binding domain of deoxyribonucleoside regulator DeoR from *B. subtilis*.

Crystals suitable for X-ray diffraction analysis were obtained by elaborate optimization of crystallization conditions. First crystallization trials with recombinant C-DeoR expressed in *E.coli* yielded thin needle-shaped crystals in 8 out of 96 screened crystallization conditions. Despite the extensive effort to optimize the initial crystallization conditions, only rod-shaped crystals of poor diffraction quality were obtained. Therefore, we employed the Thermofluor-based optimization of the protein storage buffer to achieve maximal protein stability. This assay revealed protein thermal stabilization by phosphate ions, but these buffers were not taken into account for the crystallization, as binding of phosphate was shown before for other bacterial transcription factors [15, 16]. The Thermofluor assay also identified a combined stabilizing effect of citrate buffer and the pH value of around 7.5. A combination of these two conditions was used in the optimized protein storage buffer (based on tri-sodium citrate pH 7.0) for new crystallization screening trials both in the presence and absence of the effector (dexyribose-5-phospate). These trials yielded crystals in 8 out of 96 conditions for the effector-bound protein, which were different from those for the original protein storage buffer. The free C-DeoR protein in the optimized storage buffer yielded crystals in 31 out of 96 screened conditions. Most of the crystals were again represented by needle or plate clusters, but new crystal forms were

obtained for both the free and effector-bound C-DeoR, which were three-dimensional monocrystals. These results proved that the Thermofluor-based buffer optimization technique generally used in order to improve protein stability, and therefore its crystallizability can be used to obtain new, better diffracting crystal forms of otherwise well crystallizing protein.

The new crystal forms of C-DeoR were easily optimized to large well-diffracting monocrystals suitable for X-ray diffraction experiments. Three complete data sets were acquired for the free C-DeoR (space group $P3_2$ or $P3_1$, resolution 1.90 Å) and for the effector-bound C-DeoR (space group $C222_1$, resolution 1.60 Å, and space group $P222_1$, resolution 1.65 Å). The sequence similarity of C-DeoR with the homologous transcriptional regulators with known three-dimensional structures suggested that C-DeoR crystal structures can be solved using the molecular replacement method. The putative sugar-binding transcriptional regulator from *Arthrobacter aurescens* (PDB code 3NZE) shows 52% sequence similarity and 30% sequence identity with 259 DeoR residues, the probable sorbitol operon regulator from *Shigella flexneri* (PDB code 3EFB) shows 49% sequence similarity and 31% sequence identity with 265 DeoR residues, and the sorbitol operon regulator SorC from *Klebsiella pneumoniae* (PDB code 2W48) shows 50% sequence similarity and 30% sequence identity for 246 DeoR residues [152].

The next step in this project was the determination of the C-DeoR structures. The structure of effector-bound C-DeoR was determined at resolution of 1.60 Å by molecular replacement using the homologous putative sugar-binding transcriptional regulator from *Arthrobacter aurescens* (PDB code 3NZE) as the search model. The refined effector-bound C-DeoR structure was then used as a molecular replacement search model for the determination of the unliganded C-DeoR structure using a dataset acquired at 1.80 Å resolution.

The C-DeoR structure is composed of a central double-Rossmann-fold core, typical for dinucleotide-binding proteins [153], which is supplemented on both sides with a total of 5 α-helices, resulting in an overall α/β fold of the core subdomain. Additionally, the C-DeoR is equipped with three, mostly helical peripheral subdomains, which take part in effector binding and repressor oligomerization. The effector-binding site, formed by the interface of the core subdomain and two peripheral subdomains, binds the effector molecule deoxyribonuceloside-5-phosphate in a linear form, through a reversible Schiff-base double bond with residue Lys141 located in one of the peripheral subdomains.

The phosphate moiety of the effector molecule interracts with the N-terminal end of one of the Rossmann fold α-helices, an interaction motif typical for dinucleotide-binding Rossmann-fold proteins [153-155].

C-DeoR shows structural homology [156] to numerous prokaryotic transcriptional regulators from the SorC family. C-DeoR is also homologous to central glycolytic genes regulator CggR from *B. subtilis* (PDB code 3BXF [15]), which exhibits a very similar organization of the effector-binding site and also binds its ligands in a very similar pose to that of C-DeoR. Moreover, C-DeoR structure is homologous to many enzymes involved in prokaryotic sugar metabolism, such as 6-phosphogluconolactonase, glucose-6-phosphate-1-dehydrogenase and glucosamine-6-phosphate deaminase. This indicates that one common protein fold can be adapted to performing various enzymatic and regulatory functions. One such enzyme, ribose-5-phosphate isomerase A from *Burkholderia thailandensis* (PDB code 3UW1 [157]) also binds its substrate ribose-5-phospate in a linear form in an orientation very similar to that of deoxyribose-5-phosphate in C-DeoR. The Schiff base, however, cannot be formed here, as ribose-5-phosphate isomerase A contains a serine residue instead of the lysine in the active site. The Schiff-base adduct of deoxyribose-5-phosphate has been observed also in the structure of deoxyribose-5-phosphate aldolase form *E. coli*, where it represents a reaction intermediate (PDB code 1JCJ [158]). The length of the imine bond in the aldolase structure is 1.29 Å and the Nζ-C-C angle is 125°, which are identical values to those in the C-DeoR structure.

Our effector-bound C-DeoR structure is the only crystal structure of a transcriptional factor capturing a covalently bound effector molecule. The physiological nature of the covalent bond was confirmed by the mass spectrometry analysis of the Schiff-base products formed in solution under physiological concentrations of deoxyribose-5-phosphate [159]. The mass to charge ratio difference between the two detected MALDI-TOF peaks corresponding to free C-DeoR and the C-DeoR Schiff-base adduct was equal to the mass of the cyanoborohydride-reduced deoxyribose-5-phosphate adduct, 3,4-dihydroxy-5-(phosphonooxy)pentyl residue. Moreover, the abundance of the higher molecular mass peak increased with the incubation time. Mutational analysis combined with the Thermofluor-based differential scanning fluorimetry assay [160-162] confirmed the key role of Lys141 in effector binding. The titration of Lys141-mutant proteins K141N, K141Q, K141R, or K141A, respectively, by deoxyribose-5-phosphate showed only small increase in the thermal stability of the mutant proteins when compared

to the thermal stabilization of the wild-type C-DeoR. This suggests that Lys141 is essential for proper effector binding.

The superposition of the Cα atoms of the free and effector-bound C-DeoR structures identified the location and the extent of the effector-induced structural changes. Major changes occur around the effector-binding site and in the adjacent peripheral subdomains, and are in some extent similar to those observed in CggR [15]. The structural changes in the parts of peripheral subdomains that are involved in the dimeric interface might affect the protein's oligomeric state as they disrupt the dimer interface and reduce the interface area from 1367.3 $Å^2$ formed by 40 interacting residues in the free C-DeoR dimer to 841.3 $Å^2$ formed by 25 interacting residues in the effector-bound C-DeoR dimer. The interface is formed by a peripheral subdomain of C-DeoR and also in part by a portion of the double-Rossmann-fold core, in a manner similar to dimers of other members of the SorC family, such as CggR [15], putative sugar-binding transcriptional regulator from *A. aurescens* (PDB code 3NZE), and SorC [152]. The size-exclusion and dynamic light scattering experiments with the C-DeoR and full-length DeoR both in the presence and absence of deoxyribose-5-phosphate have shown that C-DeoR and full-length DeoR persist in the dimeric and tetrameric forms, respectively, even upon effector-binding. This suggests the presence of two dimerization interfaces in the full-length DeoR: one in the effector-binding domain, and the second in the DNA-binding domain. We suggested a model for the regulation of DeoR function: the tight tetramer of DeoR binds to a palindromic operator sequence [20, 25], but in the presence of deoxyribose-5-phosphate, the effector-induced structural change in the effector-binding domains disrupts the dimerization interfaces in both the effector- and allosterically also in the DNA-binding domains and the less tight tetramer can be easily displaced from the operator by RNA polymerase. The exact structural mechanism, however, still remains to be unraveled by the determination of the full-length DeoR structures, ideally in complex with the operator DNA.

8.2 Epitope mapping for the anti-CD44 monoclonal antibody MEM-85

Monoclonal antibodies are molecules with immense therapeutic and diagnostic potential. The same applies to their single-chain variable fragments (scFv), the smallest antibody fragments that retain the antigen-binding properties while having a relatively small size which makes them excellent molecular biology tools for the characterization of

antigen binding. The only drawback that might compromise their use for some applications is their spontaneous oligomerization. This issue might be, however, resolved by some optimization approaches, as described in the first part of this section on a model case of the scFv fragment of the anti-CD3 antibody MEM-57. The second part of this project is focused on antibody MEM-85, which is one of the therapeutically applicable antibodies targeted against the CD44 antigen. CD44 has been recently identified to be involved in many aspects of cancer and in the last few years, novel CD44-targeted immunotherapeutic approaches keep emerging and seem to be very promising. Antibody MEM-85 has been widely used as a molecular biology tool, but its epitope has not been unambiguously described so far, which was the goal of this project.

We constructed an scFv fragment of antibody MEM-57 for recombinant expression in *E. coli*. The variable domains of the heavy and light chains were connected via a $(Gly_4Ser)_4$ linker sequence. A longer version of the conventional $(Gly_4Ser)_3$ linker [163] was used here, which should reduce the spontaneous oligomerization of scFv fragments, observed typically for shorter linker sequences [164-168]. Size-exclusion analysis of the purified scFv revealed equilibrium between scFv monomeric and oligomeric forms, where the monomer represented only 65% of the total scFv. This equilibrium re-establish even after the separation of scFv monomers and dimers using ion-exchange chromatography. This oligomerization reduced the effective protein yield, but, more importantly, presented a disadvantage in the use of the scFv fragments for experiments that require high protein homogeneity.

The oligomeric equilibrium is not only a function of the linker sequence length, but it also depends on other aspects such as protein concentration and the pH and ionic strength of the protein storage buffer [169]. In order to resolve the oligomerization issue, we employed the Thermofluor assay to screen for conditions that would preferentially stabilize scFv monomers, and thus reduce the oligomeric heterogeneity of the protein sample. The Thermofluor-based thermal denaturation curve for a homogeneous protein has a typical shape containing only one inflection point which indicates the melting temperature point (T_m). Therefore, multi-inflection curves were excluded from the T_m analysis and the buffer which provided scFv denaturation curve with one inflection point and the highest T_m was selected as the optimal protein storage buffer for further experiments. Size-exclusion analysis and dynamic light scattering confirmed scFv homogeneity in the optimized protein storage buffer (the monomer represented 88% of the total protein). Our results

suggested that Thermofluor assay nowadays routinely used for protein stability optimization [162, 170] can be of help also in the efforts to resolve the undesirable oligomerization issue of scFv fragments in general, including for example the anti-CD44 scFv MEM-85 studied in the following part of this project.

For the anti-CD44 antibody MEM-85, we have constructed a recombinant scFv fragment in which the variable domains of the heavy and light chains were connected via a $(Gly_4Ser)_4$ linker sequence, similarly to MEM-57. The recombinant scFv MEM-85 was able to bind native CD44 on the surface of CD44-positive cells as confirmed by flow cytometry and fluorescence microscopy, and it also bound recombinant hyaluronate-binding domain (HABD) of CD44 as confirmed by surface plasmon resonance (SPR). SPR analysis of the binding affinities of scFv MEM-85 and IgG MEM-85 revealed lower binding affinity of scFv MEM-85 (K_D = 430 ± 60 nM) when compared to IgG MEM-85 (K_D = 4.0 ± 1.7 nM), which is in concordance with a generally observed trend [171]. Preparation of a highly stable and homogeneous scFv sample (employing the Thermofluor assay optimization) and a sample of the CD44 HABD – scFv MEM-85 complex (employing size-exclusion chromatography and dynamic light scattering) was necessary for the further NMR and SAXS experiments aimed at the characterization of MEM-85 epitope and the antibody-induced conformational changes in CD44 HABD. The MEM-85 epitope residues in CD44 HABD were identified by using the chemical shift perturbation method on the backbone NMR signals, acquired in the sets of three-dimensional experiments performed on the free $^{15}N/^{13}C$-labeled CD44 HABD and on the complex of the $^{15}N/^{13}C$-labeled CD44 HABD with scFv MEM-85. Locating the significantly perturbed residues on the surfaces of the available three-dimensional structures of CD44 HABD (unliganded O-conformation [62] and the hyaluronate-bound PD-conformation [64]) revealed that the epitope is located in the C-terminal part of the HABD extension lobe, clustered around the most perturbed residues 160-163. The role of these residues in antibody binding was confirmed by mutational analysis combined with SPR: mutations of residues 160, 161, and 163 to alanines significantly reduced MEM-85 affinity towards CD44 HABD. These data were also corroborated with the rigid body model of the CD44 HABD – scFv MEM-85 complex, that was created based on the low-resolution structure of the complex obtained by small-angle X-ray scattering (SAXS). The rigid body model with the epitope defined as residues 160-163 provided a perfect fit to

the experimental data, unlike the epitope defined as residues 38-42, based on the previous mutational experiments performed by Bajorath *et al.* [33].

The major conformational changes, that occur in the C-terminus of CD44 HABD upon hyaluronate binding [64, 70] provide enhanced flexibility to the unstructured HABD tail and induce CD44 proteolytic shedding [64]. The key residue for this rearrangement is Tyr161 [70], which is also the residue exhibiting the highest normalized combined chemical shift in our NMR experiments. This suggests that the binding of MEM-85 triggers a similar conformational change in HABD from the O- to the PD-conformation, which is also in agreement with our observation of sharpening of the NMR signals for the very C-terminal HABD residues in the antibody-bound state. Moreover, MEM-85 has also been shown to induce CD44 shedding similar to that induced by hyaluronate [151].

Taken together, our results propose that MEM-85 recognizes an epitope located in the C-terminal part of CD44 HABD, including residues 160-163, and that the antibody binding induces conformational changes in the C-terminal region by a direct contact with residues around Tyr161. MEM-85 competes with hyaluronate for binding to CD44 HABD [33, 150]. This could be explained by our finding that some of the residues that exhibit moderate antibody-induced chemical shift perturbations (including residues 38-42) are located in the vicinity of the hyaluronate-binding groove. These perturbations are too small to be caused by a direct binding of the antibody [172, 173] but rather suggest a secondary allosteric rearrangement triggered by antibody-induced conformational change in the C-terminal portion of HABD. This conformational change may be transmitted through residues 38-42 that are clustered in a linear patch reaching from residue Tyr161 towards the hyaluronate-binding groove. Therefore, MEM-85 does not directly compete with hyaluronate binding, but acts through an allosteric, relay-like mechanism.

9 Conclusions

This work combines principal techniques that are used to study protein-protein and protein-ligand interactions and the changes in protein conformation. X-ray crystallographic analysis was used to study the structure of deoxyribonucleoside regulator DeoR from *Bacillus subtilis* to understand the binding of an effector molecule. NMR-based mapping of the interaction interface was used to identify the location of the antigen-binding epitope of monoclonal antibody MEM-85 in the hyaluronate-binding domain of human CD44.

The first part of this work describes an important contribution to the field of bacterial transcription regulation. We have crystallized the C-terminal effector-binding domain of deoxyribonucleoside regulator DeoR from *Bacillus subtilis* (C-DeoR). The new crystal form of C-DeoR, optimal for X-ray diffraction experiments, was obtained based on an extensive biophysical characterization of the C-DeoR protein together with protein buffer optimization using Thermofluor assay. The crystal structure of DeoR in complex with the effector molecule deoxyribose-5-phosphate revealed that DeoR binds the effector molecule deoxyribose-5-phosphate covalently via a Schiff-base double bond with a lysine residue in the effector-binding site. The formation of the Schiff-base adduct was also observed in solution at low effector concentrations and the key role of the effector-binding-site lysine residue was confirmed by mutational analysis. These findings make DeoR the first case of transcriptional regulator that binds its small-molecular ligand through a reversible covalent bond. Structural analysis of both C-DeoR in the free form and in complex with the effector revealed effector-induced structural changes disturbing the dimeric interface in C-DeoR. These structural data allowed us to create a model describing the molecular mechanism of the DeoR function as a molecular switch.

In the second part of this work, we have constructed a recombinant single-chain variable fragment (scFv) of monoclonal antibody MEM-85 targeted against CD44, the human cell receptor for hyaluronate, which is involved in cancer. Antibody MEM-85 is of therapeutic interest and needed to be characterized in terms of the antigen-binding epitope location and the effects on CD44 structure and function. The scFv fragment is a suitable small-size molecular tool retaining the antigen-binding function and simplifying the whole antibody molecule. The highly homogeneous and stable sample of recombinant scFv

MEM-85 necessary for further experiments was prepared based on a general strategy of optimization of the biophysical properties of scFv fragments, developed also in the framework of this project. NMR-based epitope mapping was employed to unambiguously locate the epitope of MEM-85 in the C-terminal region of the hyaluronate-binding domain (HABD) of CD44. Moreover, the antibody binding induced allosteric conformational changes which lead to an increased disorder in the C-terminal tail of HABD. The character of this conformational rearrangement was similar to that induced by hyaluronate-binding. These important data shed light on the previous observations that MEM-85 cross-blocks hyaluronate binding to CD44 and also induces CD44 shedding. MEM-85 does not do so by a direct physical competition for the hyaluronate-binding site, but rather allosterically, by binding to a distant epitope located close to the membrane-proximal C-terminus of HABD. Small-angle X-ray scattering and mutational experiments combined with surface plasmon resonance allowed us to create a rigid body model for the complex of scFv MEM-85 with CD44 HABD that further corroborates the proposed MEM-85 mode of action.

10 References

1. Stulke, J. & Hillen, W. (2000) Regulation of carbon catabolism in Bacillus species, *Annu. Rev. Microbiol.* **54**, 849-80.
2. Deutscher, J. (2008) The mechanisms of carbon catabolite repression in bacteria, *Curr. Opin. Microbiol.* **11**, 87-93.
3. Steinmetz, M. (1993) Carbohydrate catabolism: pathways, enzymes, genetic regulation, and evolution in *Bacillus subtilis* and other gram-positive bacteria: biochemistry, physiology, and molecular genetics, American Society for Microbiology, Washington, DC, 157-170.
4. Gorke, B. & Stulke, J. (2008) Carbon catabolite repression in bacteria: many ways to make the most out of nutrients, *Nat. Rev. Microbiol.* **6**, 613-24.
5. Stulke, J. & Hillen, W. (1999) Carbon catabolite repression in bacteria, *Curr. Opin. Microbiol.* **2**, 195-201.
6. Bruckner, R. & Titgemeyer, F. (2002) Carbon catabolite repression in bacteria: choice of the carbon source and autoregulatory limitation of sugar utilization, *FEMS Microbiol. Lett.* **209**, 141-8.
7. Hueck, C. J. & Hillen, W. (1995) Catabolite repression in Bacillus subtilis: a global regulatory mechanism for the gram-positive bacteria?, *Mol. Microbiol.* **15**, 395-401.
8. Wehtje, C., Beijer, L., Nilsson, R. P. & Rutberg, B. (1995) Mutations in the glycerol kinase gene restore the ability of a ptsGHI mutant of Bacillus subtilis to grow on glycerol, *Microbiology.* **141 (Pt 5)**, 1193-8.
9. Beijer, L. & Rutberg, L. (1992) Utilisation of glycerol and glycerol 3-phosphate is differently affected by the phosphotransferase system in Bacillus subtilis, *FEMS Microbiol. Lett.* **100**, 217-20.
10. Stulke, J., Arnaud, M., Rapoport, G. & Martin-Verstraete, I. (1998) PRD--a protein domain involved in PTS-dependent induction and carbon catabolite repression of catabolic operons in bacteria, *Mol. Microbiol.* **28**, 865-74.
11. Resch, M., Schiltz, E., Titgemeyer, F. & Muller, Y. A. (2010) Insight into the induction mechanism of the GntR/HutC bacterial transcription regulator YvoA, *Nucleic Acids Res.* **38**, 2485-97.
12. Fillenberg, S. B., Grau, F. C., Seidel, G. & Muller, Y. A. (2015) Structural insight into operator dre-sites recognition and effector binding in the GntR/HutC transcription regulator NagR, *Nucleic Acids Res.* **43**, 1283-96.
13. Jain, D. & Nair, D. T. (2013) Spacing between core recognition motifs determines relative orientation of AraR monomers on bipartite operators, *Nucleic Acids Res.* **41**, 639-47.
14. Prochazkova, K., Cermakova, K., Pachl, P., Sieglova, I., Fabry, M., Otwinowski, Z. & Rezacova, P. (2012) Structure of the effector-binding domain of the arabinose repressor AraR from Bacillus subtilis, *Acta Crystallogr., Sect. D: Biol. Crystallogr.* **68**, 176-85.
15. Rezacova, P., Kozisek, M., Moy, S. F., Sieglova, I., Joachimiak, A., Machius, M. & Otwinowski, Z. (2008) Crystal structures of the effector-binding domain of repressor Central glycolytic gene Regulator from Bacillus subtilis reveal ligand-induced structural changes upon binding of several glycolytic intermediates, *Mol. Microbiol.* **69**, 895-910.
16. Rezacova, P., Krejcirikova, V., Borek, D., Moy, S. F., Joachimiak, A. & Otwinowski, Z. (2007) The crystal structure of the effector-binding domain of the trehalose repressor TreR from Bacillus subtilis 168 reveals a unique quarternary assembly, *Proteins.* **69**, 679-82.

17. Finn, R. D., Bateman, A., Clements, J., Coggill, P., Eberhardt, R. Y., Eddy, S. R., Heger, A., Hetherington, K., Holm, L., Mistry, J., Sonnhammer, E. L., Tate, J. & Punta, M. (2014) Pfam: the protein families database, *Nucleic Acids Res.* **42**, D222-30.
18. Sierro, N., Makita, Y., de Hoon, M. & Nakai, K. (2008) DBTBS: a database of transcriptional regulation in Bacillus subtilis containing upstream intergenic conservation information, *Nucleic Acids Res.* **36**, D93-6.
19. Saxild, H. H., Andersen, L. N. & Hammer, K. (1996) Dra-nupC-pdp operon of Bacillus subtilis: nucleotide sequence, induction by deoxyribonucleosides, and transcriptional regulation by the deoR-encoded DeoR repressor protein, *J. Bacteriol.* **178**, 424-34.
20. Zeng, X. & Saxild, H. H. (1999) Identification and characterization of a DeoR-specific operator sequence essential for induction of dra-nupC-pdp operon expression in Bacillus subtilis, *J. Bacteriol.* **181**, 1719-27.
21. Zeng, X., Galinier, A. & Saxild, H. H. (2000) Catabolite repression of dra-nupC-pdp operon expression in Bacillus subtilis, *Microbiology.* **146 (Pt 11)**, 2901-8.
22. Galinier, A., Deutscher, J. & Martin-Verstraete, I. (1999) Phosphorylation of either crh or HPr mediates binding of CcpA to the bacillus subtilis xyn cre and catabolite repression of the xyn operon, *J. Mol. Biol.* **286**, 307-14.
23. Martin-Verstraete, I., Deutscher, J. & Galinier, A. (1999) Phosphorylation of HPr and Crh by HprK, early steps in the catabolite repression signalling pathway for the Bacillus subtilis levanase operon, *J. Bacteriol.* **181**, 2966-9.
24. Zalieckas, J. M., Wray, L. V., Jr., Ferson, A. E. & Fisher, S. H. (1998) Transcription-repair coupling factor is involved in carbon catabolite repression of the Bacillus subtilis hut and gnt operons, *Mol. Microbiol.* **27**, 1031-8.
25. Zeng, X., Saxild, H. H. & Switzer, R. L. (2000) Purification and characterization of the DeoR repressor of Bacillus subtilis, *J. Bacteriol.* **182**, 1916-22.
26. Schuch, R., Garibian, A., Saxild, H. H., Piggot, P. J. & Nygaard, P. (1999) Nucleosides as a carbon source in Bacillus subtilis: characterization of the drm-pupG operon, *Microbiology.* **145 (Pt 10)**, 2957-66.
27. Amouyal, M., Mortensen, L., Buc, H. & Hammer, K. (1989) Single and double loop formation when deoR repressor binds to its natural operator sites, *Cell.* **58**, 545-51.
28. Harrison, S. C. & Aggarwal, A. K. (1990) DNA recognition by proteins with the helix-turn-helix motif, *Annu. Rev. Biochem.* **59**, 933-69.
29. Pabo, C. O. & Sauer, R. T. (1984) Protein-DNA recognition, *Annu. Rev. Biochem.* **53**, 293-321.
30. Dandanell, G., Valentin-Hansen, P., Larsen, J. E. & Hammer, K. (1987) Long-range cooperativity between gene regulatory sequences in a prokaryote, *Nature.* **325**, 823-6.
31. Gallatin, W. M., Weissman, I. L. & Butcher, E. C. (1983) A cell-surface molecule involved in organ-specific homing of lymphocytes, *Nature.* **304**, 30-4.
32. Stefanova, I., Hilgert, I., Bazil, V., Kristofova, H. & Horejsi, V. (1989) Human leucocyte surface glycoprotein CDw44 and lymphocyte homing receptor are identical molecules, *Immunogenetics.* **29**, 402-4.
33. Bajorath, J., Greenfield, B., Munro, S. B., Day, A. J. & Aruffo, A. (1998) Identification of CD44 residues important for hyaluronan binding and delineation of the binding site, *J. Bio. Chem.* **273**, 338-43.
34. Aruffo, A., Stamenkovic, I., Melnick, M., Underhill, C. B. & Seed, B. (1990) CD44 is the principal cell surface receptor for hyaluronate, *Cell.* **61**, 1303-13.
35. Jalkanen, S. & Jalkanen, M. (1992) Lymphocyte CD44 binds the COOH-terminal heparin-binding domain of fibronectin, *J. Cell Biol.* **116**, 817-25.

36. Ishii, S., Ford, R., Thomas, P., Nachman, A., Steele, G., Jr. & Jessup, J. M. (1993) CD44 participates in the adhesion of human colorectal carcinoma cells to laminin and type IV collagen, *Surg. Oncol.* **2**, 255-64.
37. Konstantopoulos, K. & Thomas, S. N. (2009) Cancer cells in transit: the vascular interactions of tumor cells, *Annu. Rev. Biomed. Eng.* **11**, 177-202.
38. Alves, C. S., Burdick, M. M., Thomas, S. N., Pawar, P. & Konstantopoulos, K. (2008) The dual role of CD44 as a functional P-selectin ligand and fibrin receptor in colon carcinoma cell adhesion, *Am. J. Physiol.* **294**, C907-16.
39. Bendall, L. J., James, A., Zannettino, A., Simmons, P. J., Gottlieb, D. J. & Bradstock, K. F. (2003) A novel CD44 antibody identifies an epitope that is aberrantly expressed on acute lymphoblastic leukaemia cells, *Immunol. Cell Biol.* **81**, 311-9.
40. Daniels, G. (2008) Human blood groups, John Wiley & Sons, Hoboken, NJ.
41. Lokeshwar, V. B., Fregien, N. & Bourguignon, L. Y. (1994) Ankyrin-binding domain of CD44(GP85) is required for the expression of hyaluronic acid-mediated adhesion function, *J. Cell Biol.* **126**, 1099-109.
42. Fehon, R. G., McClatchey, A. I. & Bretscher, A. (2010) Organizing the cell cortex: the role of ERM proteins, *Nat. Rev. Mol. Cell. Biol.* **11**, 276-87.
43. Mori, T., Kitano, K., Terawaki, S., Maesaki, R., Fukami, Y. & Hakoshima, T. (2008) Structural basis for CD44 recognition by ERM proteins, *J. Biol. Chem.* **283**, 29602-12.
44. Anstee, D. J., Gardner, B., Spring, F. A., Holmes, C. H., Simpson, K. L., Parsons, S. F., Mallinson, G., Yousaf, S. M. & Judson, P. A. (1991) New monoclonal antibodies in CD44 and CD58: their use to quantify CD44 and CD58 on normal human erythrocytes and to compare the distribution of CD44 and CD58 in human tissues, *Immunology.* **74**, 197-205.
45. Gee, K., Kryworuchko, M. & Kumar, A. (2004) Recent advances in the regulation of CD44 expression and its role in inflammation and autoimmune diseases, *Arch. Immunol. Ther. Exp.* **52**, 13-26.
46. DeGrendele, H. C., Estess, P. & Siegelman, M. H. (1997) Requirement for CD44 in activated T cell extravasation into an inflammatory site, *Science.* **278**, 672-5.
47. Naor, D., Sionov, R. V. & Ish-Shalom, D. (1997) CD44: structure, function, and association with the malignant process, *Adv. Cancer Res.* **71**, 241-319.
48. DeGrendele, H. C., Estess, P., Picker, L. J. & Siegelman, M. H. (1996) CD44 and its ligand hyaluronate mediate rolling under physiologic flow: a novel lymphocyte-endothelial cell primary adhesion pathway, *J. Exp. Med.* **183**, 1119-30.
49. Goodison, S., Urquidi, V. & Tarin, D. (1999) CD44 cell adhesion molecules, *Mol. Pathol.* **52**, 189-96.
50. Culty, M., Nguyen, H. A. & Underhill, C. B. (1992) The hyaluronan receptor (CD44) participates in the uptake and degradation of hyaluronan, *J. Cell Biol.* **116**, 1055-62.
51. Thankamony, S. P. & Knudson, W. (2006) Acylation of CD44 and its association with lipid rafts are required for receptor and hyaluronan endocytosis, *J. Biol. Chem.* **281**, 34601-9.
52. Stamenkovic, I., Amiot, M., Pesando, J. M. & Seed, B. (1989) A lymphocyte molecule implicated in lymph node homing is a member of the cartilage link protein family, *Cell.* **56**, 1057-62.
53. Goldstein, L. A., Zhou, D. F., Picker, L. J., Minty, C. N., Bargatze, R. F., Ding, J. F. & Butcher, E. C. (1989) A human lymphocyte homing receptor, the hermes antigen, is related to cartilage proteoglycan core and link proteins, *Cell.* **56**, 1063-72.
54. Screaton, G. R., Bell, M. V., Bell, J. I. & Jackson, D. G. (1993) The identification of a new alternative exon with highly restricted tissue expression in transcripts encoding the

mouse Pgp-1 (CD44) homing receptor. Comparison of all 10 variable exons between mouse, human, and rat, *J. Biol. Chem.* **268**, 12235-8.
55. Kalnina, Z., Zayakin, P., Silina, K. & Line, A. (2005) Alterations of pre-mRNA splicing in cancer, *Genes, Chromosomes Cancer.* **42**, 342-57.
56. Lesley, J., Hyman, R. & Kincade, P. W. (1993) CD44 and its interaction with extracellular matrix, *Adv. Immunol.* **54**, 271-335.
57. Zoller, M. (2011) CD44: can a cancer-initiating cell profit from an abundantly expressed molecule?, *Nat. Rev. Cancer.* **11**, 254-67.
58. Screaton, G. R., Bell, M. V., Jackson, D. G., Cornelis, F. B., Gerth, U. & Bell, J. I. (1992) Genomic structure of DNA encoding the lymphocyte homing receptor CD44 reveals at least 12 alternatively spliced exons, *Proc. Natl. Acad. Sci. U. S. A.* **89**, 12160-4.
59. Okamoto, I., Kawano, Y., Tsuiki, H., Sasaki, J., Nakao, M., Matsumoto, M., Suga, M., Ando, M., Nakajima, M. & Saya, H. (1999) CD44 cleavage induced by a membrane-associated metalloprotease plays a critical role in tumor cell migration, *Oncogene.* **18**, 1435-46.
60. Lammich, S., Okochi, M., Takeda, M., Kaether, C., Capell, A., Zimmer, A. K., Edbauer, D., Walter, J., Steiner, H. & Haass, C. (2002) Presenilin-dependent intramembrane proteolysis of CD44 leads to the liberation of its intracellular domain and the secretion of an Abeta-like peptide, *J. Biol. Chem.* **277**, 44754-9.
61. Okamoto, I., Kawano, Y., Murakami, D., Sasayama, T., Araki, N., Miki, T., Wong, A. J. & Saya, H. (2001) Proteolytic release of CD44 intracellular domain and its role in the CD44 signaling pathway, *J. Cell Biol.* **155**, 755-62.
62. Teriete, P., Banerji, S., Noble, M., Blundell, C. D., Wright, A. J., Pickford, A. R., Lowe, E., Mahoney, D. J., Tammi, M. I., Kahmann, J. D., Campbell, I. D., Day, A. J. & Jackson, D. G. (2004) Structure of the regulatory hyaluronan binding domain in the inflammatory leukocyte homing receptor CD44, *Mol. Cell.* **13**, 483-496.
63. Banerji, S., Wright, A. J., Noble, M., Mahoney, D. J., Campbell, I. D., Day, A. J. & Jackson, D. G. (2007) Structures of the Cd44-hyaluronan complex provide insight into a fundamental carbohydrate-protein interaction, *Nat. Struct. Mol. Biol.* **14**, 234-9.
64. Takeda, M., Ogino, S., Umemoto, R., Sakakura, M., Kajiwara, M., Sugahara, K. N., Hayasaka, H., Miyasaka, M., Terasawa, H. & Shimada, I. (2006) Ligand-induced structural changes of the CD44 hyaluronan-binding domain revealed by NMR, *J. Biol. Chem.* **281**, 40089-95.
65. Banerji, S., Day, A. J., Kahmann, J. D. & Jackson, D. G. (1998) Characterization of a functional hyaluronan-binding domain from the human CD44 molecule expressed in Escherichia coli, *Protein Exp. Purif.* **14**, 371-381.
66. Day, A. J. & Prestwich, G. D. (2002) Hyaluronan-binding proteins: tying up the giant, *J. Biol. Chem.* **277**, 4585-8.
67. Pall, T., Gad, A., Kasak, L., Drews, M., Stromblad, S. & Kogerman, P. (2004) Recombinant CD44-HABD is a novel and potent direct angiogenesis inhibitor enforcing endothelial cell-specific growth inhibition independently of hyaluronic acid binding, *Oncogene.* **23**, 7874-81.
68. Greenfield, B., Wang, W. C., Marquardt, H., Piepkorn, M., Wolff, E. A., Aruffo, A. & Bennett, K. L. (1999) Characterization of the heparan sulfate and chondroitin sulfate assembly sites in CD44, *J. Biol. Chem.* **274**, 2511-7.
69. Peach, R. J., Hollenbaugh, D., Stamenkovic, I. & Aruffo, A. (1993) Identification of hyaluronic acid binding sites in the extracellular domain of CD44, *J. Cell Biol.* **122**, 257-64.
70. Ogino, S., Nishida, N., Umemoto, R., Suzuki, M., Takeda, M., Terasawa, H., Kitayama, J., Matsumoto, M., Hayasaka, H., Miyasaka, M. & Shimada, I. (2010) Two-

state conformations in the hyaluronan-binding domain regulate CD44 adhesiveness under flow condition, *Structure.* **18**, 649-56.
71. Cichy, J. & Pure, E. (2003) The liberation of CD44, *J. Cell Biol.* **161**, 839-43.
72. Nagano, O. & Saya, H. (2004) Mechanism and biological significance of CD44 cleavage, *Cancer Sci.* **95**, 930-5.
73. Sleeman, J., Rudy, W., Hofmann, M., Moll, J., Herrlich, P. & Ponta, H. (1996) Regulated clustering of variant CD44 proteins increases their hyaluronate binding capacity, *J. Cell Biol.* **135**, 1139-50.
74. Lesley, J. & Hyman, R. (1998) CD44 structure and function, *Front. Biosci.* **3**, d616-30.
75. English, N. M., Lesley, J. F. & Hyman, R. (1998) Site-specific de-N-glycosylation of CD44 can activate hyaluronan binding, and CD44 activation states show distinct threshold densities for hyaluronan binding, *Cancer Res.* **58**, 3736-42.
76. Legg, J. W., Lewis, C. A., Parsons, M., Ng, T. & Isacke, C. M. (2002) A novel PKC-regulated mechanism controls CD44 ezrin association and directional cell motility, *Nat. Cell Biol.* **4**, 399-407.
77. Neame, S. J. & Isacke, C. M. (1993) The cytoplasmic tail of CD44 is required for basolateral localization in epithelial MDCK cells but does not mediate association with the detergent-insoluble cytoskeleton of fibroblasts, *J. Cell Biol.* **121**, 1299-310.
78. Alves, C. S., Yakovlev, S., Medved, L. & Konstantopoulos, K. (2009) Biomolecular characterization of CD44-fibrin(ogen) binding: distinct molecular requirements mediate binding of standard and variant isoforms of CD44 to immobilized fibrin(ogen), *J. Biol. Chem.* **284**, 1177-89.
79. Faller, C. E. & Guvench, O. (2014) Terminal sialic acids on CD44 N-glycans can block hyaluronan binding by forming competing intramolecular contacts with arginine sidechains, *Proteins.* **82**, 3079-89.
80. Ponta, H., Sherman, L. & Herrlich, P. A. (2003) CD44: from adhesion molecules to signalling regulators, *Nat. Rev. Mol. Cell. Biol.* **4**, 33-45.
81. Naor, D., Wallach-Dayan, S. B., Zahalka, M. A. & Sionov, R. V. (2008) Involvement of CD44, a molecule with a thousand faces, in cancer dissemination, *Semin. Cancer Biol.* **18**, 260-7.
82. Lynch, K. W. (2004) Consequences of regulated pre-mRNA splicing in the immune system, *Nat. Rev. Immunol.* **4**, 931-40.
83. He, Q., Lesley, J., Hyman, R., Ishihara, K. & Kincade, P. W. (1992) Molecular isoforms of murine CD44 and evidence that the membrane proximal domain is not critical for hyaluronate recognition, *J. Cell Biol.* **119**, 1711-9.
84. Bennett, K. L., Jackson, D. G., Simon, J. C., Tanczos, E., Peach, R., Modrell, B., Stamenkovic, I., Plowman, G. & Aruffo, A. (1995) CD44 isoforms containing exon V3 are responsible for the presentation of heparin-binding growth factor, *J. Cell Biol.* **128**, 687-98.
85. Orian-Rousseau, V. & Ponta, H. (2008) Adhesion proteins meet receptors: a common theme?, *Adv. Cancer Res.*. **101**, 63-92.
86. Tremmel, M., Matzke, A., Albrecht, I., Laib, A. M., Olaku, V., Ballmer-Hofer, K., Christofori, G., Heroult, M., Augustin, H. G., Ponta, H. & Orian-Rousseau, V. (2009) A CD44v6 peptide reveals a role of CD44 in VEGFR-2 signaling and angiogenesis, *Blood.* **114**, 5236-44.
87. Johnson, P. & Ruffell, B. (2009) CD44 and its role in inflammation and inflammatory diseases, *Inflammation Allergy: Drug Targets.* **8**, 208-20.
88. Naor, D., Nedvetzki, S., Golan, I., Melnik, L. & Faitelson, Y. (2002) CD44 in cancer, *Crit. Rev. Clin. Lab. Sci.* **39**, 527-79.

89. Lesley, J., Hyman, R., English, N., Catterall, J. B. & Turner, G. A. (1997) CD44 in inflammation and metastasis, *Glycoconjugate J.* **14**, 611-22.
90. Estess, P., DeGrendele, H. C., Pascual, V. & Siegelman, M. H. (1998) Functional activation of lymphocyte CD44 in peripheral blood is a marker of autoimmune disease activity, *J. Clin. Invest.* **102**, 1173-82.
91. Haynes, B. F., Hale, L. P., Patton, K. L., Martin, M. E. & McCallum, R. M. (1991) Measurement of an adhesion molecule as an indicator of inflammatory disease activity. Up-regulation of the receptor for hyaluronate (CD44) in rheumatoid arthritis, *Arthritis Rheum.* **34**, 1434-43.
92. Gunthert, U., Hofmann, M., Rudy, W., Reber, S., Zoller, M., Haussmann, I., Matzku, S., Wenzel, A., Ponta, H. & Herrlich, P. (1991) A new variant of glycoprotein CD44 confers metastatic potential to rat carcinoma cells, *Cell.* **65**, 13-24.
93. Itoh, Y. & Seiki, M. (2006) MT1-MMP: a potent modifier of pericellular microenvironment, *J. Cell. Physiol.* **206**, 1-8.
94. Kuncová, J., Mandys, V., Heráček, J., Lukeš, M., Zachoval, R. & Urban, M. (2003) Význam alterací adhezivních molekul CD44 v maligním chování nádorů, *Klin. Onkol.* **16**, 171-7.
95. Dworzak, M. N., Fritsch, G., Fleischer, C., Printz, D., Froschl, G., Buchinger, P., Mann, G. & Gadner, H. (1998) Comparative phenotype mapping of normal vs. malignant pediatric B-lymphopoiesis unveils leukemia-associated aberrations, *Exp. Hematol.* **26**, 305-13.
96. Dworzak, M. N., Stolz, F., Froschl, G., Printz, D., Henn, T., Fischer, S., Fleischer, C., Haas, O. A., Fritsch, G., Gadner, H. & Panzer-Grumayer, E. R. (1999) Detection of residual disease in pediatric B-cell precursor acute lymphoblastic leukemia by comparative phenotype mapping: a study of five cases controlled by genetic methods, *Exp. Hematol.* **27**, 673-81.
97. Shtivelman, E. & Bishop, J. M. (1991) Expression of CD44 is repressed in neuroblastoma cells, *Mol. Cell. Biol.* **11**, 5446-53.
98. Gao, A. C., Lou, W., Dong, J. T. & Isaacs, J. T. (1997) CD44 is a metastasis suppressor gene for prostatic cancer located on human chromosome 11p13, *Cancer Res.* **57**, 846-9.
99. De Marzo, A. M., Bradshaw, C., Sauvageot, J., Epstein, J. I. & Miller, G. J. (1998) CD44 and CD44v6 downregulation in clinical prostatic carcinoma: relation to Gleason grade and cytoarchitecture, *Prostate.* **34**, 162-8.
100. Ratajczak, M. Z. (2005) Cancer stem cells-normal stem cells "Jedi" that went over to the "dark side", *Folia Histochem. Cytobiol.* **43**, 175-81.
101. Wielenga, V. J., van der Neut, R., Offerhaus, G. J. & Pals, S. T. (2000) CD44 glycoproteins in colorectal cancer: expression, function, and prognostic value, *Adv. Cancer Res.* **77**, 169-87.
102. Prives, C. & Hall, P. A. (1999) The p53 pathway, *J. Pathol.* **187**, 112-26.
103. Godar, S., Ince, T. A., Bell, G. W., Feldser, D., Donaher, J. L., Bergh, J., Liu, A., Miu, K., Watnick, R. S., Reinhardt, F., McAllister, S. S., Jacks, T. & Weinberg, R. A. (2008) Growth-inhibitory and tumor- suppressive functions of p53 depend on its repression of CD44 expression, *Cell.* **134**, 62-73.
104. Bourguignon, L. Y., Zhu, H., Chu, A., Iida, N., Zhang, L. & Hung, M. C. (1997) Interaction between the adhesion receptor, CD44, and the oncogene product, p185HER2, promotes human ovarian tumor cell activation, *J. Biol. Chem.* **272**, 27913-8.
105. Yu, Q. & Stamenkovic, I. (1999) Localization of matrix metalloproteinase 9 to the cell surface provides a mechanism for CD44-mediated tumor invasion, *Genes Dev.* **13**, 35-48.

106. Yu, Y., Ramena, G. & Elble, R. C. (2012) The role of cancer stem cells in relapse of solid tumors, *Front. Biosci.* **4**, 1528-41.
107. Misra, S., Heldin, P., Hascall, V. C., Karamanos, N. K., Skandalis, S. S., Markwald, R. R. & Ghatak, S. (2011) Hyaluronan-CD44 interactions as potential targets for cancer therapy, *FEBS J.* **278**, 1429-43.
108. Ghatak, S., Misra, S. & Toole, B. P. (2005) Hyaluronan constitutively regulates ErbB2 phosphorylation and signaling complex formation in carcinoma cells, *J. Biol. Chem.* **280**, 8875-83.
109. Ghatak, S., Misra, S. & Toole, B. P. (2002) Hyaluronan oligosaccharides inhibit anchorage-independent growth of tumor cells by suppressing the phosphoinositide 3-kinase/Akt cell survival pathway, *J. Biol. Chem.* **277**, 38013-20.
110. Misra, S., Ghatak, S. & Toole, B. P. (2005) Regulation of MDR1 expression and drug resistance by a positive feedback loop involving hyaluronan, phosphoinositide 3-kinase, and ErbB2, *J. Biol. Chem.* **280**, 20310-5.
111. Zhu, H., Mitsuhashi, N., Klein, A., Barsky, L. W., Weinberg, K., Barr, M. L., Demetriou, A. & Wu, G. D. (2006) The role of the hyaluronan receptor CD44 in mesenchymal stem cell migration in the extracellular matrix, *Stem Cells.* **24**, 928-35.
112. Zoltan-Jones, A., Huang, L., Ghatak, S. & Toole, B. P. (2003) Elevated hyaluronan production induces mesenchymal and transformed properties in epithelial cells, *J. Biol. Chem.* **278**, 45801-10.
113. Liu, L. K. & Finzel, B. C. (2014) Fragment-based identification of an inducible binding site on cell surface receptor CD44 for the design of protein-carbohydrate interaction inhibitors, *J. Med. Chem.* **57**, 2714-25.
114. Luo, Y., Kirker, K. R. & Prestwich, G. D. (2000) Cross-linked hyaluronic acid hydrogel films: new biomaterials for drug delivery, *J. Controlled Release.* **69**, 169-84.
115. Luo, Y. & Prestwich, G. D. (1999) Synthesis and selective cytotoxicity of a hyaluronic acid-antitumor bioconjugate, *Bioconjugate Chem.* **10**, 755-63.
116. Luo, Y., Ziebell, M. R. & Prestwich, G. D. (2000) A hyaluronic acid-taxol antitumor bioconjugate targeted to cancer cells, *Biomacromolecules.* **1**, 208-18.
117. Zheng, Z., Katoh, S., He, Q., Oritani, K., Miyake, K., Lesley, J., Hyman, R., Hamik, A., Parkhouse, R. M., Farr, A. G. & Kincade, P. W. (1995) Monoclonal antibodies to CD44 and their influence on hyaluronan recognition, *J. Cell Biol.* **130**, 485-95.
118. Perez, A., Neskey, D. M., Wen, J., Pereira, L., Reategui, E. P., Goodwin, W. J., Carraway, K. L. & Franzmann, E. J. (2013) CD44 interacts with EGFR and promotes head and neck squamous cell carcinoma initiation and progression, *Oral Oncol.* **49**, 306-13.
119. Seiter, S., Arch, R., Reber, S., Komitowski, D., Hofmann, M., Ponta, H., Herrlich, P., Matzku, S. & Zoller, M. (1993) Prevention of tumor metastasis formation by anti-variant CD44, *J. Exp. Med.* **177**, 443-55.
120. Song, G., Liao, X., Zhou, L., Wu, L., Feng, Y. & Han, Z. C. (2004) HI44a, an anti-CD44 monoclonal antibody, induces differentiation and apoptosis of human acute myeloid leukemia cells, *Leuk. Res.* **28**, 1089-96.
121. Jin, L., Hope, K. J., Zhai, Q., Smadja-Joffe, F. & Dick, J. E. (2006) Targeting of CD44 eradicates human acute myeloid leukemic stem cells, *Nat. Med.*. **12**, 1167-74.
122. Charrad, R. S., Gadhoum, Z., Qi, J., Glachant, A., Allouche, M., Jasmin, C., Chomienne, C. & Smadja-Joffe, F. (2002) Effects of anti-CD44 monoclonal antibodies on differentiation and apoptosis of human myeloid leukemia cell lines, *Blood.* **99**, 290-9.
123. Borjesson, P. K., Postema, E. J., Roos, J. C., Colnot, D. R., Marres, H. A., van Schie, M. H., Stehle, G., de Bree, R., Snow, G. B., Oyen, W. J. & van Dongen, G. A. (2003) Phase I therapy study with (186)Re-labeled humanized monoclonal antibody BIWA 4

(bivatuzumab) in patients with head and neck squamous cell carcinoma, *Clin. Cancer Res.* **9**, 3961S-72S.
124. Tijink, B. M., Buter, J., de Bree, R., Giaccone, G., Lang, M. S., Staab, A., Leemans, C. R. & van Dongen, G. A. (2006) A phase I dose escalation study with anti-CD44v6 bivatuzumab mertansine in patients with incurable squamous cell carcinoma of the head and neck or esophagus, *Clin. Cancer Res.* **12**, 6064-72.
125. Lee, E., Hong, Y., Choi, J., Haam, S., Suh, J. S., Huh, Y. M. & Yang, J. (2012) Highly selective CD44-specific gold nanorods for photothermal ablation of tumorigenic subpopulations generated in MCF7 mammospheres, *Nanotechnology.* **23**, 465101.
126. Naujokat, C. (2012) Targeting human cancer stem cells with monoclonal antibodies, *J. Clin. Cell. Immunol*. **S5**, 007.
127. Naujokat, C. (2014) Monoclonal antibodies against human cancer stem cells, *Immunotherapy.* **6**, 290-308.
128. Charrad, R. S., Li, Y., Delpech, B., Balitrand, N., Clay, D., Jasmin, C., Chomienne, C. & Smadja-Joffe, F. (1999) Ligation of the CD44 adhesion molecule reverses blockage of differentiation in human acute myeloid leukemia, *Nat. Med.* **5**, 669-76.
129. Gadhoum, Z., Delaunay, J., Maquarre, E., Durand, L., Lancereaux, V., Qi, J., Robert-Lezenes, J., Chomienne, C. & Smadja-Joffe, F. (2004) The effect of anti-CD44 monoclonal antibodies on differentiation and proliferation of human acute myeloid leukemia cells, *Leuk. Lymphoma.* **45**, 1501-10.
130. Marangoni, E., Lecomte, N., Durand, L., de Pinieux, G., Decaudin, D., Chomienne, C., Smadja-Joffe, F. & Poupon, M. F. (2009) CD44 targeting reduces tumour growth and prevents post-chemotherapy relapse of human breast cancers xenografts, *Br. J. Cancer.* **100**, 918-22.
131. Masuko, K., Okazaki, S., Satoh, M., Tanaka, G., Ikeda, T., Torii, R., Ueda, E., Nakano, T., Danbayashi, M., Tsuruoka, T., Ohno, Y., Yagi, H., Yabe, N., Yoshida, H., Tahara, T., Kataoka, S., Oshino, T., Shindo, T., Niwa, S., Ishimoto, T., Baba, H., Hashimoto, Y., Saya, H. & Masuko, T. (2012) Anti-tumor effect against human cancer xenografts by a fully human monoclonal antibody to a variant 8-epitope of CD44R1 expressed on cancer stem cells, *PloS One.* **7**, e29728.
132. Weigand, S., Herting, F., Maisel, D., Nopora, A., Voss, E., Schaab, C., Klammer, M. & Tebbe, A. (2012) Global quantitative phosphoproteome analysis of human tumor xenografts treated with a CD44 antagonist, *Cancer Res.*. **72**, 4329-39.
133. Zhang, S., Wu, C. C., Fecteau, J. F., Cui, B., Chen, L., Zhang, L., Wu, R., Rassenti, L., Lao, F., Weigand, S. & Kipps, T. J. (2013) Targeting chronic lymphocytic leukemia cells with a humanized monoclonal antibody specific for CD44, *Proc. Natl. Acad. Sci. U. S. A.* **110**, 6127-32.
134. Orian-Rousseau, V. (2010) CD44, a therapeutic target for metastasising tumours, *Eur. J. Cancer.* **46**, 1271-7.
135. Heider, K. H., Kuthan, H., Stehle, G. & Munzert, G. (2004) CD44v6: a target for antibody-based cancer therapy, *Cancer Immunol. Immunother.* **53**, 567-79.
136. de Bree, R., Roos, J. C., Quak, J. J., den Hollander, W., Snow, G. B. & van Dongen, G. A. (1995) Radioimmunoscintigraphy and biodistribution of technetium-99m-labeled monoclonal antibody U36 in patients with head and neck cancer, *Clin. Cancer Res.* **1**, 591-8.
137. de Bree, R., Roos, J. C., Plaizier, M. A., Quak, J. J., van Kamp, G. J., den Hollander, W., Snow, G. B. & van Dongen, G. A. (1997) Selection of monoclonal antibody E48 IgG or U36 IgG for adjuvant radioimmunotherapy in head and neck cancer patients, *Br. J. Cancer.* **75**, 1049-60.

138. Brakenhoff, R. H., van Gog, F. B., Looney, J. E., van Walsum, M., Snow, G. B. & van Dongen, G. A. (1995) Construction and characterization of the chimeric monoclonal antibody E48 for therapy of head and neck cancer, *Cancer Immunol. Immunother.* **40**, 191-200.
139. Colnot, D. R., Quak, J. J., Roos, J. C., de Bree, R., Wilhelm, A. J., Snow, G. B. & van Dongen, G. A. (2001) Radioimmunotherapy in patients with head and neck squamous cell carcinoma: initial experience, *Head & Neck.* **23**, 559-65.
140. Colnot, D. R., Quak, J. J., Roos, J. C., van Lingen, A., Wilhelm, A. J., van Kamp, G. J., Huijgens, P. C., Snow, G. B. & van Dongen, G. A. (2000) Phase I therapy study of 186Re-labeled chimeric monoclonal antibody U36 in patients with squamous cell carcinoma of the head and neck, *J. Nucl. Med.* **41**, 1999-2010.
141. Colnot, D. R., Wilhelm, A. J., Cloos, J., Roos, J. C., de Bree, R., Quak, J. J., Snow, G. B. & van Dongen, G. A. (2001) Evaluation of limited blood sampling in a preceding 99mTc-labeled diagnostic study to predict the pharmacokinetics and myelotoxicity of 186Re-cMAb U36 radioimmunotherapy, *J. Nucl. Med.* **42**, 1364-7.
142. Koppe, M., Schaijk, F., Roos, J., Leeuwen, P., Heider, K. H., Kuthan, H. & Bleichrodt, R. (2004) Safety, pharmacokinetics, immunogenicity, and biodistribution of (186)Re-labeled humanized monoclonal antibody BIWA 4 (Bivatuzumab) in patients with early-stage breast cancer, *Cancer Biother. Radiopharm.* **19**, 720-9.
143. Stroomer, J. W., Roos, J. C., Sproll, M., Quak, J. J., Heider, K. H., Wilhelm, B. J., Castelijns, J. A., Meyer, R., Kwakkelstein, M. O., Snow, G. B., Adolf, G. R. & van Dongen, G. A. (2000) Safety and biodistribution of 99mTechnetium-labeled anti-CD44v6 monoclonal antibody BIWA 1 in head and neck cancer patients, *Clin. Cancer Res.* **6**, 3046-55.
144. Postema, E. J., Borjesson, P. K., Buijs, W. C., Roos, J. C., Marres, H. A., Boerman, O. C., de Bree, R., Lang, M., Munzert, G., van Dongen, G. A. & Oyen, W. J. (2003) Dosimetric analysis of radioimmunotherapy with 186Re-labeled bivatuzumab in patients with head and neck cancer, *J. Nucl. Med.* **44**, 1690-9.
145. Sauter, A., Kloft, C., Gronau, S., Bogeschdorfer, F., Erhardt, T., Golze, W., Schroen, C., Staab, A., Riechelmann, H. & Hoermann, K. (2007) Pharmacokinetics, immunogenicity and safety of bivatuzumab mertansine, a novel CD44v6-targeting immunoconjugate, in patients with squamous cell carcinoma of the head and neck, *Int. J. Oncol.* **30**, 927-35.
146. Liu, C. & Chari, R. V. (1997) The development of antibody delivery systems to target cancer with highly potent maytansinoids, *Expert Opin. Invest. Drugs.* **6**, 169-72.
147. Widdison, W. C., Wilhelm, S. D., Cavanagh, E. E., Whiteman, K. R., Leece, B. A., Kovtun, Y., Goldmacher, V. S., Xie, H., Steeves, R. M., Lutz, R. J., Zhao, R., Wang, L., Blattler, W. A. & Chari, R. V. (2006) Semisynthetic maytansine analogues for the targeted treatment of cancer, *J. Med. Chem.* **49**, 4392-408.
148. Riechelmann, H., Sauter, A., Golze, W., Hanft, G., Schroen, C., Hoermann, K., Erhardt, T. & Gronau, S. (2008) Phase I trial with the CD44v6-targeting immunoconjugate bivatuzumab mertansine in head and neck squamous cell carcinoma, *Oral Oncol.* **44**, 823-9.
149. Bazil, V., Stefanova, I., Hilgert, I., Kristofova, H., Vanek, S., Bukovsky, A. & Horejsi, V. (1989) Monoclonal antibodies against human leucocyte antigens. III. Antibodies against CD45R, CD6, CD44 and two newly described broadly expressed glycoproteins MEM-53 and MEM-102, *Folia Biol.* **35**, 289-97.
150. Sandmaier, B. M., Storb, R., Bennett, K. L., Appelbaum, F. R. & Santos, E. B. (1998) Epitope specificity of CD44 for monoclonal antibody-dependent facilitation of marrow engraftment in a canine model, *Blood.* **91**, 3494-502.

151. Bazil, V. & Horejsi, V. (1992) Shedding of the CD44 adhesion molecule from leukocytes induced by anti-CD44 monoclonal antibody simulating the effect of a natural receptor ligand, *J. Immunol.* **149**, 747-53.
152. de Sanctis, D., McVey, C. E., Enguita, F. J. & Carrondo, M. A. (2009) Crystal structure of the full-length sorbitol operon regulator SorC from Klebsiella pneumoniae: structural evidence for a novel transcriptional regulation mechanism, *J. Mol. Biol.* **387**, 759-70.
153. Dym, O. & Eisenberg, D. (2001) Sequence-structure analysis of FAD-containing proteins, *Protein Sci.* **10**, 1712-28.
154. Bellamacina, C. R. (1996) The nicotinamide dinucleotide binding motif: a comparison of nucleotide binding proteins, *FASEB J.* **10**, 1257-69.
155. Wierenga, R. K., Demaeyer, M. C. H. & Hol, W. G. J. (1985) Interaction of Pyrophosphate Moieties with Alpha-Helixes in Dinucleotide Binding-Proteins, *Biochemistry.* **24**, 1346-1357.
156. Holm, L. & Rosenstrom, P. (2010) Dali server: conservation mapping in 3D, *Nucleic Acids Res.* **38**, W545-9.
157. Baugh, L., Gallagher, L. A., Patrapuvich, R., Clifton, M. C., Gardberg, A. S., Edwards, T. E., Armour, B., Begley, D. W., Dieterich, S. H., Dranow, D. M., Abendroth, J., Fairman, J. W., Fox, D., 3rd, Staker, B. L., Phan, I., Gillespie, A., Choi, R., Nakazawa-Hewitt, S., Nguyen, M. T., Napuli, A., Barrett, L., Buchko, G. W., Stacy, R., Myler, P. J., Stewart, L. J., Manoil, C. & Van Voorhis, W. C. (2013) Combining functional and structural genomics to sample the essential Burkholderia structome, *PloS One.* **8**, e53851.
158. Heine, A., DeSantis, G., Luz, J. G., Mitchell, M., Wong, C. H. & Wilson, I. A. (2001) Observation of covalent intermediates in an enzyme mechanism at atomic resolution, *Science.* **294**, 369-74.
159. Bennett, B. D., Kimball, E. H., Gao, M., Osterhout, R., Van Dien, S. J. & Rabinowitz, J. D. (2009) Absolute metabolite concentrations and implied enzyme active site occupancy in Escherichia coli, *Nat. Chem. Biol.* **5**, 593-9.
160. Pantoliano, M. W., Petrella, E. C., Kwasnoski, J. D., Lobanov, V. S., Myslik, J., Graf, E., Carver, T., Asel, E., Springer, B. A., Lane, P. & Salemme, F. R. (2001) High-density miniaturized thermal shift assays as a general strategy for drug discovery, *J. Biomol. Screening.* **6**, 429-40.
161. Lo, M. C., Aulabaugh, A., Jin, G., Cowling, R., Bard, J., Malamas, M. & Ellestad, G. (2004) Evaluation of fluorescence-based thermal shift assays for hit identification in drug discovery, *Anal. Biochem.* **332**, 153-9.
162. Ericsson, U. B., Hallberg, B. M., Detitta, G. T., Dekker, N. & Nordlund, P. (2006) Thermofluor-based high-throughput stability optimization of proteins for structural studies, *Anal. Biochem.* **357**, 289-98.
163. Huston, J. S., Levinson, D., Mudgett-Hunter, M., Tai, M. S., Novotny, J., Margolies, M. N., Ridge, R. J., Bruccoleri, R. E., Haber, E., Crea, R. & et al. (1988) Protein engineering of antibody binding sites: recovery of specific activity in an anti-digoxin single-chain Fv analogue produced in Escherichia coli, *Proc. Natl. Acad. Sci. U. S. A.* **85**, 5879-83.
164. Power, B. E., Doughty, L., Shapira, D. R., Burns, J. E., Bayly, A. M., Caine, J. M., Liu, Z., Scott, A. M., Hudson, P. J. & Kortt, A. A. (2003) Noncovalent scFv multimers of tumor-targeting anti-Lewis(y) hu3S193 humanized antibody, *Protein Sci.* **12**, 734-47.
165. Kortt, A. A., Lah, M., Oddie, G. W., Gruen, C. L., Burns, J. E., Pearce, L. A., Atwell, J. L., McCoy, A. J., Howlett, G. J., Metzger, D. W., Webster, R. G. & Hudson, P. J. (1997) Single-chain Fv fragments of anti-neuraminidase antibody NC10 containing five- and ten-residue linkers form dimers and with zero-residue linker a trimer, *Protein Eng.* **10**, 423-33.

166. Holliger, P., Prospero, T. & Winter, G. (1993) "Diabodies": small bivalent and bispecific antibody fragments, *Proc. Natl. Acad. Sci. U. S. A.* **90**, 6444-8.
167. Atwell, J. L., Breheney, K. A., Lawrence, L. J., McCoy, A. J., Kortt, A. A. & Hudson, P. J. (1999) scFv multimers of the anti-neuraminidase antibody NC10: length of the linker between VH and VL domains dictates precisely the transition between diabodies and triabodies, *Protein Eng.* **12**, 597-604.
168. Carmichael, J. A., Power, B. E., Garrett, T. P., Yazaki, P. J., Shively, J. E., Raubischek, A. A., Wu, A. M. & Hudson, P. J. (2003) The crystal structure of an anti-CEA scFv diabody assembled from T84.66 scFvs in V(L)-to-V(H) orientation: implications for diabody flexibility, *J. Mol. Biol.* **326**, 341-51.
169. Arndt, K. M., Muller, K. M. & Pluckthun, A. (1998) Factors influencing the dimer to monomer transition of an antibody single-chain Fv fragment, *Biochemistry.* **37**, 12918-26.
170. Reinhard, L., Mayerhofer, H., Geerlof, A., Mueller-Dieckmann, J. & Weiss, M. S. (2013) Optimization of protein buffer cocktails using Thermofluor, *Acta Crystallogr., Sect. F: Struct. Biol. Cryst. Commun.* **69**, 209-14.
171. Adams, G. P. & Schier, R. (1999) Generating improved single-chain Fv molecules for tumor targeting, *J. Immunol. Methods.* **231**, 249-260.
172. Addis, P. W., Hall, C. J., Bruton, S., Veverka, V., Wilkinson, I. C., Muskett, F. W., Renshaw, P. S., Prosser, C. E., Carrington, B., Lawson, A. D., Griffin, R., Taylor, R. J., Waters, L. C., Henry, A. J. & Carr, M. D. (2014) Conformational Heterogeneity in Antibody-Protein Antigen Recognition: Implications for High Affinity Protein Complex Formation, *J. Biol. Chem.* **289**, 7200-10.
173. Wilkinson, I. C., Hall, C. J., Veverka, V., Shi, J. Y., Muskett, F. W., Stephens, P. E., Taylor, R. J., Henry, A. J. & Carr, M. D. (2009) High Resolution NMR-based Model for the Structure of a scFv-IL-1 beta Complex Potential for NMR as a Key Tool in Therapeutic Antibody Design and Development, *J. Biol. Chem.* **284**, 31928-31935.